9-2022

Enabling Rapid Chemical Analysis of Plutonium Alloys via Machine Learning-enhanced Atomic Spectroscopy Techniques

Ashwin P. Rao

Recommended Citation

Rao, Ashwin P., "Enabling Rapid Chemical Analysis of Plutonium Alloys via Machine Learning-enhanced Atomic Spectroscopy Techniques" (2022). *Theses and Dissertations*. 5496.
https://scholar.afit.edu/etd/5496

ENABLING RAPID CHEMICAL ANALYSIS OF PLUTONIUM ALLOYS *VIA* MACHINE LEARNING-ENHANCED ATOMIC SPECTROSCOPY TECHNIQUES

DISSERTATION

Ashwin P. Rao, First Lieutenant, USAF

AFIT-ENP-DS-22-S-048

DEPARTMENT OF THE AIR FORCE
AIR UNIVERSITY

AIR FORCE INSTITUTE OF TECHNOLOGY

Wright-Patterson Air Force Base, Ohio

DISTRIBUTION STATEMENT A
APPROVED FOR PUBLIC RELEASE; LA-UR-22-22098

AFIT-ENP-DS-22-S-048

ENABLING RAPID CHEMICAL ANALYSIS OF PLUTONIUM ALLOYS *VIA* MACHINE LEARNING-ENHANCED ATOMIC SPECTROSCOPY TECHNIQUES

DISSERTATION

Presented to the Faculty
Graduate School of Engineering and Management
Air Force Institute of Technology
Air University
Air Education and Training Command
in Partial Fulfillment of the Requirements for the
Degree of Doctor of Philosophy in Nuclear Engineering

Ashwin P. Rao, B.S.E, M.S.
First Lieutenant, USAF

SU22

DISTRIBUTION STATEMENT A
APPROVED FOR PUBLIC RELEASE; LA-UR-22-22098

AFIT-ENP-DS-22-S-048

Abstract

Analytical atomic spectroscopy methods have the potential to provide solutions for rapid, high fidelity chemical analysis of plutonium alloys. Implementing these methods with advanced analytical techniques can help reduce the chemical analysis time needed for plutonium pit production, directly enabling the 80 pit-per-year by 2030 manufacturing goal outlined in the 2018 Nuclear Posture Review. Two commercial, handheld elemental analyzers were validated for potential in situ analysis of Pu. A handheld XRF device was able to detect gallium in a Pu surrogate matrix with a detection limit of 0.002 wt% and a mean error of 8%. A handheld LIBS device was able to yield univariate detection limits as low as 0.1 wt% Ga with mean error of 3%. Implementing machine learning methods for spectral analysis with the handheld LIBS device reduced error to 0.27%, but the limited device resolution impedes improvements in sensitivity. A compact Echelle spectrometer was implemented with a laboratory LIBS setup to reach a detection limit of 0.006 wt% Ga when coupled with an optimized extra trees regression. A Gaussian kernel regression trained on this high resolution data set yielded the most accurate predictive model with 0.33% error. Lastly, the phenomenon of self-absorption was quantified and corrected for in Ce-Ga LIBS spectra. By implementing a Stark broadening based correction, the univariate detection limit for Ga from LIBS spectra was reduced to 0.008%. Overall, this research indicates that implementing a compact, high resolving power spectrograph for recording Pu alloy spectra and developing optimized machine learning models for spectral analysis can yield high fidelity solutions for Pu alloy chemical analysis and quality control.

AFIT-ENP-DS-22-S-048

To all my friends, near and far, who made these last two years pleasantly bearable.
"I don't know half of you half as well as I should like; and I like less than half of you half as well as you deserve." - Bilbo Baggins

Acknowledgements

This dissertation was the culmination of four years worth of experimental work I conducted with various people across the DOD and DOE. Firstly, I am grateful to my research committee for their support in helping me publish my work, as the amount of research we generated together for the spectroscopic community was far from trivial. I would also like to thank Dung Vu at Los Alamos for helping me collect Pu spectra and enabling that part of this research. I feel I have truly been able to excel above and beyond what I ever imagined I'd accomplish as a graduate student because of these people and their support.

This research was funded by the Defense Threat Reduction Agency Nuclear Science and Engineering Research Center, the Air Force Office of Scientific Research, and by internal funding at Los Alamos National Laboratory through Material Recycle and Recovery and Plutonium Sustainment.

Ashwin P. Rao

Table of Contents

List of Figures

Figure Page

List of Tables

Table Page

ENABLING RAPID CHEMICAL ANALYSIS OF PLUTONIUM ALLOYS *VIA* MACHINE LEARNING-ENHANCED ATOMIC SPECTROSCOPY TECHNIQUES

I. Introduction

The 2018 Nuclear Posture Review (NPR) outlined several initiatives to be pursued by the United States to ensure the necessary capability, capacity, and responsiveness of nuclear weapons infrastructure and the needed skills of the workforce. One of these initiatives is outlined as follows:

> "Provide the enduring capability and capacity to produce plutonium pits at a rate of no fewer than 80 pits per year by 2030. A delay in this would result in the need for a higher rate of pit production at higher cost."

The production of these pits, which are the masses of fissile fuel in a nuclear weapon primary, is a complex process involving several metallurgical and radiochemical processing steps to turn raw plutonium into a finished nuclear component. Increasing the production rate would greatly bolster US deterrence posture and allow us to keep pace with global adversaries in their nuclear endeavors. One avenue to shorten the Pu component production timeline would be to reduce the time required for analysis of plutonium alloys at various stages of the production cycle.

The complex series of metallurgical and chemical steps that plutonium metal is subjected to during processing introduces several avenues for minor metal impurities to be introduced into the final alloy. Pits must meet a certain chemical specification which limits the concentration of minor elements which can appear in the bulk Pu metal. Traditionally, the levels of impurities present are evaluated using mass spectrometry methods, such as inductively coupled plasma - optical emission spectroscopy (ICP-OES) or mass spectrometry (ICP-MS). These established methods consistently and accurately yield trace elemental information of impurities in Pu metal down to the parts-per-billion (ppb) level. Although they provide accurate chemical content information, they introduce a significant amount of analysis time into the overall production process. Pu samples must be transported between labs and undergo a lengthy preparation process before the analyte can be introduced into the mass spectrometry equipment. This has garnered a search for an analytical method which can be performed *in-situ* and yield accurate, rapid chemical composition information from plutonium metal. This work builds on an initial proof-of-concept study which implemented a handheld laser-induced breakdown spectroscopy (LIBS) device for chemical analysis of Pu surrogate samples, with the goal of furthering a state of the art analytical spectroscopy method of plutonium analysis. A handheld LIBS device, along with a handheld x-ray flourescence (XRF) device are compared by quantifying their performance detecting gallium in cerium to determine advantages and drawbacks of the two methods. The handheld LIBS was utilized for analysis of Pu alloy samples in a glovebox setting, coupled with chemometric methods, to validate the results seen previously with Pu surrogate material. A full-scale laboratory LIBS setup leveraging a high resolution spectrometer was implemented to maximize data quality and couple the recorded spectra with advanced machine learning paradigms. A machine learning workflow was implemented to optimize several machine learning regression models and determine the superlative analysis method based on sensitivity and precision for Ga quantification. This provided a robust, laboratory scale comparison to the performance of the handheld devices using advanced analytical methods.

1.1 Background

LIBS has been used as a diagnostic technique for a wide variety of applications, and has proven to be a versatile analytical tool. Traditional LIBS setups on the laboratory scale have been used in a plethora of experimental proceedings to include combustion and plasma diagnostics, [1–5], uranium detection [6], detection of nuclear material in varying sample matrices [7–11], and nuclear safeguard applications [12–14]. Recent experimental proceedings have garnered great interest in the application of commercial off-the-shelf (COTS) portable LIBS systems for nuclear material analysis. The SciAps corporation produces handheld Z-series LIBS analyzers, which weigh only a few pounds, cost approximately $40,000 (USD), and are widely used for elemental analysis of scrap and industrial metals [15,16]. A recent study using cerium, a common chemical surrogate for plutonium, proved that the Z500 could effectively quantify the presence of gallium in Ce-Ga alloys [17, 18]. This has paved the way for applying portable LIBS systems for elemental analysis of plutonium samples.

Similarly, XRF is a widely used spectroscopic technique for elemental quantification and chemical analysis. A portable XRF device has been successfully utilized for detection of plutonium contamination in wounds [19]. Additionally, a study by Kirsanov et. al. highlighted the technique for its potential in analyzing complex mixed lanthanides using chemometric techniques [20]. Many handheld XRF devices are commercially available, such as the Bruker S1 Titan series marketed for fast, non-destructive elemental identification for a wide variety of applications including alloy analysis, mineral identification, geo exploration, and consumer safety. This device also has the potential to provide rapid, precise quantification of minor analytes in plutonium alloys in a laboratory or production envrionement.

The study of spectral emission lines of plutonium is much less developed than that of common industrial metals. While data on lines from plutonium in a mixed actinide sample has been tabulated, no thorough studies have been conducted concerning spectral analysis of Pu alloys using a hand-held LIBS device [21]. Quantitative analysis of plutonium is typically conducted in the laboratory environment using plasma spectroscopy techniques, such as inductively coupled plasma - optical emission spectroscopy (ICP-OES). This technique uses plasma to excite a sample and measures light from the de-excitation of the sample atoms [22]. Recent work has demonstrated capability of ICP-OES to identify optical emissions of plutonium; spectral data gathered can be processed and deconvolved for quantitative analysis [23]. While results of high resolution ICP-OES experiments show promise for quantitative analysis of plutonium alloys, the complex equipment requirements and sample preparation process leave a few areas of improvement open for investigation. In contrast, a portable LIBS or XRF device can provide a compact system for rapid spectral data acquisition and elemental analysis. The simplicity of these handheld systems and depth of their commercial capabilities make them ideal candidates for the purpose of plutonium/plutonium surrogate fabrication and quality control.

1.2 Problem

This project can be sectioned into three main problems to investigate:

1. Spectroscopic methodology: To replace conventional analytical methods used for the analysis of Pu alloys, we seek to investigate other atomic spectroscopy methods which could provide rapid elemental quantification. As mentioned, LIBS is a prime candidate for this application. A portable LIBS system will be the main focus of this research; the analytical performance of the Z300 will be compared to that of a standard laboratory LIBS setup with a full-scale laser and spectrograph. Using a more powerful laser and a larger spectrograph with better resolution may improve the performance of the chosen analytical

methods. Additionally, x-ray fluorescence (XRF) will be implemented as a comparison of a related atomic spectroscopy technique.

2. Plasma physics phenomena: A common phenomenon seen in LIBS is self-absorption; a plasma becomes optically thick to certain wavelength emissions and reabsorbs, preventing the detector from reading the true representative intensity of those emissions from a sample. This deleteriously affects calibrations constructed from the self-absorbed spectra. This phenomenon, and potential mitigation strategies, will be investigated as part of this study to improve accuracy of univariate LIBS calibrations.

3. Data complexity: The complex optical emission spectrum of plutonium generates significant interference between Pu emissions and those of any other trace elements in the sample. Therefore, it is imperative to implement advanced analysis techniques to discern the presence of elemental impurities in the spectrum and separate these trace signatures from the bulk Pu emissions. This research seeks to implement both chemometric and machine learning methodologies to create robust prediction models which can accurately quantify the presence of trace elements in a bulk Pu matrix at LoDs comparable to traditional laboratory setups. Creating these models would significantly boost the analytical applications of COTS LIBS devices for nuclear material analysis.

1.3 Hypothesis

This research furthers my initial master's research hypothesis; analytical algorithms can be developed to discriminate between spectral lines originating from different elements in a handheld LIBS spectrum. In order to produce robust, efficient calibration models for predictive elemental analysis, machine learning methods must be implemented. Regression and classification paradigms commonly used in data science can provide optimum solutions for complex spectroscopic problems and outperform traditional analytical techniques. Machine learning can yield predictive models for various trace elements allowing the Z300 to achieve low limits of detection comparable to those of traditional laboratory LIBS setups.

1.4 Approach

Cerium samples are created with varying concentrations of minor analytes gallium and silicon. A handheld LIBS and handheld XRF device are both used to record spectra of the Ce-Ga samples. Univariate calibrations are constructed with both types of spectra and quantification performance is compared with sensitivity and precision metrics. Self-absorption in the handheld LIBS spectra is addressed and corrected. An initial investigation into machine learning models is conducted with the handheld LIBS to quantify Si in Ce-Si samples; precision and sensitivity of the regression models are evaluated. The study of the Ce-Ga samples is then extended to Pu alloy samples; the handheld LIBS is used to quantify different minor metals in Pu samples. Chemometrics are implemented to evaluate different regression techniques for sensitivity and error. Lastly, a lab-scale LIBS experiment using a high-resolution spectrograph is implemented to record spectra of the Ce-Ga samples. An initial univariate analysis is conducted to observe self-absorption effects and calibration quality at different gate delays, and correct the calibrations for self-absorption. A full machine learning experimental design is then implemented to evaluate several paradigms for Ga quantification; these models are tuned with hyperparameter optimization to ascertain the superlative machine learning approach with the highest sensitivity and precision.

1.5 Research Assumptions and Limitations

This study is primarily limited by the design of the Z300. The accuracy of the calibrations made using data collected from the device will depend largely on the resolution, fixed time gating and low laser power of the system. It is assumed that the system resolution of 0.1 nm is enough to resolve differences between the cerium and gallium emission lines to be used in quantitative sample analysis. This study is also limited by the resources available in a laboratory setting and the quality of experimental samples used to build the analytical program. The true composition of the created samples is affected by the accuracy of the various apparati used in their creation, such as the weigh scale for estimating proper weight fractions of each material to yield a particular composition. The sample homogeneity of the powder prior to pellet pressing will affect how representative the recorded LIBS spectra is of the true chemical makeup. This is directly affected by the homogenization mixing process. Additionally, the applicability of the chosen analytical models used for Ce is limited when used for analyzing Pu. Although the spectral responses are similar, Pu has significantly more complex emissions which cannot be fully simulated by Ce. Furthermore, the study of these methods on Pu alloys is limited to the Pu samples we are able to access due to radiation protection protocols and COVID-19 measures enacted in the laboratory.

1.6 Research Contributions

This research will advance the analytical capabilities of COTS handheld elemental analyzers, provide novel analysis of plutonium spectra, and advance existing analytical methods for spectral analysis. Some of the specific contributions are listed as follows:

- **Validating capability of COTS portable LIBS system for plutonium analysis:** This study confirmed that the Z300 LIBS analyzer can be implemented for *in-situ* analysis of trace metals in plutonium metal

- **Providing a new analytical tool for Pu production quality control:** This research developed techniques which can be used to conduct rapid in-situ analysis of plutonium samples at various stages in the pit production process. This provides the DoE with a critically desired capability to assist in meeting the 80 pits per year mission [24].

- **Integrating machine learning paradigms for analysis of actinide LIBS spectra for the first time:** This work examine the efficacy of various machine learning methods seldom seen in analytical spectroscopy. These paradigms produced robust models which could predict the content of various trace elements present in the complex plutonium spectrum. The new machine learning methods outperformed traditional techniques used for spectroscopic analysis, including PCA/PLS and ANN.

- **Overcoming self-absorption with a mathematical correction:** Using a correction methodology based on Stark broadening parameters can mitigate the effects of self-absorption on univariate calibration curves, drastically improving error and sensitivity of these models.

- **Comparing two COTS portable analyzers:** Investigating differences in performance between handheld LIBS and XRF analyzers for trace analyte quantification. This will open the door for exploration of data fusion techniques to increase the precision of predictive regression models.

1.6.1 Research Accomplishments

Awards:

1. Society for Applied Spectroscopy Outstanding Poster Award (SciX 2021)
2. DOE Innovations in Nuclear Technology R&D Award (2021)

Peer reviewed research articles:

1. Pending RSC Technical Note
2. Rao, A.P., Jenkins, P.R., Auxier II, J.D., Shattan, M.B. and Patnaik, A.K. (2022). "Analytical comparisons of handheld LIBS and XRF devices for rapid quantification of gallium in a plutonium surrogate matrix." Journal of Analytical Atomic Spectrometry.
3. Ashwin P. Rao, Phillip R. Jenkins, John D. Auxier, Michael B. Shattan, and Anil K. Patnaik, "Development of advanced machine learning models for analysis of plutonium surrogate optical emission spectra," Appl. Opt. 61, D30-D38 (2022)
4. Rao, A.P., Jenkins, P.R., Vu, D.M., Auxier II, J.D., and Shattan, M.B. (2021). "Rapid quantitative analysis of trace elements in plutonium alloys using a handheld laser-induced breakdown spectroscopy (LIBS) device coupled with chemometrics and machine learning." Analytical Methods, 13, 3368-3378.
5. Rao, A.P., Jenkins, P.R., Auxier II, J.D., and Shattan, M.B. (2021). "Comparison of machine learning techniques to optimize the analysis of plutonium surrogate material via a portable LIBS device." Journal of Analytical Atomic Spectrometry, 36 (2), 399-406.

Conference proceedings:

1. Rao, A.P., Auxier II, J. D., Vu, D.M., and Shattan, M.B. (2020). “Applications of portable LIBS for actinide analysis.” Optical Sensors and Sensing Congress, OSA Technical Digest (Optical Society of America), paper LM1A.2.

Conference presentations:

1. Rao, A.P., Pinson, R. E., Jenkins, P.R., and Patnaik, A.K. (2021) “Applications of laser-induced breakdown spectroscopy for chemical analysis of nuclear materials.” 2021 SciX, September 26-30, 2021, Providence, RI. (Invited talk).
2. Rao, A.P., Jenkins, P.R., Auxier II, J.D., Shattan, M.B., and Patnaik, A.K. (2021) “Development of tree-based machine learning methods for quantification of gallium in a Pu surrogate matrix via LIBS.” 2021 SciX, September 26-30, 2021, Providence, RI. (Poster presentation).
3. Rao, A.P., Jenkins, P.R., Auxier II, J.D., Shattan, M.B., and Patnaik, A.K. (2021) “Decision tree-based methods for chemical analysis of Pu surrogate spectra.” 2021 Fall ACS National Meeting, August 22-27, 2021, Atlanta, GA. (Oral presentation).
4. Rao, A.P, Jenkins, P.R., Auxier II, J.D., and Shattan, M.B. (2020). “Improving analytical performance of a portable laser-induced breakdown spectroscopy device through use of a boosted regression ensemble.” 2020 SciX Annual Meeting, October 12-15, 2020, Virtual (Poster Presentation).
5. Rao, A.P., Auxier II, J. D., Vu, D.M., and Shattan, M.B. (2020). “Applications of portable LIBS for actinide analysis.” 2020 OSA Congress, LACSEA, June 22-26, 2020, Virtual (Oral Presentation).

II. Theory

The development of predictive models for quantitative analysis of trace metals in plutonium alloys requires an understanding of laser-plasma spectroscopy, techniques for chemical analysis of spectral data, and the complex properties of plutonium metal. First, a summary of plasma spectroscopy and the function of the SciAps Z300 is presented. This topic is followed by a discussion of previous work using LIBS for elemental analysis and analysis techniques as well as a technical discussion of the XRF technique. Previous LIBS studies specific to nuclear material analysis are presented, followed by a discussion of plutonium chemistry and metallurgy. Finally, traditional chemometric techniques used for spectral analysis are presented, followed by a detailed discussion of all the machine learning methods implemented in this work.

2.1 Laser Ablation

Laser ablation, depicted in Fig. 1, has traditionally been used to remove material from the surface of a target object. The ablation process itself occurs when short wavelength radiation from a laser beam couples with the material surface. The ablation process is fundamentally dependent on different laser parameters, including wavelength, pulse duration, repetition rate, and beam quality. Laser wavelength affects the energy of the laser photons, which determines the way in which they interact with the atomic matrix of the material. Laser photons with energies higher than the atomic force attracting electrons to the nucleus will liberate these electrons from the atom, causing ablation. This process is defined as a photochemical interaction. Lower energy photons won't liberate electrons from their orbits, but will simply cause them to vibrate, causing molecular dissociations. If many such photons are incident on the atomic matrix of a material over time, the cumulative vibration is imparted as thermal energy. This interaction, called photothermal coupling, can also be used to remove electrons from the atomic matrix of a material [25].

Pulse duration and repetition rate affect the thermal characteristics of the ablation. Shorter pulses minimize thermal damage to the area surrounding the ablation event, and higher laser repetition rates enable maintaining a constant ablation temperature, preventing heat waste. Beam characteristics such as size, focus, and homogeneity are all factors affecting the ablation efficiency. These parameters must all be carefully evaluated prior to experimental data collection in order to perform successful ablation of a selected material. Typically, ablation blows material off the surface of the target in the form of a gas. At higher laser fluxes, the ablated material interacts with a trailing portion of the laser pulse, further ionizing the ablated material. This ionization creates a plasma of the ablated surface material, forming what is referred to as a laser-induced plasma.

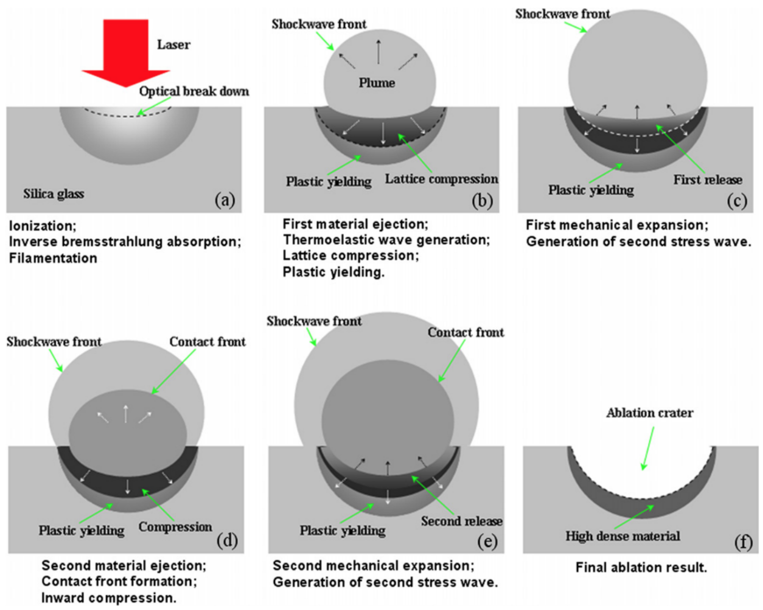

Ionization;
Inverse bremsstrahlung absorption;
Filamentation

First material ejection;
Thermoelastic wave generation;
Lattice compression;
Plastic yielding.

First mechanical expansion;
Generation of second stress wave.

Second material ejection;
Contact front formation;
Inward compression.

Second mechanical expansion;
Generation of second stress wave.

Final ablation result.

Figure 1. Breakdown of laser ablation process stages [26].

The general process of a laser ablation event is depicted in Fig. 1, describing the ablation of silica. Initially, the incident laser photons deposit part of their energy on the surface of the material, while part of the energy is absorbed through various ionization processes (multi-photon, inverse Brehmstrahlung, avalanche), creating the laser plasma. Next, material heated by the laser is ejected away from the target site. This heated mass transfers heat to the surrounding air, compressing it to create a shockwave front. Additionally, pressure induced by the laser forms a thermoelastic wave, which propagates as a pressure wave. This second stress wave further compresses material at the target site, leading to a second ejection and the formation of the contact front. As this front expands, further compression of the ablation site occurs and a third stress wave is generated. At the end of the ablation process, the target site is left with an ablation crater filled with highly dense material formed from the compressions [26]. While this process occurs in the material, the plasma plume is expanding as a result of the shock front propagation. As it expands, the plasma begins to cool and recombine, leading to optical emission from various atomic shell transitions. The exponential temperature decrease is described in Fig. 2.

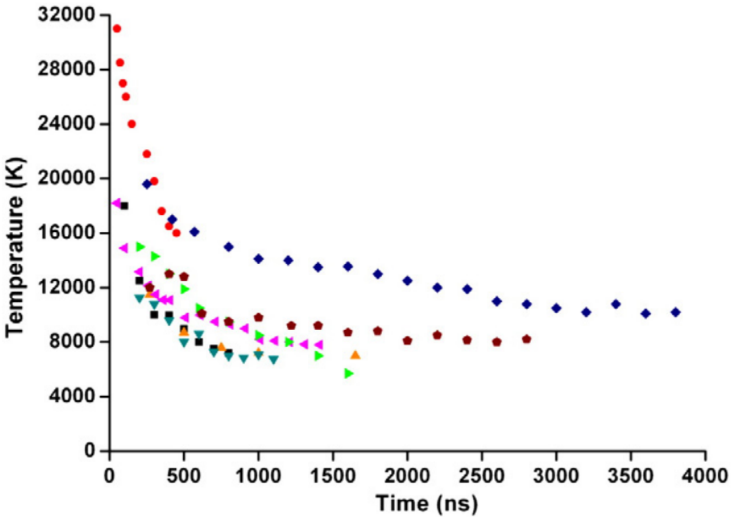

Figure 2. Example of temporal evolution of laser-induced plasma temperature [26].

As the ions and electrons recombine and the collision rate of the plasma slows, the temperature decreases to an asymptote over the period of a few thousand nanoseconds. Eventually, all the constituent particles of the plasma recombine. In pulsed LIBS, the entire process described above is repeatedly cyclically between each laser pulse incident on the target material. For the purpose of material composition identification, a pulsed laser at a lower power and small beam diameter can be used to interrogate and collect data on a sample material with minimal damage beyond the ablation point on the surface.

2.2 Laser-Induced Breakdown Spectroscopy (LIBS)

LIBS is an analytical process which extends the laser ablation technique to excite the atoms of the target material when it is vaporized by the laser energy. This occurs when material blown off by the ablation is vaporized, forming a plasma plume. Atoms within the plume absorb laser photon energy; this leads to the excitation of electrons to higher level energy states. As the plasma cools, these electrons de-excite and return to their ground state configurations; this results in the emission of a de-excitation photon with a wavelength corresponding to the energy lost in the electronic transition. A simple rendering of this process is shown in Fig. 3.

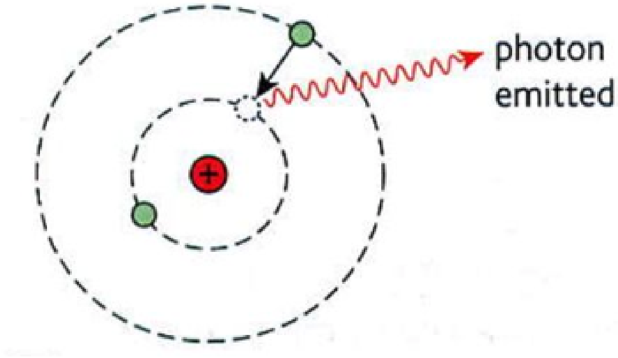

Figure 3. Basic rendering of the atomic de-excitation process [27].

De-excitation photon emissions from a plasma are characteristic of the specific energy level transitions of a particular atom. An example energy level diagram (ELD) is shown below for helium, along with different possible atomic transition paths. As evident from the figure, one element may emit photons at multiple wavelengths characteristic of one type of transition; some of these transitions are more probable than others.

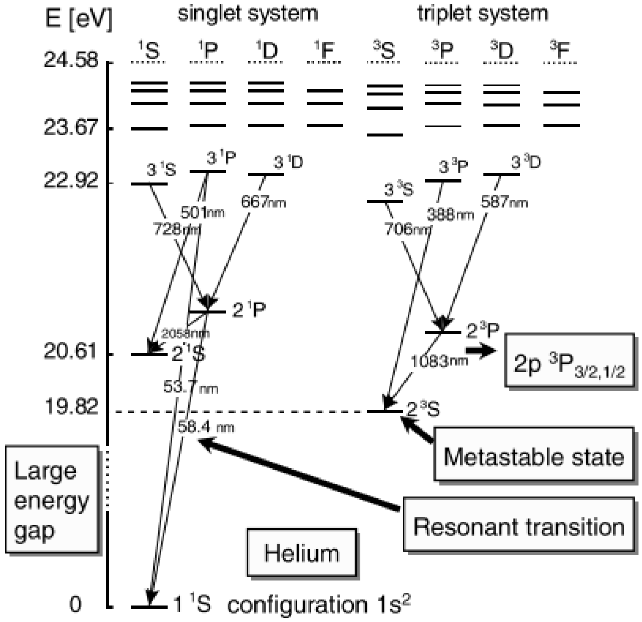

Figure 4. Atomic energy level diagram for Helium [28].

Resonant transitions refer to transitions linked to the ground state; these transitions are favorable with high probabilities, and therefore the emitted radiation is generally intense. Radiation in the visible spectra used for optical emission spectroscopy generally originates from transitions between different excited states [28]. The wavelength (λ_0) of the photon emitted from a transition can be calculated from the energies of the transition states as given in Eq. 1, where h is Planck's constant, c is the speed of light, E_p is the lower level and E_k is the upper level.

$$\lambda_0 = \frac{hc}{E_p - E_k} \tag{1}$$

The intensity ϵ_{pk} of the emitted light is a function of the particle density ($n(p)$) and the transition probability (A_{pk}), and can be quantified as described in Eq. 2.

$$\epsilon_{pk} = n(p)A_{pk}\frac{hc}{4\pi\lambda_0} \tag{2}$$

The spectra of emitted light from a plasma can be recorded using a spectrometer. Emitted light directed into a spectrometer is collimated and focused onto a diffraction grating, which disperses the light into its different constituent wavelengths. The diffracted light is then reflected off a focusing mirror and can be directed onto a detector, such as a CCD camera, to be recorded. The monochromator, shown in Fig. 5, is a commonly used spectrometer which can be coupled to a plasma experiment to record spectral emission of a particular narrow band of wavelengths. To record a larger bandwidth, some spectrometers do not use an exit slit, and instead direct all the diffracted light straight to a detector.

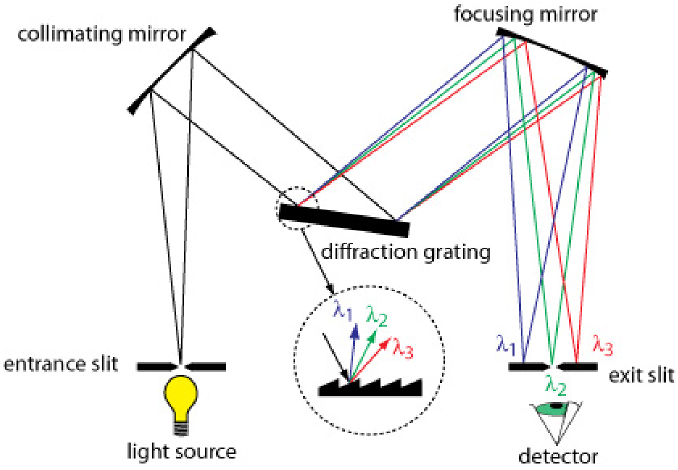

Figure 5. Schematic of Czerny-Turner style spectrometer [29].

The complete LIBS process, depicted in Figure 6, brings the atomic de-excitation and spectrometry processes discussed above. The optical emission generated by a laser-produced plasma can be focused and directed into a spectrometer, dispersing the light into its different wavelengths. The dispersed light can then be detected using a camera, and the intensities of the various wavelengths can be recorded. Strong spectral emissions characteristic of particular atoms in the laser-ablated sample show up as peaks in the spectrum; analysis of these peaks can yield different information about the sample itself.

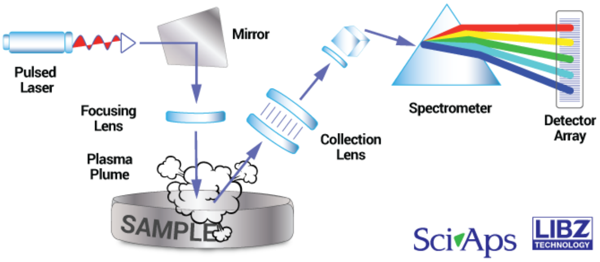

Figure 6. Schematic diagram of LIBS setup [15]. A pulsed laser ablates the sample surface; the recombination of particles in the resulting microplasma produces photons which can be captured by a spectrometer and recorded by a CCD camera. This spectra can then be analyzed to determine sample composition.

2.2.1 Self-absorption

The phenomenon of self-absorption is often evident in optically thick laser-produced plasmas (LPPs), and can be fundamentally detrimental to quantitative analyses built with LIBS spectra affected by this phenomenon. In self-absorption, the hotter interior of the plasma preferentially emits wavelengths of resonant transitions. As these resonant emissions travel to the colder periphery of the plasma, they are reabsorbed before they can escape to the detector system. This is particularly detrimental for LIBS measurements, as many major LIBS emissions stem from resonant transitions. For quantitative analyses relating emission peak intensity to analyte concentration changes in a sample, the presence of self-absorption can reduce the linearity of the relationship between intensity and concentration, ultimately reducing the efficacy of calibration curves created with the peak intensity data. The degree of self-absorption can vary based on the transition parameters of the particular line being observed, as well as on properties of the plasma related to the optical thickness such as the electron density and temperature distribution. Higher degrees of self-absorption can affect recorded emission peaks in different ways.

In an optically thick plasma, the number of ionized emitters can directly affect the self absorption behavior, as illustrated in Fig. 7. This diagram shows the Cu I 324.7 nm emission behavior changing with different emitter number density (electron density). As number density increases, the emission peak intensity also begins to increase, but the behavior is markedly nonlinear as self-absorption begins to take effect. Peak broadening is evident after a density of N = 10^{15} cm^{-3} is reached; peak flattening begins to occur as well when the blackbody limit is reached at N = 10^{17} cm^{-3}. When N < 10^{15} cm^{-3}, the line profile is distinctly Lorentzian, corresponding to an optically thin plasma. This result is important to reference for LIBS studies, as a denser plasma may have higher intensities of critical emission lines, but may be marred by self-absorption effects that can reduce overall calibration fidelity.

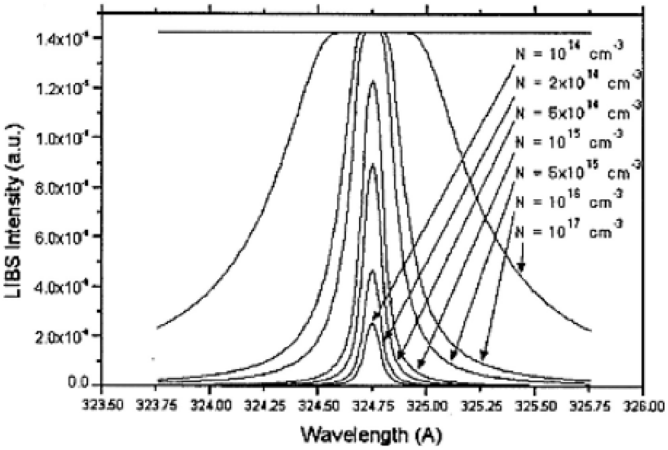

Figure 7. Diagram taken from Bulajic *et. al.* showing how increasing emitter density exacerbates the effects of self absorption on a peak, leading to broadening and eventual peak flattening [30]

It is known that the dynamics of the plasma plume during expansion and cooling have a significant effect on the optical thickness and self-absorption effects. The observed self-absorption can then be strongly dependent on the acquisition delay time (gate delay), as this parameter controls the period in the plasma lifetime at which atomic emissions are recorded. Previous studies have suggested an inverse relationship between the gate delay and the measured self-absorption, as depicted in Fig. 8. This data depicts the SA coefficient change for two neutral Al emissions over an 18 μs period; as the gate delay is increase the SA coefficient decreases, indicating increasing self-absorption. The current explanation for these observations is that as the plasma cools with time, states with lower excitation energies become relatively more populated and can reabsorb more radiation. In particular, the periphery of the plasma cools at a quicker rate than the inner plasma, thus leading to higher probabilities of radiation re-absorption at later times. Most current studies investigating this behavior have only examined lines of common lighter metals with transitions terminating on lower energy levels. Therefore it should be noted that transitions between higher-lying energy levels behave differently, and have different temporal evolution of self-absorption effects.

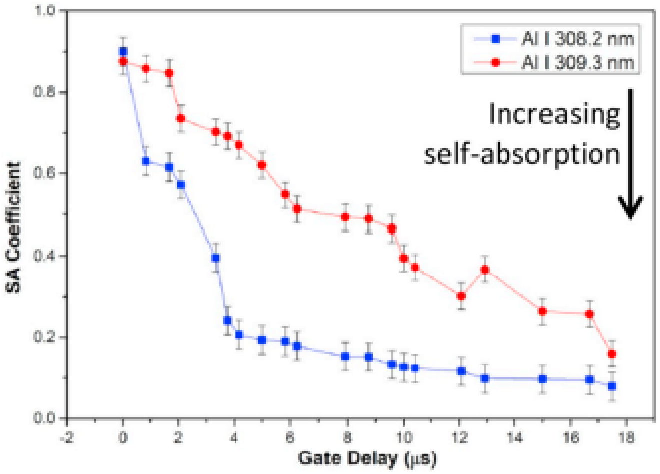

Figure 8. Diagram taken from Rezaei *et. al.* illustrating effects of gating parameters on self-absorption of Al peaks [31].

Lastly, it is worth mentioning that the self-absorption effects in spectra of Pu alloys or surrogate materials has not been extensively studied. In particular, the degree of opacity of an LPP of this characteristic material is not known. Alloying metals used in Pu, such as Ga, have major atomic transitions to the ground state level. The Ga I 417 nm emission transitions to the $^2p_{3/2}$ level of the ground shell [32]; while not a completely resonant transition its proximity to the ground state presents the potential for this emission to be absorbed by the LPP. It is important to keep in mind that optical thickness does not manifest simply as a "present or not present" phenomenon, rather it can appear at different levels. Prior to the advent of LIBS, initial studies on self-absorption were conducted on emission profiles of arcs and sparks. The results of this investigation formulated a relation for emitted radiation intensity dependent on an absorption parameter, p. A non self-absorbed line is characterized by $p = 0$, as shown in the most prominent peak of Fig. 9. Values of p larger than 0 indicate some

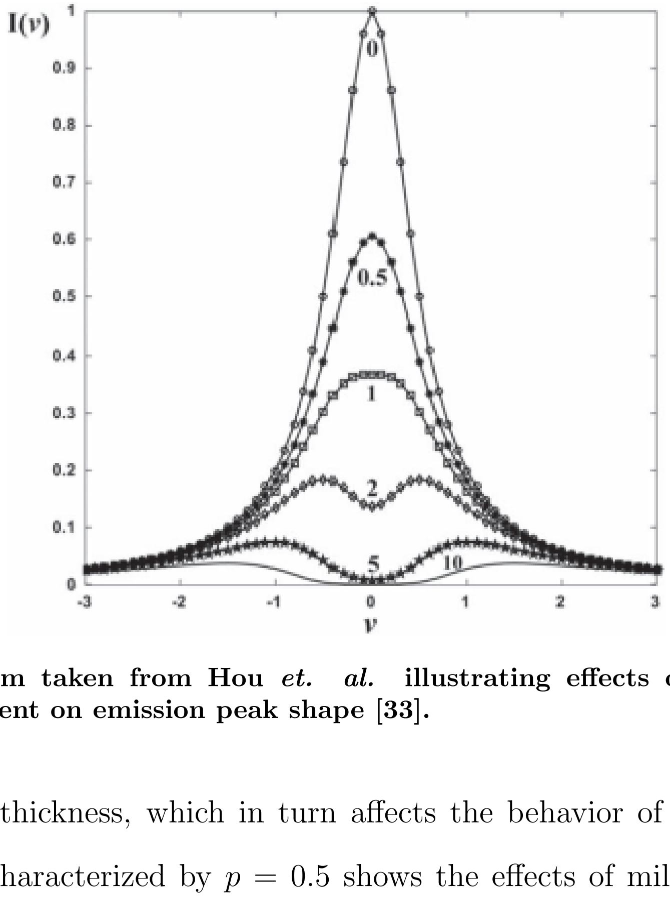

Figure 9. Diagram taken from Hou *et. al.* illustrating effects of increasing self-absorption coefficient on emission peak shape [33].

degree of optical thickness, which in turn affects the behavior of the emitted line. The second line characterized by $p = 0.5$ shows the effects of mild self-absorption; the line profile and shape has not changed from the non self-absorbed condition, but the intensity has decreased due to the reabsorption of some radiation by the plasma. The effects of mild self-absorption are of importance to calibration curve LIBS studies as they can affect the fidelity of the curves by reducing the linearity of the relationship between line intensity and analyte concentration. This can sometimes be hard to discern since there is no change in line shape, but tracking the intensity across analyte concentration range can reveal the presence of this $p < 1$ opacity. Moderate self-absorption effects begin to appear at $p > 1$, as the emission line profile becomes less Lorentzian and broadens at the wings. Additionally, the blackbody limit is reached at these more moderate levels of opacity, and the peak begins to flatten at the top. Severe levels of self-absorption, seen at $p \geq 2$ show the phenomenon known as self-reversal, wherein the peak intensity begins to decrease downwards while the wings remain the same, causing a ”valley” to appear at the peak centroid. The varying degrees of self-absorption can affect calibrations built from peak intensity measurements in different ways. In general, non-linear changes in intensity with respect to analyte content will decrease the slope of a calibration and reduce the calibration sensitivity. This study will investigate the occurence of this phenonemon in the cerium-gallium emission spectra by quantifying the self-absorption effect and attempting to correct the calibration curves mathematically to boost precision and sensitivity.

2.3 X-ray Flourescence (XRF)

XRF applies a collimated beam of x-ray photons at the surface of a target in order to knock an inner shell electron from its position in the shell of surface atoms. Another electron from a higher energy level de-excites to fill the inner shell vacancy; this de-excitation then emits an x-ray photon. Different materials fluoresce at different wavelengths characteristic of their constituent atoms, and a spectra can be recorded to conduct elemental composition analysis of experimental samples [34]. Fig. 10 illustrates the fluorescence process in a simplified manner. XRF is a common technique used in chemical analysis of various substances, and is similar to LIBS in efficiency, resolution, detection limits and time required for sample analysis. XRF also requires little to no sample preparation. Additionally, LIBS is semi-nondestructive and preserves the bulk sample while leaving small ablation craters on its surface, but XRF is completely non-destructive and does no physical damage to the sample surface. Hand held XRF devices are commercially available, with detection speed and accuracy comparable to a portable LIBS device [36]. Previous research has proven the effectiveness of XRF for rapidly quantifying Pu surrogate contamination in wounds [19]. Some studies have been conducted evaluating XRF for use in quantifying lanthanides in rare earth rice ores and mixed lathanide materials [20, 37]; these experiments found significant interferences between lanthanide and trace element emissions in samples and noted that calibration curve quality could be hampered by poor signal-to-noise ratios of the recorded spectra, making the analysis of Ce potentially challenging. One particular drawback of portable XRF devices lies in their inability to detect elements lighter than magnesium. Elements with Z < 11 will typically only emit K-shell emissions due to the lack of larger electron shells. This means that an inner shell electron

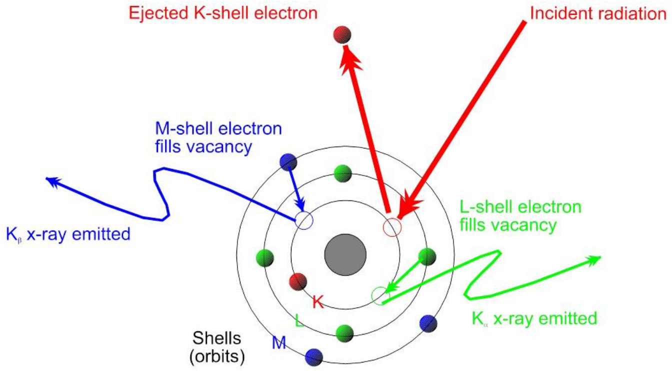

Figure 10. Diagram of the x-ray fluorescence process. Incident radiation ejects an inner shell electron; an outer shell electron fills the vacancy and a characteristic x-ray is emitted by the de-excitation [35].

is ejected and an electron from the L or M shell fills its place. Since these lighter elements only have 2 electron shells (s and p), they will typically only emit lower energy K_α x-rays rather than higher energy emissions corresponding to transitions between higher energy shells seen in heavier elements. These lower energy emissions are often reabsorbed in the electron cloud and fail to escape the material to the x-ray detector. Those that do escape are often attenuated in the space between the air and the detector itself. A very sensitive detection setup is required to record these K-shell fluorescence emissions from lighter elements, and portable devices do not have this capability.

2.4 Nuclear Material Analysis *via* LIBS

Previous work using Z series LIBS analyzers has confirmed lanthanide and actinide quantification capabilities of the hand held device. A prior study by Shattan *et. al.* examined the Z500 for quantification of uranyl flouride in sand by taking spectra from samples varying from 1 to 39.5 weight percent UO_2F_2 [16]. Figure 11 shows the variation in the spectra of the 409.1 U(II) peak height over different concentrations of uranyl flouride (UO_2F_2) mixed with sand [16]. It is expected that

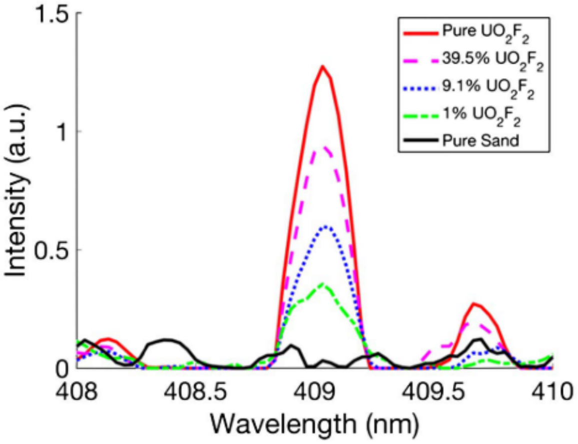

Figure 11. U(II) 409.1 nm peak for varying uranyl fluoride concentrations [16].

as the uranium concentration in the sample decreases, the line intensity decreases since less of the transitions emitting the 409.1 nm line are occurring. Calibration curves were built using intensities of each uranium line selected for all sample concentrations, an example calibration curve for the U II 409.1 nm line is shown in Figure 12. The fitted line to the datapoints gives the calibration curve which can be used to determine concentration of an unknown sample once the appropriate line ratios has been calculated. This technique can be applied to Ce-Ga alloys as well, allowing the creation of a calibration curve for the plutonium surrogate. An additional study conducted by Manard et. al. [38] demonstrates how portable LIBS can be used to discriminate rare earth metals in a uranium matrix. Here, a Z500 was able to detect Eu, Nd, and Yb in levels up to hundredths of a percent in a uranium oxide powder. These results indicate that the HH-LIBS device is capable of detecting dopants in a bulk actinide compound matrix and also show promising potential for the Z500 device to discriminate and identify gallium in a cerium, or even plutonium matrix.

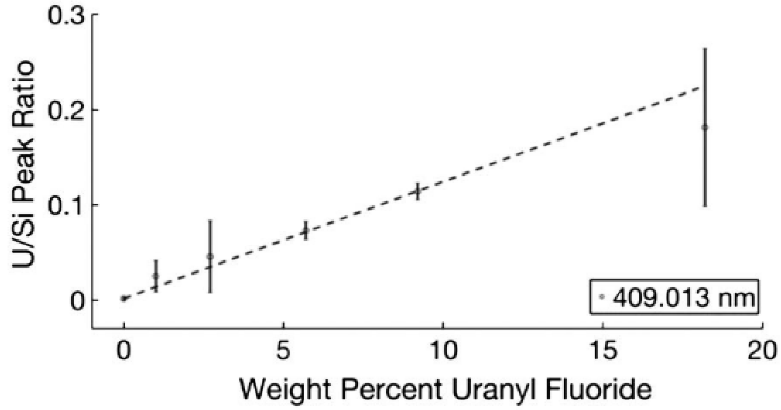

Figure 12. Calibration curve for the U II 409.1 nm line [16].

Finally, recent work conducted by the author using the Z500 developed the groundwork for analysis of Pu by conducting experiments on cerium alloys [18]. This study examined the capabilities of the portable LIBS system for quantifying gallium present in Ce-Ga alloys. The primary challenge of this analysis was discriminating atomic emissions of gallium from the complex spectrum of the bulk cerium; an example spectrum taken from a cerium oxide sample is shown in Fig. 13.

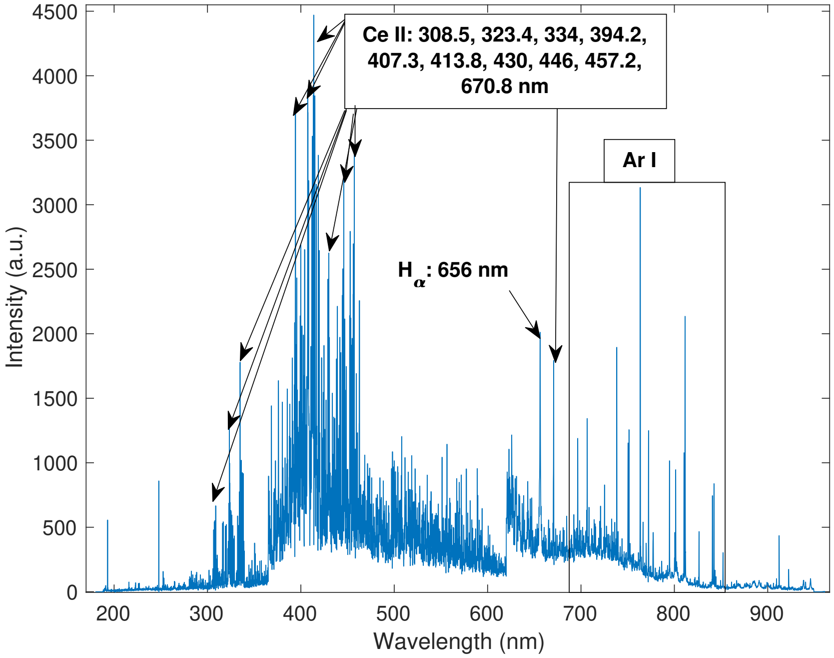

Figure 13. CeO_2 spectra from hand held LIBS device with Ce II lines identified.

The two minor Ga I emissions at 287.4 and 294.4 nm were extracted from the Z500 spectra and used for initial spectroscopic analysis. These are shown in 14; this data demonstrates a clear dependence on Ga signal intensity with Ga concentration of the sample. The result indicates that the handheld LIBS device can register changes in concentration based on spectral data and would be sensitive enough for the construction of regression models.

The accomplishments of this initial work are listed below:

- **Univariate calibration analysis for quantification of Ga in Ce:** Using univariate line calibration fits to different ratios of Ga and Ce emission line intensities, an LoD for Ga up to 0.3 wt% was achieved.

- **Implementation of chemometrics for Pu surrogate analysis:** Multivari-

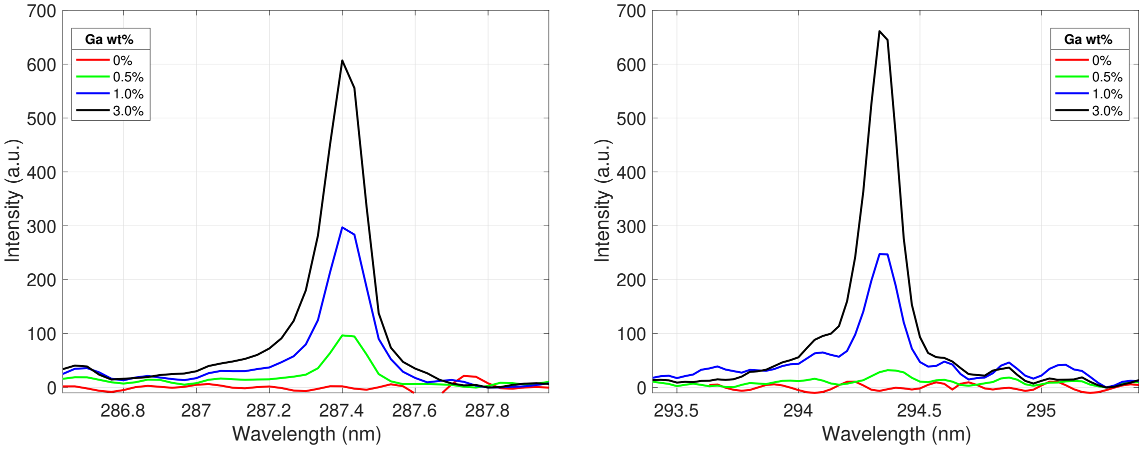

(a) **(b)**

Figure 14. Two of the minor Ga I emission peaks at a) 287.4 nm and b) 294.4 nm, showing the increase in emission intensity of the peak as the concentration of the Ga in the sample increases.

ate regression, principal components regression and partial least-squares regression techniques were implemented to build the groundwork for more robust predictive models for determining Ga content. A 2-factor multivariate regression drove the LoD down to 0.2 wt%. PCR and PLSR models yielded root mean square errors (RMSEs) of 0.7 and 0.2, respectively.

- **Evaluation of portable LIBS device for conducting surface mapping of variation in Ga content:** A modified laboratory setup was built for the Z500 to analyze points along the surface of a cerium alloy sample. The spectral data was used in conjunction with the multivariate calibration model to visually depict variations in the gallium distribution along the surface of the sample.

A visual depiction of the surface Ga content generated with the data from the Z500 is shown in Fig. 15.

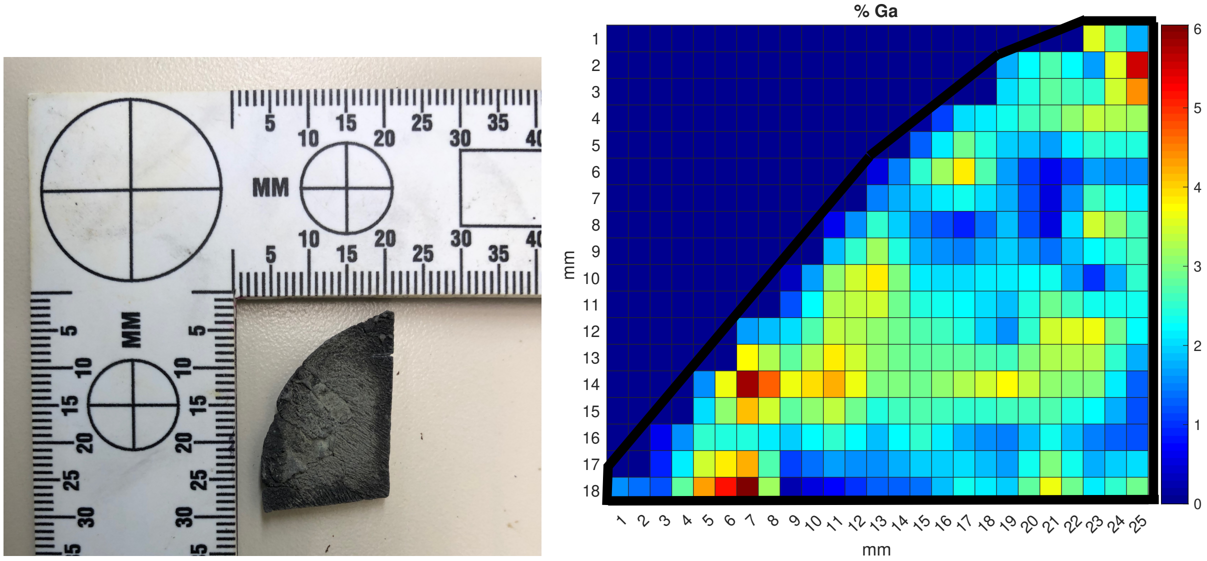

(a) (b)

Figure 15. (a) Photograph of the 3% Ga cerium alloy sample used in the mapping analysis and (b) surface Ga concentration map of the sample. The color map represents the localized weight percent of gallium ranging from zero to six percent.

2.5 Plutonium Metallurgy

Plutonium is a critical material used in the manufacturing of pits of modern nuclear explosive devices. Due to the complex chemical and physical properties of plutonium metal, a variety of procedures must be implemented to form a pit from raw plutonium. One particular property crucial to plutonium manufacturing is the phase behavior of Pu metal across different temperatures. Plutonium metal exists in many different material phases, or allotropes, defined by different arrangements of the atoms in the crystal lattice of the metal. The mechanical and thermal properties of plutonium vary widely between the different phases; understanding the phase chemistry of Pu metal is critical to weapon core design and nuclear forensics. This particular property of plutonium makes it extremely sensitive to phases in temperature and allows for large changes in atomic volume between phase transitions [39]. Fig. 16 shows the change in atomic volume of plutonium with temperature, along with the various phase ranges and transition points. Upon extraction from reprocessed uranium fuel,

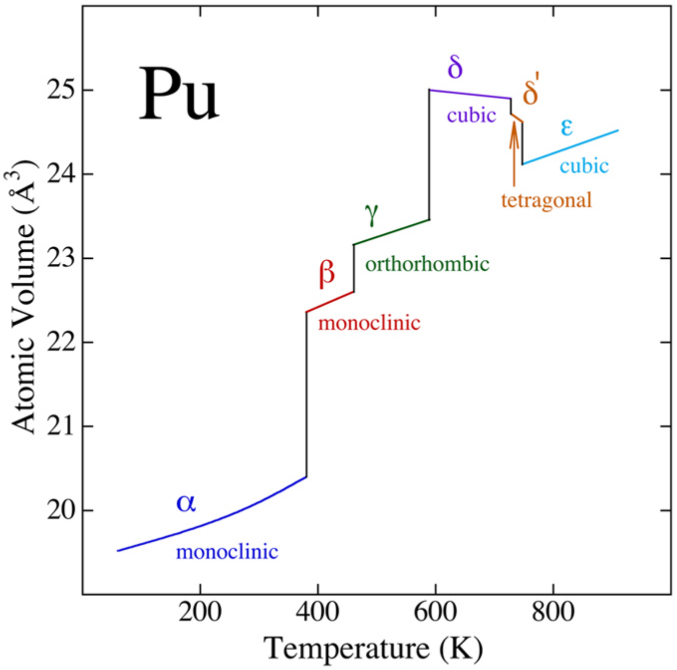

Figure 16. Atomic volume change over various temperatures for known Pu allotropes [39].

plutonium is found in the alpha phase, which exhibits a simple monoclinic crystal structure. As a result, it is brittle, weak and not easily compressed or machined. Additionally, it is susceptible to large changes in atomic volume over small temperature fluctuations. Both of these properties make it far from ideal for manufacture and use in a weapon pit. The beta (body-centered monoclinic) and gamma (face-centered orthorhombic) exhibit similar behavior as the alpha phase. The delta phase of plutonium can be reached by heating up Pu metal within 310 to 452 Celsius. This phase exhibits face-centered cubic (FCC) crystal structure, and is much less sensitive to volume changes due to temperature fluctuation. Additionally it behaves more like a traditional metal, and has a comparable strength and malleability to aluminum. Pu metal in this phase is easily machined and formed into different shapes [40]. In order to stabilize delta phase Pu at room temperatures, the Pu metal must be heated and then alloyed with a dopant [40,41]. The most common alloying metal used is gallium. A phase diagram of Pu-Ga up to 12 atom percent Ga concentration is shown in Fig.

17. The phase diagram indicates that alloying larger percentages of Ga with Pu

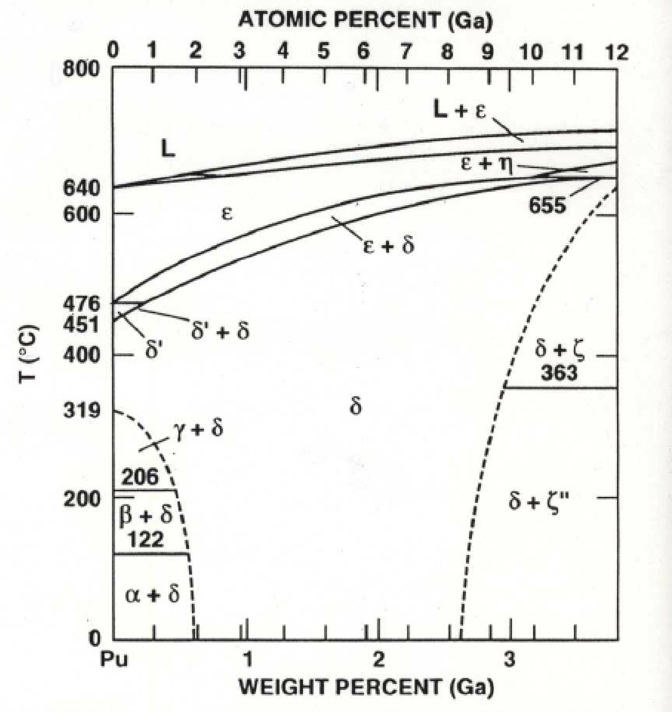

Figure 17. Pu-Ga alloy phase diagram [41].

allows for delta phase stabilization across a wider range of temperatures. This allows for the alloyed plutonium to undergo a variety of machining, casting, or forming processes upon cooling back down to room temperature. Enabling the machinability of Pu metal is key to nuclear component production, and highlights the importance of having a proper alloying process in place on Pu component production lines.

Pu-Ga alloys are made by adding a certain amount of gallium to a mass of molten plutonium to achieve the desired weight percent of Ga. Gallium segregates itself in plutonium, forming rich grain centers and lean grain boundaries, as shown in Fig. 18. In order to diffuse the gallium through the plutonium, the alloy must be annealed at a temperature in the delta phase transition region. This homogenization process stabilizes the lattice structure of the alloy. Upon cooling, the alloy stabilizes in the FCC configuration of delta-phase Pu, making it ideal for undergoing various

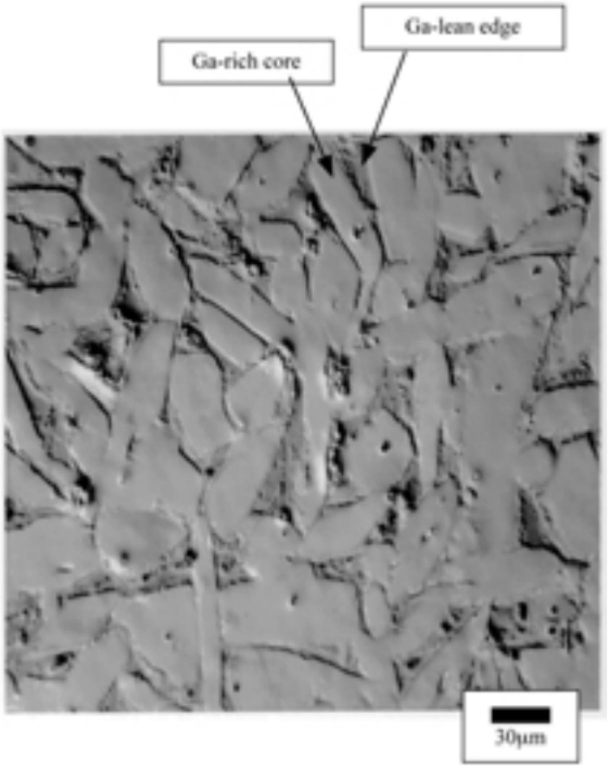

Figure 18. E-probe image of Pu-Ga alloy [42].

machining, casting or forming processes [40].

2.5.1 Cerium as a Plutonium Surrogate

While conducting experimental LIBS measurements of plutonium alloys can yield valuable data, plutonium is relatively hard to access compared to other radioisotopes. However, conducting LIBS measurements of similar metals can provide more easily accessible results and help characterize the possible LIBS signatures of an actual Pu-Ga alloy. Cerium, a lanthanide metal, is a commonly used chemical surrogate for plutonium [43, 44]. Fundamental links between cerium and plutonium have been reported in several studies. Both metals have low melting points, asymmetrical crystal lattice structures, and multiple allotropes which exhibit large volume changes with phase transformations. The similarities in properties has been attributed to the fact that f-shell electrons in both elements are in transition to a localized state [42]. Fig. 19 shows the E-probe image of a Ce-Ga alloy; this alloy exhibits the same segregation behavior as seen in Pu-Ga in Fig. 18. The similarities between cerium and plutonium have made cerium compounds a popular choice for use in experimental work to overcome many of the laboratory hazards of working with plutonium. Cerium compounds such as cerium oxides have been studied extensively as an experimental substitute for plutonium oxides, and the comparative behavior of both compounds in different experimental conditions has been documented in literature [42–45]. This work will examine LIBS spectra of both Ce-Ga in metal and oxide forms and develop a base of analytical measurements which can be extended to Pu-Ga alloys.

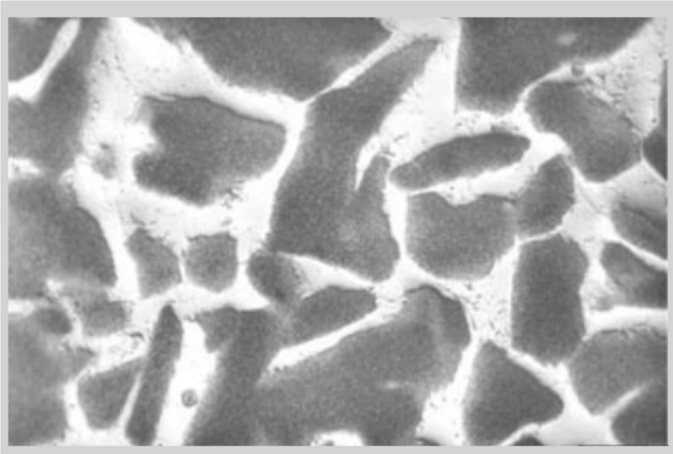

Figure 19. E-probe image of Ce-Ga alloy [42].

2.6 Chemometric Methods for Analytical Spectroscopy

2.6.1 Univariate Analysis

Univariate analysis generates a simple regression model relating changes in intensity of an emission line, or intensity ratios of emission lines, to changes in analyte concentration across a sample set. A simple linear regression fit to these data points generates a calibration curve describing the sensitivity of the spectral response to

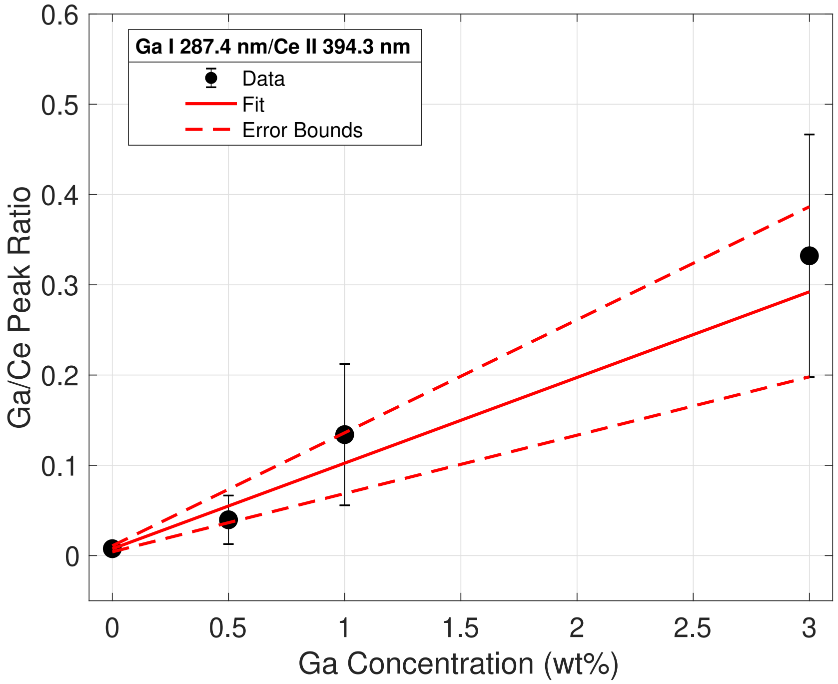

Figure 20. Calibration curve based on intensity ratios of emissions from Ga I 287.4 nm to Ce II 394.3 nm.

the concentration. The univariate calibration method works best when the emission line of interest can be extracted from a simple, well-resolved spectrum without interferences from other nearby emissions. LoDs based on univariate calibrations are directly dependent on the sensitivity (slope) of the calibration; this often results in univariate calibrations producing unreliable and less accurate regression models from complex spectral data. This is evident in Fig. 20, produced during the analysis of cerium-gallium alloy spectra in previous Master's thesis work. It is important to note the high uncertainty in the data points corresponding to higher Ga concentrations; increased shot-to-shot deviation in recorded spectral intensity contributes to an overall higher standard deviation of the lines being used in a univariate calibration. This can lead to inferior regression fit to the calibration data, producing a poor model for prediction.

2.6.2 Multivariate Analysis

Multivariate analysis techniques seek to use multiple variables in a data set to quantify relationships between samples. Multivariate methods are often implemented in analytical chemistry, commonly referred to as chemometrics; these techniques seek to implement advanced statistical methods for analysis of chemical data. Chemometrics is extremely useful in processing of LIBS data, due to the complex nature of spectral responses and the large number of variables present [46–51]. Two commonly implemented methods for ascertaining chemical information from LIBS spectra are principal components analysis (PCA) and partial least-squares (PLS).

PCA is a statistical analysis technique used to reduce the dimensionality of a complex data set by creating a smaller set of variables describing the variance in most of the original data [52, 53]. PCA algorithms are commonly used in the LIBS community to identify significantly varying spectral lines in crowded spectral data sets and analyze only the factors causing variations in the data [8, 47–51, 54, 55]. PCA uses matrix algebra to construct linear combinations of the original data set vari-

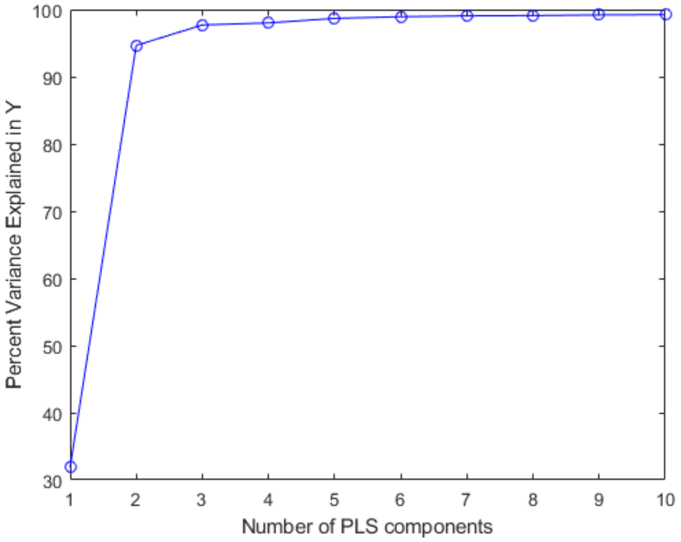

Figure 21. Percent of explained variance in data set vs. principle component number.

ables, called principal components (PCs). Each PC is uncorrelated, but most of the information in the data set is compressed into the first few PCs. Each component explains a percentage of the total variance of the overall data set; this can be graphically represented in order to determine how many PCs are needed to represent the data set. An example is shown in Fig. 21. PCA outputs two information matrices for each PC: loadings and scores. Loadings describe correlations between the variables, as well as their relative contributions to the data set. Scores quantify patterns and correlations between samples in the data set itself. Examining the relationship between loadings values and emission wavelengths of LIBS spectra can identify the emission lines causing the most variance in the data set, and aid in variable reduction. Fig. 22 shows how wavelengths of different metals in a LIBS spectra load on the first PC of a decomposed LIBS data set. The plot indicates that Mg, Si, Al, and Ca emissions contribute to most of the variance of the data set. While loadings are useful for discriminating sample elements and representing variable correlation, PCA scores plots can represent patterns and resolve differences in the sample distribution.

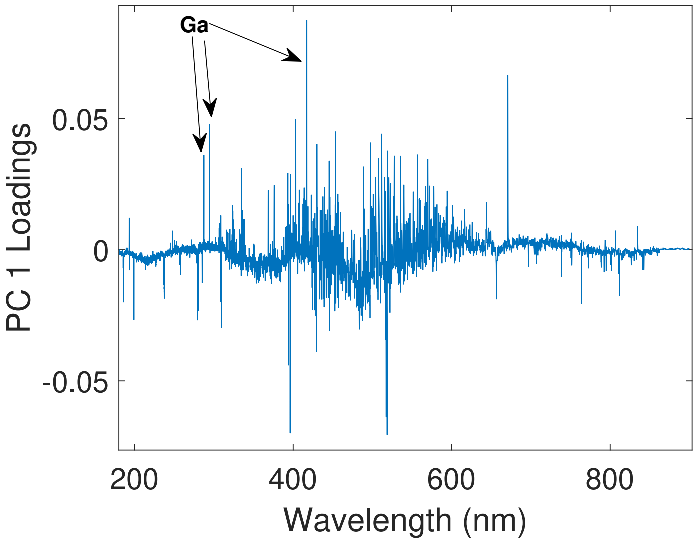

Figure 22. Example PC loadings of LIBS spectra of Ce-Ga. The Ga emissions vary significantly in the data set and have higher loadings values, as marked by the annotation.

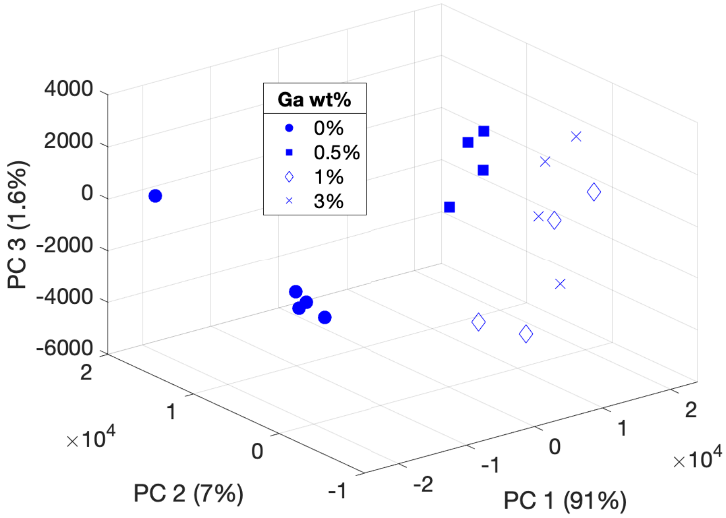

Figure 23. Principle component scores comparison between PC 1, PC2 and PC 3. Clustering based on Ga concentration is evident.

Fig. 23 represents the first three PC scores; the data points are identified by the Ga concentration of the sample from which they were taken. This 3D plot of the scores can be rotated to observe different patterns and features that are similar in the sample set.

PLS regression is a technique which combines features from ordinary multivariate regression and PCA, and is another commonly used technique used to analyze complex LIBS spectra of a limited sample set [7,51,54,56,57]. A PLS regression builds a model predicting an outcome from predictor variables in order to describe their common structure. PLSR finds a set of components called latent vectors, which decompose the predictor and outcome matrices such that the information contained within the latent vectors explains as much of the variance between the predictors and outcomes as possible. A regression then decomposes the predictor matrix in order to determine outcome.

At the simplest level, PLS analysis involves generating a regression model which correlates the LIBS spectral data (X) to elemental concentrations (Y) as described in

Eq. 3.

$$Y = XB \tag{3}$$

B represents a regression coefficients matrix describing the relationships between the spectral emission intensities and the elemental concentrations (response). Comparing the regression coefficients to the predictor variables (wavelengths) generates a plot similar to the loadings comparison depicted in Fig. 22. This allows for discrimination of the important variables in the data set, as noted in Fig. 24. The PLS algorithm then uses a linear combination of values to relate the variation in the spectra with the elemental compositions using a familiar linear equation:

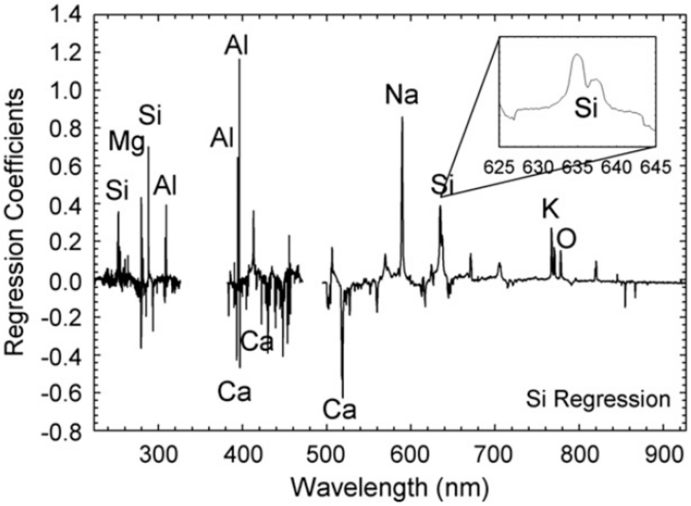

Figure 24. Comparison of PLS regression coefficients to wavelength variables from data set. The behavior of the coefficients clearly identifies which emissions contribute to the variation in the data [7].

$$Y = b_0 + b_1X_1 + ... + b_kX_k \tag{4}$$

In Eq. 4, Y refers to the elemental composition variables, and the b terms represent regression coefficients for the corresponding emission wavelength X. This regression model can be used to determine elemental concentrations using spectral data taken from a sample of unknown composition. PLSR often yields higher fidelity regressions compared to PCR. This is due to the supervised nature of PLS in contrast to the unsupervised nature of PCA; PLS generates data accounting for the covariance between the input and output variable. More specifically, the latent variables generated by PLS also account for explained variance in the output data. This allows it to fit trends in the input to the target output more accurately using the same number of components. This improved fit is demonstrated in Fig. 25, which shows both regression methods fitting LIBS data to predicted concentrations of gallium in cerium alloys [18]. The corresponding fit metrics are shown in Table 1. The supervised nature of PLSR yielded significantly lower root mean-squared error (RMSE) and higher linearity (R^2) of the fit, indicating superior precision of the PLSR model.

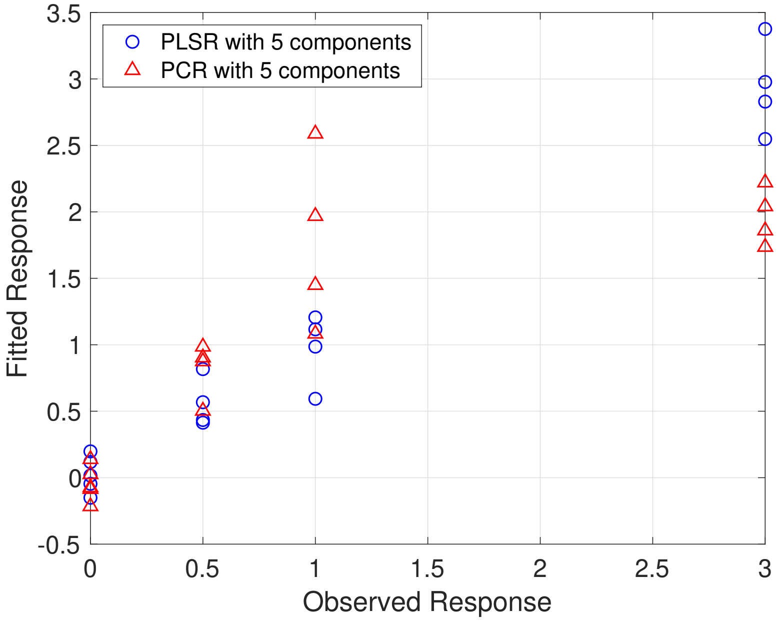

Figure 25. Comparison of measured and predicted Ga concentration using PCR and PLSR models.

Table 1. RMSE and R^2 values of PCR and PLSR models

	PCR	**PLSR**
RMSE	0.716	0.216
R^2	0.603	0.964

2.7 Machine learning (ML) Methods for Analytical Spectroscopy

While the aforementioned traditional methods of spectroscopic analysis have been implemented for spectroscopic regression problems in various fields, the complex nature of the spectra of lanthanide and actinide metals limits their usage for creating high-fidelity predictive models. The complex electronic structure of metals like plutonium yields a plethora of possible emission wavelengths that are recorded in a LIBS spectra. These bulk emissions can often interfere with or hide emissions from secondary metals in the bulk matrix, making the quantification of these lighter elements a challenging and complex analytical problem. As a result, we look towards implementing advanced ML paradigms typically applied towards complex data science problems in order to discern trends in the complex Pu and Pu surrogate spectra.

2.7.1 Artificial Neural Networks (ANNs)

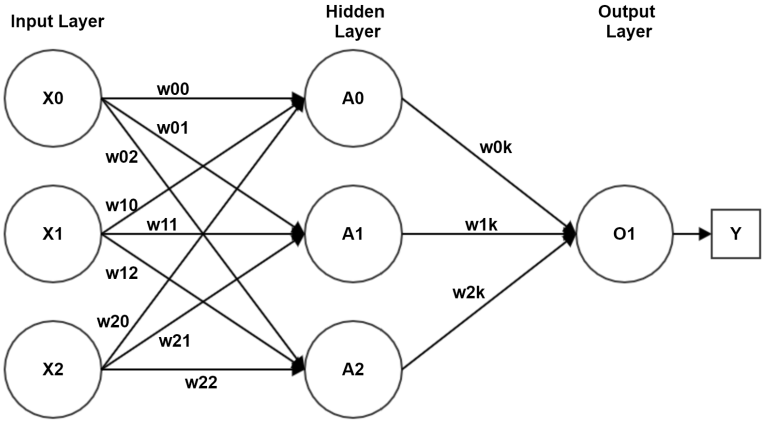

Figure 26. ANN architecture diagram; each circular node represents a single neuron, and each arrow represents the connection of the output of one neuron to the input of another.

ANNs are a machine learning paradigm inspired by the structure of biological nervous systems. Similar to how a neuron receives an input and turns it into a signal to pass to another neuron, a neural network takes a series of input variables and multiplies them by weights. More specifically, data enters an ANN through an input layer and is fed-forward to subsequent layers. Each hidden layer contains neurons (nodes), wherein each neuron sums weighted inputs from the previous layer and generates an output by applying an activation function. The output layer sums weighted inputs from the last hidden layer and generates a numerical output via an activation function. [53, 58] This process is modeled as a mathematical analog of synaptic communication in biological neural pathways; Fig. 26 illustrates a single hidden layer ANN architecture. ANNs have the capability to capture highly complex data relationships and produce accurate classification or regression solutions for very large data sets, and are often used for image or pattern recognition. [59, 60] Their ability to tie a large number of input variables into a concise output makes them ideal for use in spectroscopy, particularly for the plutonium analysis problem.

2.7.2 Tree-based Methods

Decision Trees

Decision trees are commonly used supervised machine learning techniques with applications to a variety of other fields, including data mining, stellar imaging, astrophysics, and molecular modeling [53, 61–64]. Decision trees take input variables and relate them to a target output by following branches across different decision nodes based on the input attribute values, until a terminating node is reached which provides an output result. These algorithms are used in classification and regression, and provide a promising solution to the spectroscopic problem outlined in this study. A graphical depiction of a lone decision tree built from the ceria spectra is shown in Fig. 27, diagramming how the model determines Si content based on the value of different emissions in a spectrum. Whereas a single decision tree model often suffers from overfitting and lower performance with large data sets, an ensemble of trees can improve performance by reducing variance and increasing bias. These types of ensemble methods aim to partition the decision space rather than provide a general separation, making them ideal for use in nonlinear problem spaces.

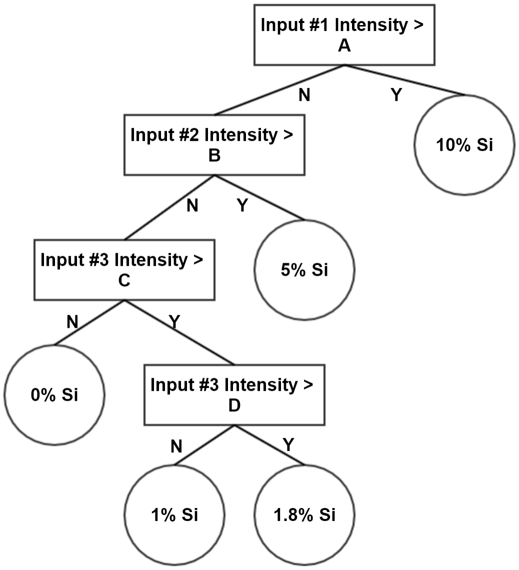

Figure 27. Example of a lone regression tree for Si content prediction. Each rectangle represents a node, or decision based on the intensity value of a particular emission in the spectra, where A,B,C, and D are values determined by the fit model. Each circle represents a leaf, or outcome, determining the Si content from the flow of the nodes and branches.

Ensemble Methods

Two ensemble methods, boostrap-aggregated (also known as bagged) regression trees and boosted ensemble regression trees, can yield the aforementioned enhanced performance over a single regression tree. The methodologies of these ensemble methods are diagrammed in Fig. 28. Bagging uses random replacement sampling to create subsets (S) of the data and independently trains the individual regression models (M), whereas boosting introduces an adaptive algorithm which focuses on areas in the dataset generating higher misclassifications and trains each model sequentially. [53,61] Whereas bagged models run in parallel and the final prediction is made from an aggregate of each trained model, boosting changes the input weights for each model depending on the error of the previous iteration to improve the accuracy of subsequent learners. Using this sequential adaptive process to mitigate misclassification errors generates improved learners that are combined into a final regression model to make the prediction. The adaptive nature of the boosting algorithm reduces errors in prediction due to variance and bias in the data set, yielding models with significantly lower *MSEPs* and better regression fits. Although both ensemble methods improve model generalization and reduce prediction error, the sequential training process of the boosted ensemble method renders it a ”slow learner” compared to the bagged ensemble method, introducing a trade-off between training time and prediction accuracy [65].

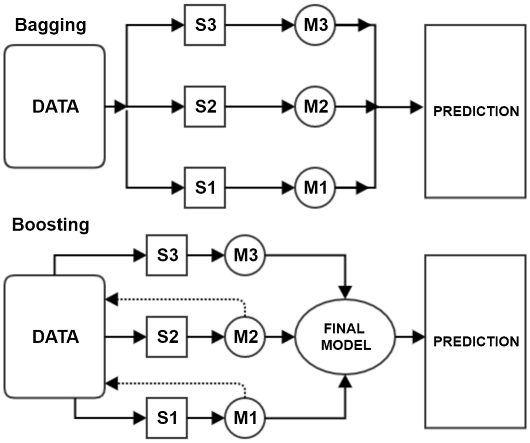

Figure 28. Comparison of bagging and boosting ensemble methods. Squares denoted by ’S’ and ’M’ represent data subsets and individual learner models trained on those subsets, respectively.

Random Forest

Random forest is a variation to the aforementioned ensemble methods. It implements bootstrap aggregation and creates subsets of the original data to train individual learners by sampling with replacement, but the pool of variables for decision splits is limited. Typically, the value $m = p/3$ is given as the allowed number of variables for creating regressions, with p being the total number of predictors in the original data set. This methodology decorrelates the individual trees in the model, improving prediction accuracy by reducing bias and variance.

Extra Trees

Extra trees is similar to random forest, but does not use bagging with random replacement when generating each individual learner. Instead, all the data is used to train each tree. Additionally, while random forest optimizes the decision split points, the extra trees algorithm makes splits at random. This further decorrelates the individual trees in the model, but can increase variance; this can then be countered by increasing the number of individual learners used in the model to make the regression prediction.

2.7.3 Support Vector Machine Regression (SVR)

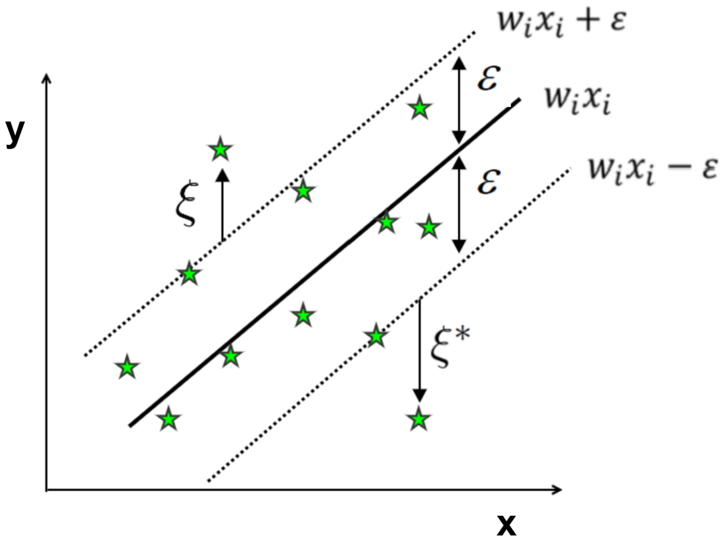

Figure 29. Graphical example of support vector machine regression method depicting support vector regression function $w_i x_i$ with error bounds (ϵ) fitting data points (green stars) with slack error (ξ)

SVR is an extension of the support vector machine (SVM), which uses hyperplanes to divide classes of data points and is well known for its classification abilities. SVR builds on traditional regression methods, such as an ordinary least squares (OLS) regression by allowing the user to define a degree of acceptable error for the prediction range and find the appropriate hyperplane to fit the data. Rather than minimizing squared errors like OLS, SVR imposes a constraint on the error term such that the absolute error is within a margin of maximum error ϵ. This error can be tuned to maximize model accuracy. Based on this error, the SVR minimizes the model weights w as per the function $\frac{1}{2}\ \|w\|^2$ such that the regression function meets the constraint $|y_i - w_i x_i| \leq \epsilon$. This is graphically explained in Fig. 29, derived from Cherkassky 2013 [66]. The green stars represent the input data points, the solid line represents the regression function to the data points x_i with the weights w_i and the dashed lines represent the minimum and maximum error based on ϵ. The variable ξ is a slack parameter which defines a tolerance for data points outside of the regression bounds which the model will deem acceptable for better flexibility.

2.7.4 Kernel Regression

Kernel regression is a nonparametric regression technique in which a mathematical function called the kernel is used to calculate an output by utilizing the weighted sum of all the data points [67]. Estimates are given via a weighted sum, calculated using the Nadaraya-Watson kernel weighted average in Eq. 5. Here, $\mathrm{K}_h(x_s, x_i)$ is a weighting function whose value decreases as the distance between the query point x_s and measurement point x_i increases. Moreover, h is a scaling parameter known as the bandwidth. Lastly, y_i refers to the known outcome value whereas $\hat{y_s}$ is the predicted value.

$$\hat{y_s} = \frac{\sum_{i=1}^{n} K_h(x_s, x_i) y_i}{\sum_{i=1}^{n} K_h(x_s, x_i)} \tag{5}$$

A common choice for the kernel function is the Gaussian kernel, given by Eq. 6, based on the Euclidean norm of x_s and x_i. Implementing this kernel yields the GKR; this technique allows the use of all data points for the prediction of an outcome value, but weights input points closer to the prediction point more heavily [68]. In doing so, GKR can overcome issues seen with similar techniques such as k-nearest neighbors in which the estimate of the response variable can change abruptly despite input features changing continuously when switching the set of nearest neighbors making the prediction.

$$K_h(x_s, x_i) = \exp(-\frac{||x_s - x_i||^2}{h}) \tag{6}$$

III. Experimental Methodology

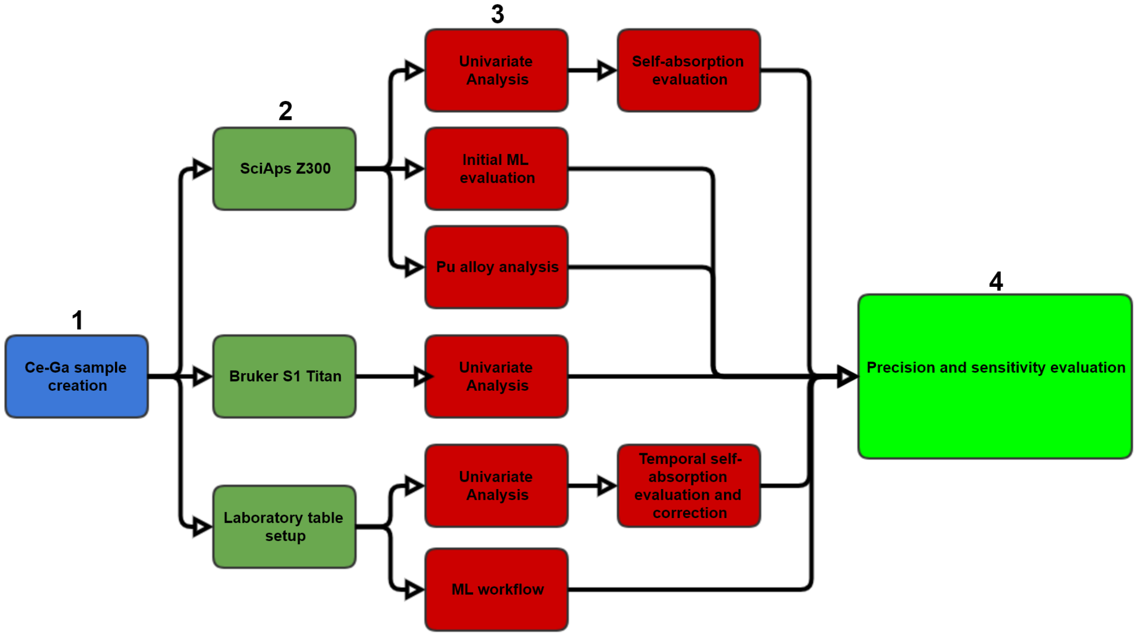

Figure 30. Experimental data collection and analysis flowchart.

This study implemented three separate analytical spectroscopy setups to analyze cerium-gallium samples and a limited set of plutonium alloy samples using various methods for quantititive analysis. Fig. 30 gives a simplified graphical depiction of the workflow of this dissertation research. This overall workflow can be broken down into four main phases; sample creation, analytical tool selection, spectroscopic analysis, and predictive model quantitative evaluation.

3.1 Sample Creation

The first phase of this dissertation research required the creation of Pu surrogate samples for in-house experiments conducted at AFIT. To efficiently accomplish this, oxide-based samples were chosen for analysis in order to simplify the sample creation process and ensure that new samples could be expeditiously created when necessary.

It should be noted that the Master's work preceding this dissertation used Ce-Ga metal alloys; while the physical properties of a metal sample differ significantly from that of an oxide pellet sample, the spectral response remains nearly the same. As a result, no detriment came from switching the sample morphology for the atomic spectroscopy experiments. The cerium-gallium pellet samples were prepared from Sigma Aldrich cerium oxide (99.995% CeO_2) mixed with varying weight percent concentrations of gallium oxide (99% Ga_2O_3). The powders were milled using an agate mortar and pestle, weighed to achieve the desired weight percent concentrations and then homogenized using a Fluxana MUK mixer. The mixed powder was then pressed using a 14 mm stainless steel die at 5 metric tons for 120 seconds. Pellets with 0, 0.25, 0.5, 1, 1.5, 2, 2.5, 3 and 5 wt% Ga were created for use throughout this dissertation work. Each sample weighed approximately 1 gram; the mixing and pressing equipment is shown in Fig. 31.

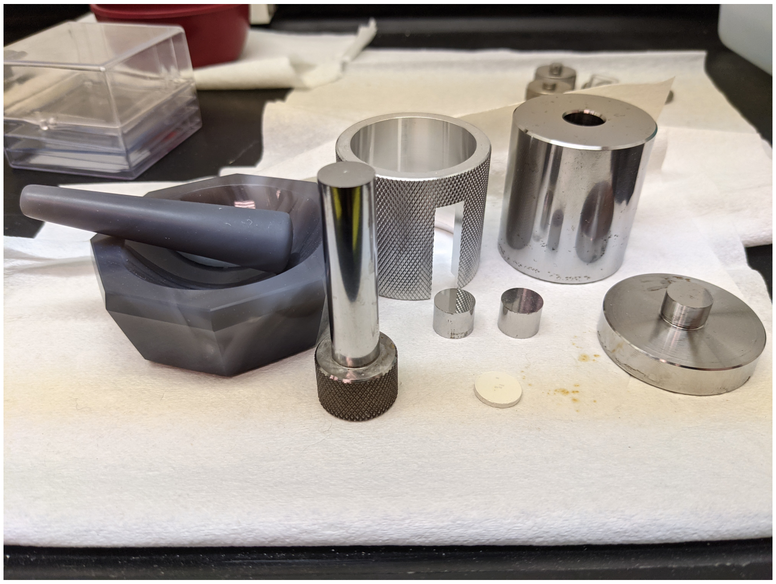

Figure 31. Pellet pressing equipment: 14 mm stainless steel die press set, agate mortar and pestle.

3.2 Spectroscopic Methods

3.2.1 SciAps Z300

The SciAps Z series handheld LIBS analyzers contain all of the hardware shown in Fig. 6 within a compact, lightweight device capable of conducting field/*in-situ* measurements of materials. This study implemented a SciAps Z300, shown in Fig. 32. The device's built-in rastering function and capability to couple to external data acquisition software make it particularly useful for expeditiously analyzing the surface of a sample in a glovebox environment.

Figure 32. SciAps Z300 handheld LIBS device.

Table 2. Z300 specifications

Laser	Nd:YAG
Wavelength	1064 nm
Pulse Width	1 ns
Pulse Energy	5-6 mJ
Focal Length	1.5 cm
Spot Size	50 μm
Dimensions	8.25 x 11.5 x 4.5 in
Weight	4 lbs
Bandwidth	190-950 nm
Resolution	0.1 nm FWHM

3.2.2 Bruker S1 Titan 800

The Bruker S1 Titan Model 800 is a lightweight portable XRF analyzer, marketed for rapid and precise analysis of elements from Mg to U. This device, shown in Fig. 33, uses a 4W Rh target x-ray tube at energies between 6-50 kV to generate x-rays, along with a graphene window SDD detector (20 mm^2 active area) to record fluorescence emissions with a resolution $<$ 145 eV at 450,000 counts per second. The recording time and voltage sweep parameters can be manually adjusted by the user for different material types. The device also comes with a stand and shielded sample chamber for hands-free analysis, and can be run with computer software.

Figure 33. The Bruker S1 Titan Model 800 portable XRF analyzer.

3.2.3 Laboratory LIBS Setup

A full scale laboratory laser ablation setup was implemented for the later phase of this dissertation research to advance studies on the temporal behavior of the cerium LIBS signal and generate large amounts of data to train advanced machine learning models.

Table 3. Regression model error and sensitivity results

Hardware	Model	Parameters
Laser	Quantel Everbright 250	15 Hz rep rate; 10 ns pulse width
Spectrometer	Catalina Scientific EMU-120/65	30x120μm slit width; 25 mm AS;
Camera	Andor USB iStar	1024x1024 pixel CCD
Delay generator	Berkeley Nucleonics 577 DDG	-

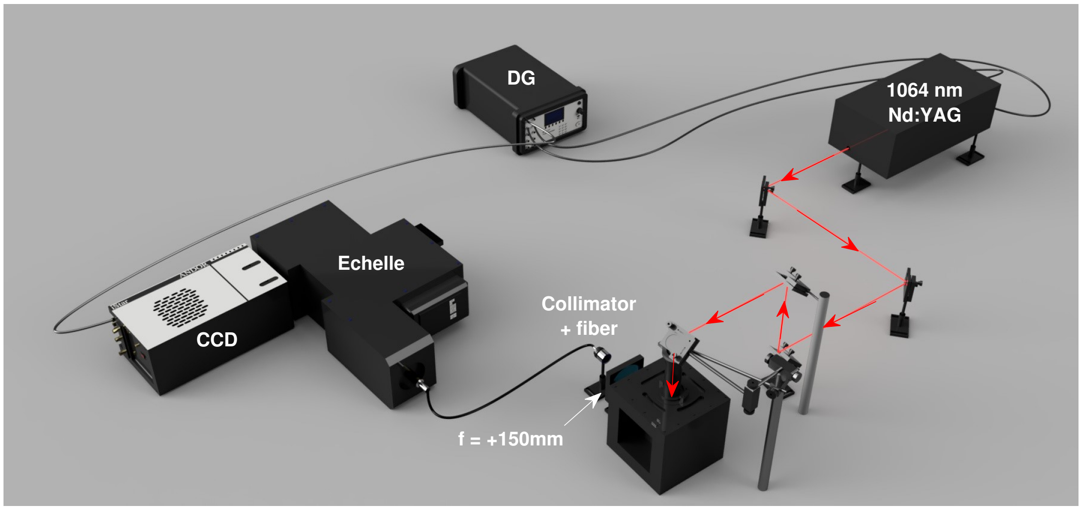

Figure 34. Laboratory LIBS setup with 1064 nm laser, Echelle monochromator and CCD camera.

The main equipment implemented is listed in Table 3. The Everbright laser generated 1064 nm laser pulses at energies between 40 - 250 mJ per pulse. The beam was directed into a sample chamber using a mirror and periscope setup; an f=+30mm lens focused the beam onto the sample to create the ablation. Optical emissions were focused by an f=+150mm lens outside of the chamber and directed into the Thor Labs SMA collimator attached to an optical cable. The cable transmitted the atomic emission light to the Echelle spectrometer, blazed at 505 nm, dispersing the light into a broadband spectrum between 325-925 nm at a resolution of $\Delta\lambda = 0.01$. The Andor CCD camera was used to record the spectral emissions at a variable gate delay, with an exposure time of 1 ms and gate width of 6 μs using an MCP gain of 2000. The DDG was used to trigger all the equipment and set timing parameters; a 190 ns delay between the laser flash lamp and Q-switch was used, and all pulses were set to 10 ns. Both the Q-switch and camera triggered off the flash lamp. The burst mode was used to repeatedly generate ablations with a 3.5s delay between each pulse. This gave the KestrelSpec software on the computer enough time to record and process

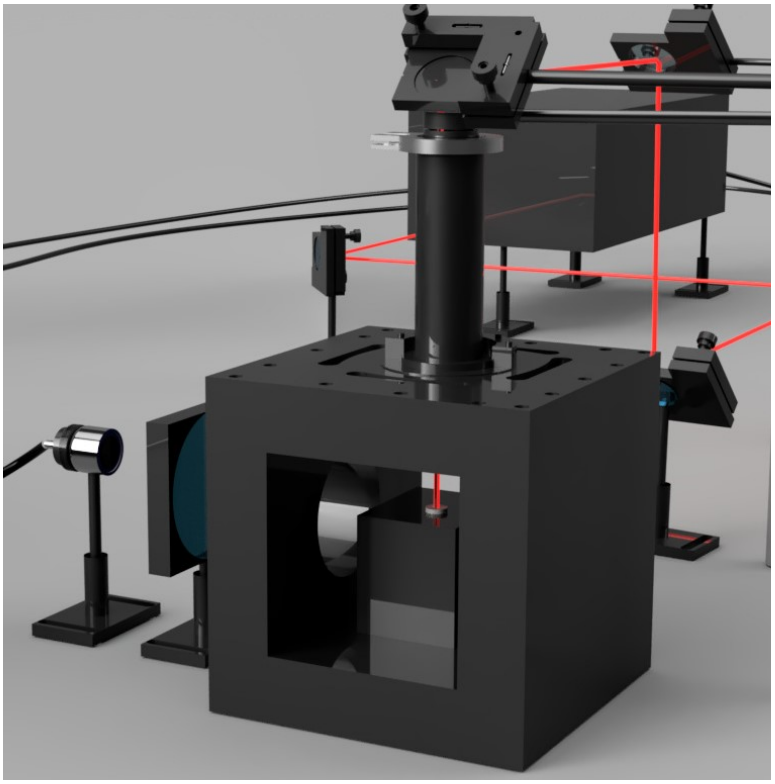

Figure 35. Cutout view of sample in chamber. Laser pulses are focused onto the sample with an f = +30mm lens. Optical emissions are focused with the f=+150mm lens outside the chamber and directed into the fiber collimator.

the spectra of each shot. The full setup is drawn in Fig. 34, with a close-up of the sample chamber shown in Fig. 35. Once recorded on the computer, all spectra were exported as text files and saved for further analysis.

3.3 Analytical Techniques

3.3.1 Univariate analysis

A basic univariate analysis was conducted for nearly every spectral data set in this study. Univariate analysis simply relates the intensity of a single spectra line, or ratios of two lines, to the concentration of the target analyte. These values are plotted at different analyte concentrations and then fit with a linear regression. This is the most basic form of quantitative spectral analysis and was implemented in the previous Master's work for Ce-Ga alloys [18]. The quality of a univariate calibration can be assessed by calculating the limit of detection (LoD) and the error, computed as the mean average percent error ($MAPE$). The LoD is the IUPAC defined quantity representing the smallest amount of minor analyte in the bulk that the calibration model can distinguish from a blank sample to within one standard deviation of error [69]. A commonly implemented equation to determine LoD is shown in Eq. 7. The univariate limit of detection stems from the standard deviation of a blank sample in the bandwidth where the emission used in the calibration exists (σ) and the slope of the calibration curve (b). Lower standard deviations and higher slopes yield lower detection limits, or more sensitive calibration models.

$$LoD = \frac{3\sigma}{b} \tag{7}$$

The formula for univariate calibration error is given by Eq. 8; n is the number of data points, y_i is the datapoint value and $\hat{y}_i$ is the calibration line value. This term quantifies the precision of the regression as the mean error between the calibration curve and calibration data points. A lower $MAPE$ equates to a more accurate model. Together, these two metrics are used to evaluate the quality of a given calibration curve.

$$MAPE = \frac{100}{n} \sum_{i=1}^{n} \left| \frac{y_i - \hat{y}_i}{y_i} \right| \tag{8}$$

3.3.2 Self-absorption correction

A mathematical correction to the self-absorption phenomenon was employed to correct the calibration curves. This was achieved by implementing a well documented intensity correction based on Stark broadening parameters of the selected spectral lines [31, 33, 70]. The correction is formulated as follows: It is well understood that experimentally measured LIBS lines show significant line broadening; this behavior typically stems from two main sources. Doppler broadening occurs in a plasma due to its constituent particles having velocities described by a distribution, rather than a discrete value. Emission particles moving at different speeds produce different Doppler shifts, and the aggregate effect of these various shifts in emissions leads to broadening of the spectral line. Additionally, Stark broadening occurs as a result of electric fields in the plasma splitting degenerate energy levels, which in turn splits spectral lines and also induces broadening. The Stark broadening width, referred to in this paper as the Stark full-width at half maximum (w_s), can be used in conjuction with other calculated plasma parameters to develop a self-absorption correction.

$$\Delta\lambda_0 = \frac{2w_s n_e}{10^{16}} \tag{9}$$

Eq. 9 is a very commonly used relation in LIBS relating the total peak FWHM (λ_0) to the electron density n_e and the Stark width w_s. The electron density in this equation was calculated from a non-absorbed hydrogen Balmer line found in the experimental spectra, rearranging Eq. 9 to solve for n_e. The Stark broadening of the line in the experimental spectra was calculated using a Voigt profile fit (VPF). This fitting method describes a mathematical convolution of a Gaussian and a Lorentzian function, and can be fit using the analytical expression in Eq. 10 where σ and γ refer to the Doppler and Stark broadening widths and w is the Faddeeva complex error function [71]. An example VPF of the Ga I 287 nm peak is illustrated in Fig. 36. This fit can generate the total peak FWHM and the Stark FWHM required for calculating the self-absorption coefficient of the peak.

$$V(\lambda, \sigma, \gamma) = \frac{Re[w(z)]}{\sigma\sqrt{2\pi}}; z = \lambda + i\gamma \tag{10}$$

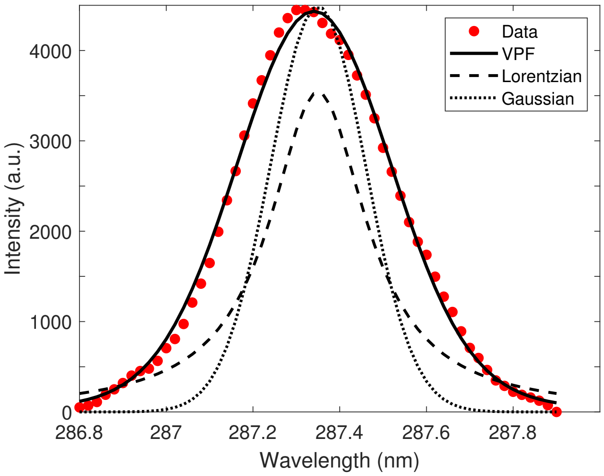

Figure 36. Example deconvolution of the Ga I minor peak using a Voigt profile fitting routine.

The self-absorption correction (SA) is formulated by Eq. 11, noting that the measured full-width at half max (FWHM) $\Delta\lambda$ is related to the actual non self-absorbed broadening ($\Delta\lambda_0$) multiplied by SA raised to the coefficient β which is given as -0.54.

$$\Delta\lambda = \Delta\lambda_0 (SA)^{\beta} \tag{11}$$

Combining Eqs. 9 and 11 to relate the SA coefficient as a ratio of the corrected and uncorrected emission lines yields the empirical expression in Eq. 12 to calculate SA from the electron density and calculated broadening of the emission line used in the calibration curve. The corrected intensity is then calculated as the measured intensity divided by the corresponding SA value at each point.

$$SA = \frac{I(\lambda)}{I_0(\lambda_0)} = \left(\frac{\Delta\lambda}{2w_s} \frac{10^{16}}{n_e} \right)^{\frac{1}{\beta}} \tag{12}$$

Employing this methodology yields a linearized calibration curve corrected for the effects of the optically thick plasma. An appropriate LoD can be calculated from the corrected curve to determine sensitivity, and the *MAPE* can be determined for the corrected calibration and compared to the uncorrected value to gauge improvments in precision by employing this methodology.

3.3.3 Machine Learning Workflow

The novel component of this dissertation research largely rests on the machine learning models discussed in the Theory section being implemented for spectroscopic analysis. After initial cursory results on the efficiacy of ML methods for this type of analysis [72], a machine learning workflow model, illustrated in Fig. 37, was implemented to develop the most robust predictive regressions possible from the spectra acquired in the laboratory. Each step is described below:

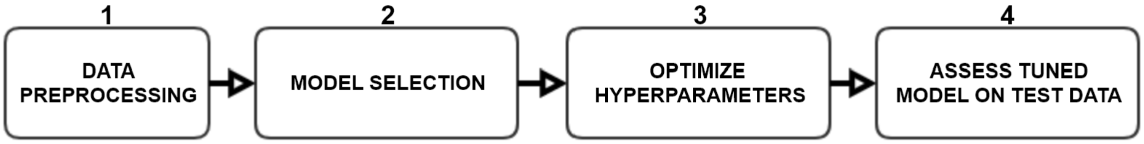

Figure 37. Machine learning workflow process implemented for development of higher fidelity regression models.

1. Data preprocessing: preparing the data for quantitative analysis. This step includes data cleaning (e.g., noise removal and filtering), transformation (e.g., normalization) and reduction (e.g., feature selection and/or extraction) [73].

2. Model selection: selecting ideal candidate ML paradigms to provide a robust solution to the problem at hand. Factors such as training time, complexity, and response to nonlinear data are among things to be considered.

3. Optimize hyperparameters: Hyperparameter optimization is key to tuning the various numerical variables in a given ML model to achieve the best performance (lowest error). This step often involves conducting a design experiment, in which model performance is evaluated for different values of hyperparameters, using

an optimization function to reach tuned values yielding the lowest prediction error.

4. Assess tuned model: The final tuned model delivered from Step 3 is evaluated for performance by passing in test data not used during model optimization or training. This allows for an assessment of the model's accuracy when fielded new data; this step is critical to identifying overfitting, where the model cannot successfully generalize trends in the training data to make accurate test predictions.

3.3.4 Assessment of Models

Each regression model generated with a machine learning method was evaluated for its precision and sensitivity on a test data set. Root mean-squared error of prediction, or *RMSEP*, given by Eq. 13, is used to quantify precision. Here the variables n, y_i, and $\hat{y}_i$ represent the number of samples, the target value, and the predicted value. This metric gives a measurement of the distance between a prediction made by a model and the true target value corresponding to the same input data point and is used to quantify the accuracy of predictive regression models.

$$RMSEP = \sqrt{\frac{\sum_i^n (y_i - \hat{y}_i)^2}{n}} \tag{13}$$

Sensitivity is evaluated using the LoD metric discussed in Sect. 3.3.1 modified for multivariate statistics, shown in Eq. 14 [74].

$$LoD = \frac{3\sigma_a}{b} \tag{14}$$

The multivariate LoD is a simple ratio of the dispersion of the x-intercept of the regression (standard deviation of a) and the slope of the regression (b). Higher slopes from more accurately fit prediction models yield lower LoDs and are therefore more sensitive. The goal of this study is to implement the machine learning workflow to tune regression models to minimize error ($RMSEP$) and maximize sensitivity (minimize LoD).

IV. Analysis of Ce and Pu with portable LIBS device

The SciAps Z300 was implemented for a comprehensive analysis of Ce-Ga and Ce-Si pellets, as well as a shorter analysis of actual plutonium alloy samples. This section describes the results of basic univariate analysis, quantification of self-absorption, and chemometric/machine learning models implemented on the cerium spectra. The extension to plutonium analysis encompassing the same methods is presented as well.

4.1 Ce-Ga pellet univariate analysis

Using the samples previously discussed in Section 3.1, the Z300 was used to collect spectra using an 8x8 raster pattern, averaging every 16 shots in each recording. 5 recordings of each sample concentration were collected, yielding a total data set of 180 recordings, 20 for each Ga concentration. The pLIBS devices was used in gated mode, with an initial gate delay of 250 ns. An argon preflush was implemented to remove air from the vicinity of the ablation. An example of the pure cerium

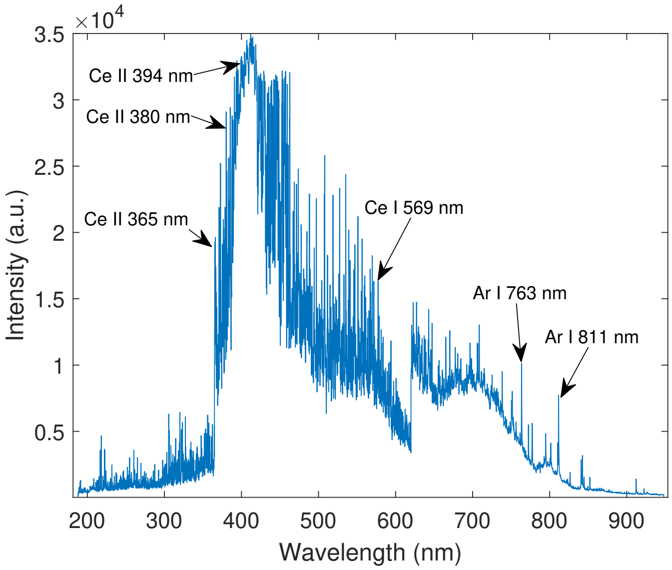

Figure 38. Annotated Ce LIBS spectrum of pure Ce oxide pellet recorded with the Z300.

pellet spectrum recorded with the Z300 is shown in Fig. 38, with the major Ce and Ar emissions annotated. Here it is clear that the limited 0.1 nm resolution of the device causes issues when trying to resolve the major emissions around 400 nm, as the individual emission lines are not discrete and interfere significantly with each other. Additionally, the sheer complexity of the Ce LIBS spectrum is evident in this figure, denoting the difficulty of performing univariate analyses on such data and highlighting the need for machine learning methods.

Analyzing the recordings of the sample set allowed for the extraction of two minor Ga I emissions at 287 and 294 nm. It should be noted that the major Ga I emissions, such as those at 403 and 417 nm, are not well-resolved in the recorded spectra as there is significant spectral interference in the 400-500 nm range in these recordings. Fig. 39 shows the evolution of the Ga I 287 nm emission with increasing Ga content at 250 and 500 ns delay. It is important to note that while the line intensity increases

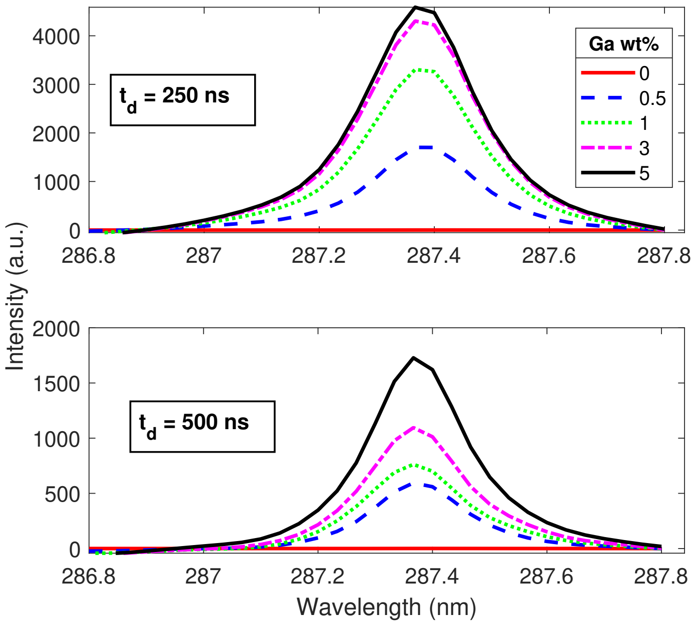

Figure 39. Ga I 287 nm emissions at varying Ga concentrations taken at 250 ns and 500 ns delays.

with Ga content as expected, there is a significant plateau in the intensity increase past 1 wt%; the 3 and 5 wt% data points in fact have almost the same spectral response at 250 ns delay despite the significant difference in Ga content from these samples. This is an initial indication of a phenomenon known as self-absorption, in which a plasma becomes optically thick and reabsorbs certain emission wavelengths, preventing them from exiting the plasma and being recorded on a detector. This is often seen in LIBS studies and is demonstrated to be more pronounced at higher analyte concentrations [2, 70, 75]. Recent studies have recommended recording signal at longer gate delays to mitigate this effect, as it is often most pronounced in the early phases of laser-produced plasmas [76, 77]. The 500 ns delay peak behavior indicates a less pronounced self-absorption effect as there is a greater different between the 3 and 5 wt% peak intensities. This same behavior is evident in the behavior of the 294 nm emission, shown in Fig. 40. The intensity values of the 3 and 5 wt% Ga peaks are noticeably similar when recorded at 250 ns delay, but are more clearly separated at 500 ns delay. However, there does seems to be a decrease in the separation between the lower Ga content peaks at 500 ns, which stems from the overall decrease in recorded signal intensity at 500 ns. This initial evaluation indicates that while prolonging the gate delay of the spectral recording could potentially alleviate self-absorption effects at higher analyte concentrations, the drop in signal later at the plasma lifetime can affect the overall fidelity and sensitivity of the calibration.

The selected LIBS lines from the spectra at each gate delay were used to construct univariate calibration curves relating the peak intensity of each line to the Ga concentration of the sample. First, the self-absorption phenomenon was analyzed by fitting an exponential curve to the data, rather than a linear regression. The method implemented by Yage *et. al.* [75] relating the intensity of the emissions (I) to the analyte concentration (C), a constant (a) and a self-absorption coefficient (b) was

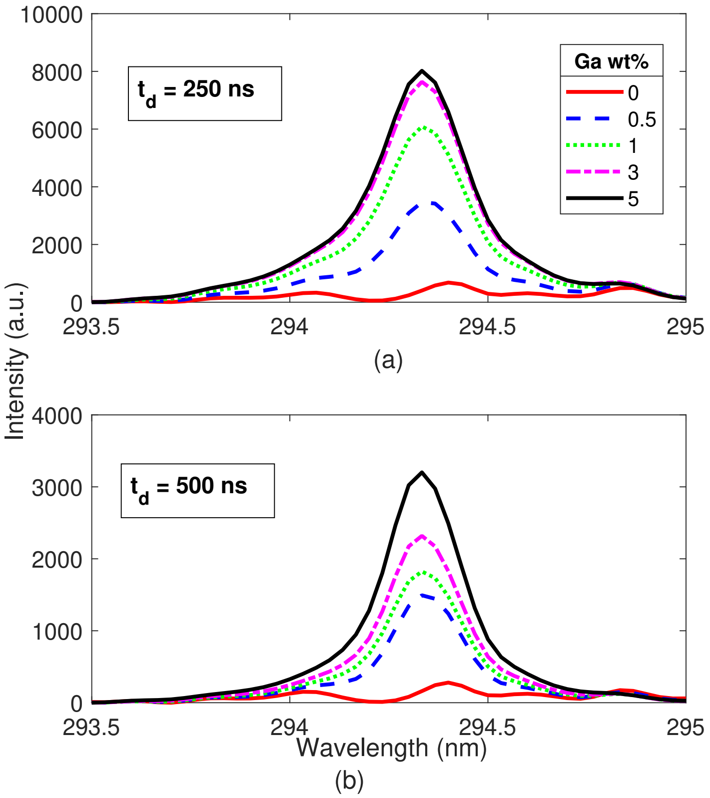

Figure 40. Ga I 294 nm emissions at varying Ga concentrations taken at 250 ns and 500 ns delays.

used to fit the peak intensity data. This relation is given by Eq. 15; $b \approx 1$ signifies perfectly linear behavior between intensity and concentration and the absence of self-absorption.

$$I = aC^b \tag{15}$$

Figs. 41 and 42 illustrate the curve fit applied to the Ga I 287 nm and Ga I 294 nm peak intensities at both gate delays. The power curve fits are accompanied by the expected linear fit to the first few data points before the self-absorption begins to skew the linear trend and bend the calibration curve. Visually, the self-absorption phenomenon is evident at both delay times for each line. However, it appears that the nonlinearity begins to develop at a lower concentration with a 500 ns gate delay.

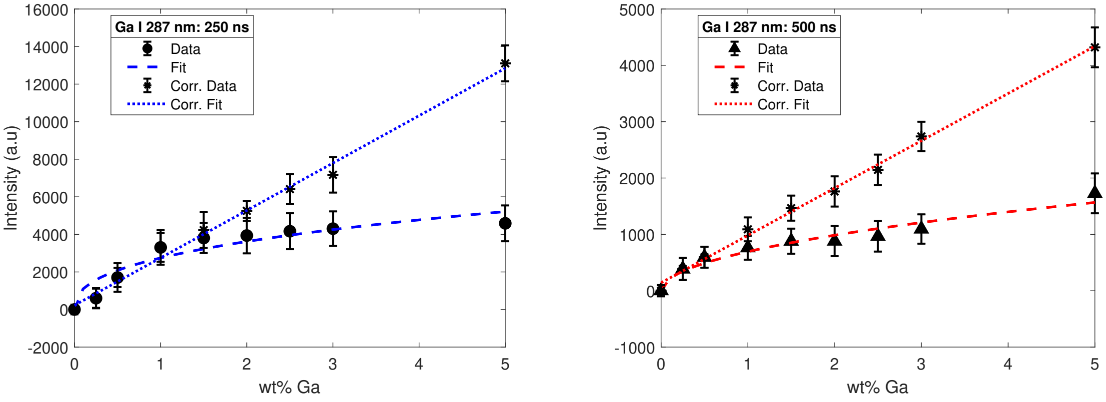

(a) (b)

Figure 41. Calibration curves of the Ga I 287 nm line at a) 250 ns and b) 500 ns gate delay.

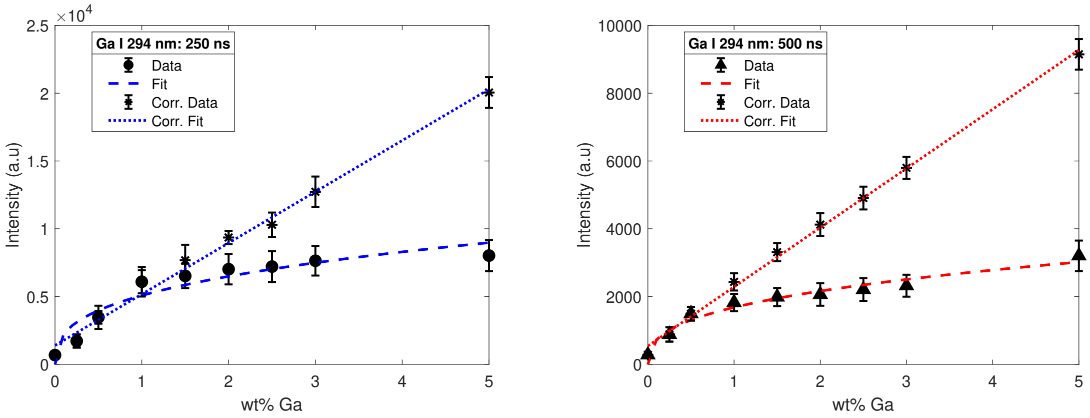

(a) (b)

Figure 42. Calibration curves of the Ga I 294 nm line at a) 250 ns and b) 500 ns gate delay.

The 250 ns delay data remains relatively linear out to 1 wt% Ga, while at 500 ns the curve begins to bend lower around 0.5%, indicating that the level of self-absorption is more sensitive to increases in analyte concentrations at later plasma lifetimes. Table 4 lists the numerical fit coefficients for all four calibration models; the self-absorption coefficient values (b) indicate that increasing the gate delay reduced self-absorption by 20% with the 287 nm line, but only marginally for the 294 nm calibration. This follows the visual trend in the calibration curves showing the persistence of the phenomenon. This indicates the 294 nm line may be more susceptible to the effects of the optically thick plasma, as the bend of these calibration fits is more severely pronounced at 500 ns than it is for the corresponding 287 nm line calibration.

Table 4. Self-absorption calibration fit parameters for all LIBS lines and gate delays.

λ_0	$\mathbf{t}_d$	$\boldsymbol{a}$	$\boldsymbol{b}$
287 nm	250 ns	2746	0.398
	500 ns	693.2	0.507
294 nm	250 ns	5076	0.354
	500 ns	1679	0.364

The SA correction methodology discussed in Sect. 3.3.2 was implemented for each emission line at each gate delay; the original peak intensities were then divided by their corresponding SA values to generate the corrected calibration curves also shown in Figs. 41 and 42 with their uncorrected counterparts. Next, the precision of the corrected and uncorrected calibrations were evaluated by calculating the ($MAPE$). This quantity estimates an average error bound for the whole calibration curve from 0 to 5 wt%. Additionally, the sensitivity of each corrected calibration was determined by calculating the 3-sigma LoD as defined by Eq. 7, using the slope of the fit and the blank standard deviation. These fit quality metrics are listed in Table 5. The data clearly indicates an accuracy improvement in the models when the gate delay is extended to 500 ns, as even the uncorrected calibration curves saw significant error reductions at the later time. Applying the SA correction drastically improved model precision; errors as low as 3 and 4 % were achieved in conjunction with the later gate delay using the 287 and 294 nm peaks, respectively. These results clearly demonstrate the merits of the applied correction methodology for improving the efficacy of univariate calibration models. The sensitivities of each corrected model do not differ significantly when the delay is lengthened by 250 ns; in fact, for the 287 nm line the LoD actually increases 0.1% when the delay is extended. A potential cause for this could stem from the overall reduction in line intensity when the spectrum is captured later in the plasma lifetime. A calibration with lower intensity value data points will likely have a lower slope, which directly increases the LoD. It should be noted that the 294 nm line calibrations were significantly more sensitive than those of the 287 nm line post-correction. This peak seemingly benefited more from the applied correction when compared to the 287 nm calibrations, and yields detection limits around a tenth of a percent, which is acceptable for the problem at hand since homogoenous δ-Pu forms with 0.5 to 2.5 wt% Ga alloyed. It should also be noted that the Z300 has a small gate delay range with a max of 650 ns, while many LIBS measurements are taken well beyond in the 1-2 μs range. One would expect to see more significant differences in calibration fit when the gate delay is increased past 500 ns as the dynamics of the plasma change significantly in the μs range of its lifetime. This is investigated with a laboratory LIBS setup in Sect. 6.1.

Table 5. LIBS univariate calibration fit metrics: *MAPE*, and LoD for each emission line and gate delay.

λ_0	$\mathbf{t}_d$	**Uncorr. MAPE**	***Corr. MAPE***	**LoD**
287 nm	250 ns	38.4%	10.0%	0.60%
	500 ns	20.8%	4.4%	0.70%
294 nm	250 ns	27.4%	8.4%	0.14%
	500 ns	18.0%	3.4%	0.11%

Overall, the LIBS calibration results indicate some important trade offs to consider when choosing a gate delay for spectral acquisition with the Z300. While changing the limited gate delay of the devices does not completely mitigate SA effects, it can yield calibration models with higher precision for gallium quantification. However, the sensitivity is not greatly affected and may even be detrimented in some cases due to the overall decrease in recorded spectral intensity at longer gate delays.

4.2 Ce-Si pellet machine learning analysis

A study on cerium-silicon pellets was conducted as an initial exploratory venture into various machine learning regression methods. This portion of the dissertation research serves as a proof of concept study of the efficacy of machine learning constructs for spectroscopic problems. As such, the full ML workflow was not implemented, rather a cursory selection of models were trained and tested to begin the investigation into applying machine learning paradigms. Cerium and silicon oxide powders were used to form pellets of 0, 1, 5 and 10 wt% Si. Using an 8x8 raster pattern, argon purge, and gate delay of 250 ns, the Z300 was used to record 176 spectra across the range of sample concentrations. The raw spectra were normalized using the standard normal variate (SNV) method in Eq. 16; each spectrum (I_k) is centered on its mean value (μ_I) and then divided by the original spectrum standard deviation to yield the SNV normalized spectrum (I_k^{snv}). Normalization is commonly implemented in spectroscopic analysis to reduce signal fluctuation in the raw spectra and yield enhanced analytical performance; [78] SNV normalization is often implemented in pre-processing LIBS, near-infrared and Raman spectra for this purpose. [79–82]

$$I_k^{snv} = \frac{I_k - \mu_I}{\sigma_I}, \quad \forall k \tag{16}$$

Normalization was important for this application as the entire spectrum rather than a particular wavelength range was used to train and test the different regression methods. More specifically, SNV was implemented to allow the machine learning models to more easily discriminate the small differences in spectral response among the different sample concentrations. It should be noted that cutting the spectra down and using less wavelength variables could be advantageous, especially since a lot of lighter metals emit at lower wavelengths (200-400 nm), while the higher wavelengths (700+ nm) in the recorded spectra contain mostly emissions from the argon purge gas. However, this initial study sought to test the efficiency of different regression methods with a very complex data set, so all wavelength variables were kept for training and testing.

4.2.1 PCA and PLS

PCA and PLS were implemented for initial trend analysis and regression, as these are the most commonly used chemometric techniques for complex LIBS data sets. PCA was used to perform an initial analysis of the data to visualize similarities and differences between the samples. Examining a plot of the first three principal component scores which collectively explain greater than 90% of the total spectral variance, displayed in Fig. 43, shows some initial separation between the different sample concentrations. Although a clustering pattern is noticeable, the first three wt% groups show significant overlap. To understand how this could affect a regression model created from the transformed variables, we examine the explained variance of each PC. Typically, PCA is used to reduce the original variable set down to a few principal components representing most of the variance of the original data. The first PC of this deconstruction explains 73% of the total spectral variance. However, examining the first PC loading values of each emission wavelength yields some insight

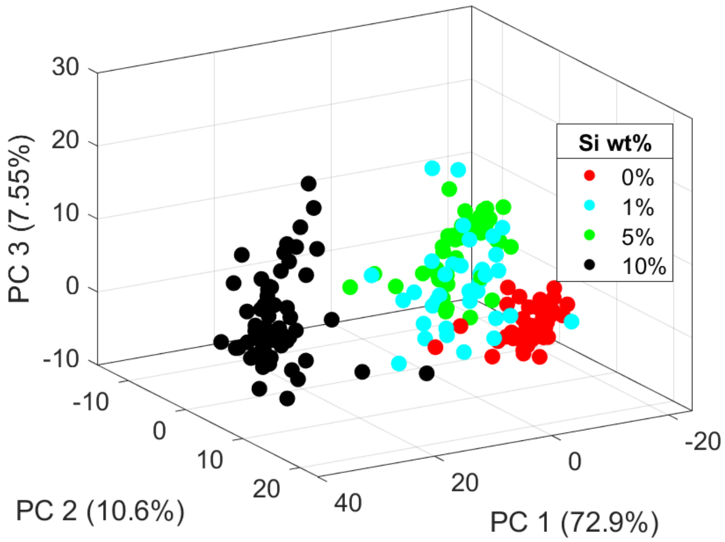

Figure 43. 3D plot of the PC score value of the first three components of each sample. The percent variance of the total data explained in each component is listed on the axis of each PC. The scores plotting reveals overlapping groups of the samples by their Si wt%.

into why the cluster separation is imperfect.

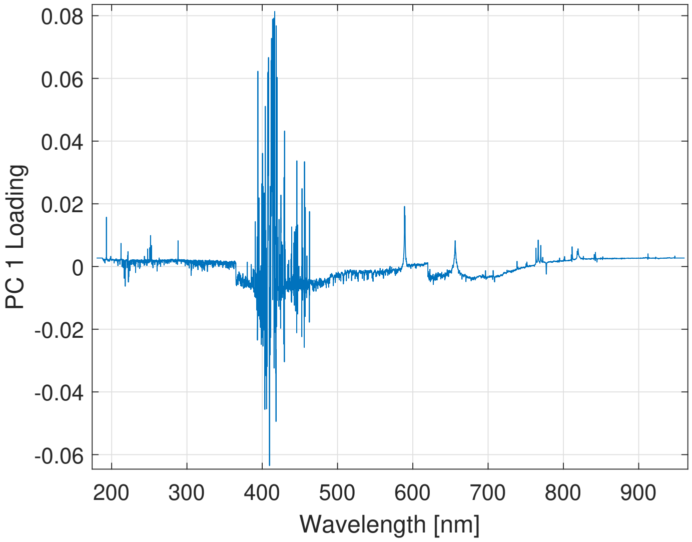

Figure 44. Wavelength loadings in PC 1. A higher loading value indicates that emission wavelength contributes more to variance of the spectral data set.

The majority of the wavelengths in the first PC with the highest loading values correspond to emissions from the bulk cerium oxide, as seen in Fig. 44. Silicon emissions, often strongest below 400 nm, [32] load relatively low on this PC despite it explaining the overwhelming majority of the total variance of the entire spectral data set. This indicates that the intensity of the silicon emission lines varies significantly less between the different sample concentrations when compared to the cerium emissions. Data corresponding to smaller emissions from the dopants is typically pushed to lower PCs, while higher PCs explain variance of the bulk emissions. As a result of this, a good visual separation between sample types cannot be achieved by simply plotting the scores.

This result has significant implications for regressions built from the transformed PC variables. In order to ensure that a regression model can properly distinguish the variations in spectral features between different dopant concentrations, a higher number of components needs to be used in the model. PCs explaining very little of the total variance can often contain important information corresponding to variation in emissions from dopant or impurity elements, and need to be included for accurate determination of elemental concentrations. Ten-component PC regression (PCR) and PLS regression (PLSR) models were built with this data set; the models are compared graphically in Fig. 45, and their R-squared (R^2), ($RMSE$), and LoD values are listed in Table 6. The higher R^2 value of the PLSR model indicates a superior regression fit to the transformed data, whereas the lower $RMSEP$ and LoD values indicate higher predictive accuracy and sensitivity for Si prediction. As expected, these results indicate that PLSR provides the better regression model.

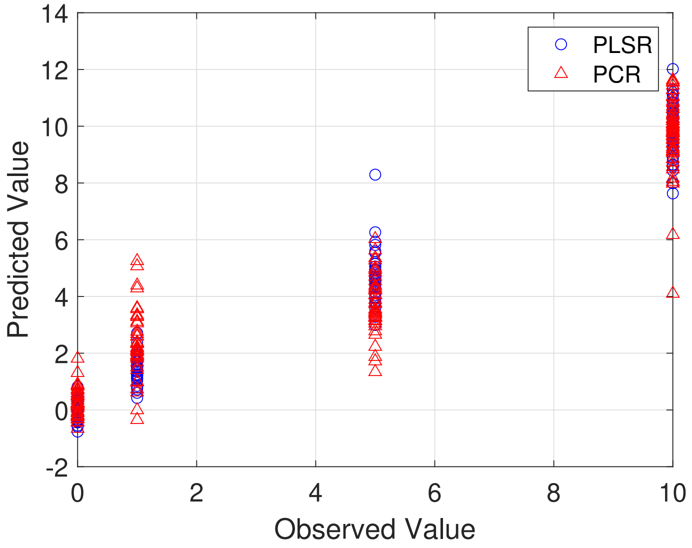

Figure 45. 10-component regression models built with PCA and PLS, comparing the Si content of a sample predicted by the model to the actual value.

Table 6. Comparison of R^2, RMSE and LoD values for regression models

Model	R^2	$RMSE$	LoD
PCR	0.887	1.388%	1.67%
PLSR	0.967	0.749%	1.15%

4.2.2 Ensemble Regression Methods

Two tree-based ensemble methods discussed in Section 2.7.2 were implemented to generate regressions predicting Si concentration from spectral inputs. Bagged and boosted ensemble regressions were trained on the spectra using a 70/30% training and testing split on the normalized data. The default leaf size of 5 was used for both methods, along with 100 learners in each model. Fig. 46 displays the test regression results.

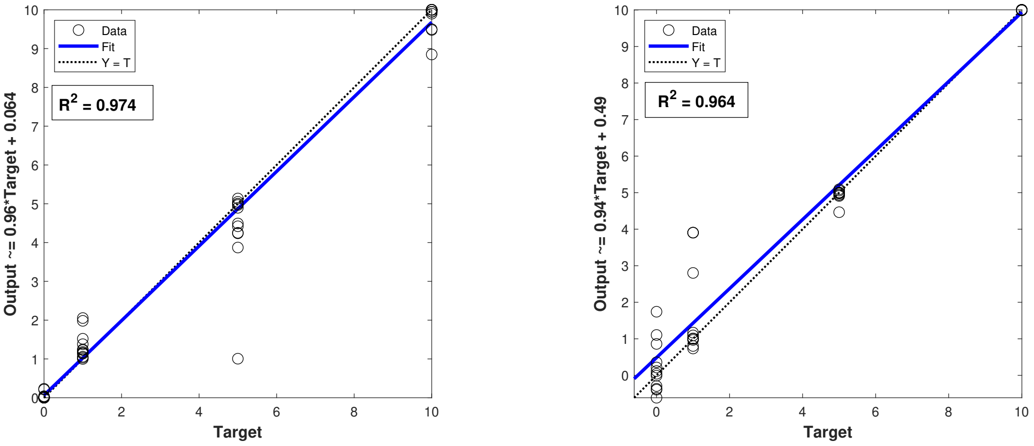

(a)

(b)

Figure 46. Ensemble test regression results using a) bagged and b) boosted methods.

Both ensemble regressions exhibited similar linearity in their first to the test data, with the bagged ensemble being slightly better with $R^2 = 0.974$. The *RMSEP* and LoD metrics defined in Section 3.3.4 were calculated in order to compare precision and sensitivity between the two ensemble methods. The boosted ensemble yielded higher overall precision with a *RMSEP* of 0.272% compared to the bagged model at 0.675 %. This is indicative of the iterative boosting algorithm decreasing error of the subsequent individual learners in the model during the training process. The LoD calculations revealed that the bagged model was nearly an order of magnitude more sensitive than the boosted model, as both fits yielded LoDs of 0.279% and 2.05%, respectively. Initially it seems counterintuitive that the more precise model would be significantly less sensitive. However, examining the blank test predictions (0%) data of Fig. 46b reveals significant dispersion of these points; higher dispersion of the intercept increases the value of σ_a, thereby rendering the model less sensitive to lower concentrations of analyte and increasing the limit of detection. It is unclear what prevents the boosted model from generalizing a blank sample while the bagged model is able to do so much more efficiently. However, both ensemble methods show promise for solving similar analytical spectroscopy problems with further model tuning and optimization as they clearly outperform traditional chemometric methods such as PCR and PLSR with regards to precision. The bagged ensemble also yields an order of magnitude lower LoD than PCR and PLSR, indicating superior sensitivity compared to these methods.

4.2.3 Feedforward neural network (FFNN) Regression

The FFNN is a simple type of ANN architecture employing a single layer of neurons and no feedback loops. An FFNN regression model was constructed, with a layer size of 15 neurons, and a 70/15/15% training/validation/test partition was applied to the data set. A scaled conjugate gradient training function was implemented for optimization; the network was run over 42 full learning cycles, or epochs, and its performance is graphically evaluated in Fig. 47. The FFNN produced a model with the lowest validation MSE of 0.412, initially indicating high predictive accuracy. Upon closer inspection, however, it appears that this ANN structure suffers from overfitting of the data. In Fig. 47, the training (blue) and validation (green) curves are driven to low *MSEs*, but the test performance curve (red) has a minimum error almost an order of magnitude higher (1.123) than that of the lowest *MSE* of the validation curve. This indicates that while the model was able to accurately fit the training data and lower

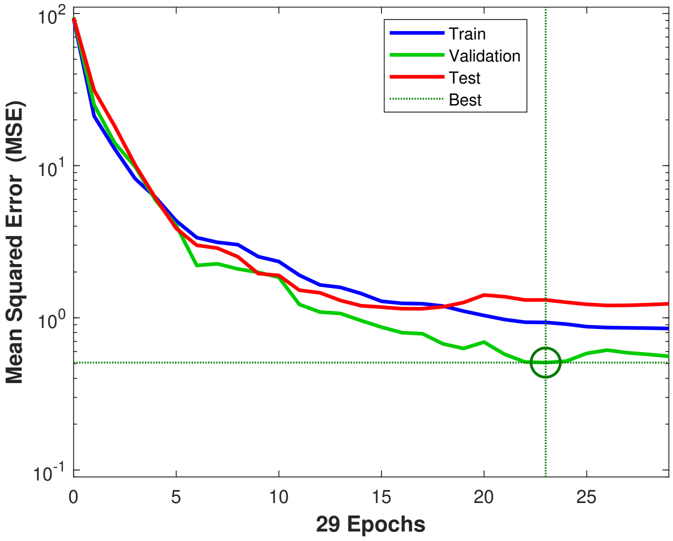

Figure 47. ANN regression model performance curve tracking *MSE* over each training cycle for all 3 data splits.

prediction error by updating weights during validation, it failed to generalize these results to the test set. As a result, the FFNN could not provide accurate predictions of Si content for new data. The model can be further analyzed by evaluating the fits of the regressions between the targets and outputs in Fig. 48.

Overall, the FFNN provided good regression fits to the training (Fig. 48a) and validation (Fig. 48b) data, but yielded a poorer fit to the test set (R^2=0.936) in Fig. 48c. This yet again indicates overfitting and a failure to properly generalize the model to new data. The model yielded a total R^2 value of 0.975 (Fig. 48d), comparable to the PLSR and ensemble regressions. Although ANNs have traditionally provided accurate regression and classification models for spectroscopic problems, this study presents evidence that ensemble regression methods can be used in-lieu of traditional neural network architectures for rapid and accurate quantification of trace elements in a bulk cerium matrix. These results are summarized in Table 7, with the best regression performance parameters in boldface. While the bagged ensemble provided the best regression fit (R^2 = 0.974) and highest sensitivity (LoD = 0.279%), the

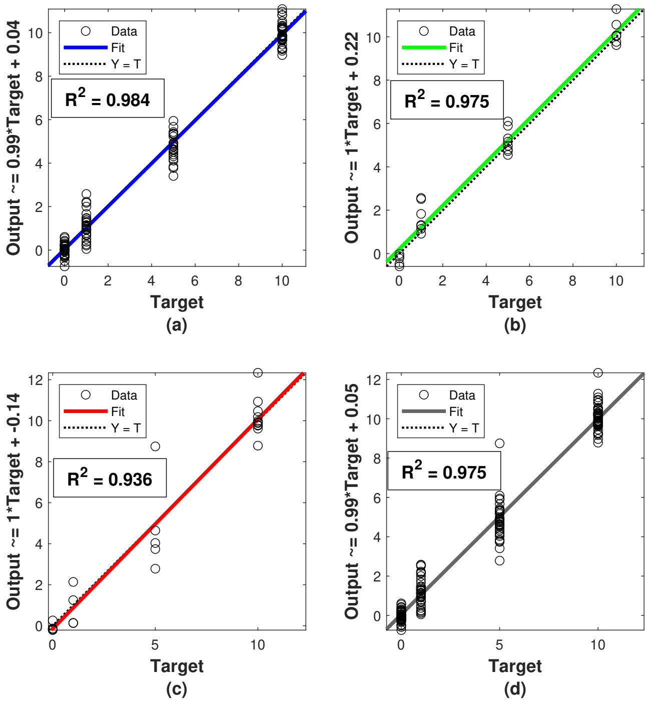

(a)
(b)
(c)
(d)

Figure 48. Feedforward network (a) training, (b) validation, (c) test and (d) total regression fits on Ce-Si spectral data.

boosted ensemble yielded the highest precision predictive model ($RMSEP = 0.272\%$). These results indicate that ensemble methods can provide advantages in accuracy and sensitivity while avoiding overfitting when compared to more common analytical approaches, and present themselves as a promising new tool for use in analytical spectroscopy.

Table 7. Summary of regression model performance parameters

Model	R^2	***RMSEP***	***LoD***
PCR	0.8871	1.388%	1.669 %
PLSR	0.967	0.749%	1.155%
Bagged Trees	**0.974**	0.675%	**0.279**%
Boosted Trees	0.964	**0.272**%	2.05%
ANN	0.936	1.059%	1.086%

4.3 Analysis of Plutonium Alloys

A study on plutonium alloy samples was conducted at Los Alamos National Laboratory, using the Z300 to record spectra from 4 different Pu samples with known concentrations of different trace elements. The Pu samples used in this study were metal coupons approximately 30 mm in diameter; a notional depiction is presented in Fig. 49. These samples had varying concentrations of the two trace elements analyzed in this study. The sample compositions are listed in Table 8. Due to radioactivity and pyrophoricity of plutonium metal, our work had limited access to only a few different Pu samples for spectroscopic introspection. However, a large amount of spectra were recorded from each sample to ensure sufficient data for constructing chemometric models. The first sample, labeled S0, was a plutonium Certified Reference Material (CRM) at 99.96% purity. The other samples were fabricated alloys with different levels of various trace elements present. The concentrations of several trace elements in these samples were verified by ICP methods at LANL, and we were provided the concentrations of Fe and Ni for this study. Additionally, samples 3 and 4 have the same reported concentrations for both metals as these two sample pieces originated from the same larger component. They were removed to initially analyze

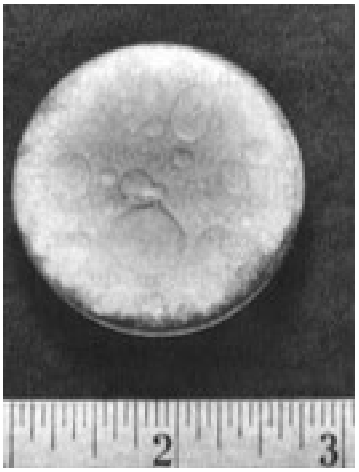

Figure 49. Notional image of size of Pu coupon samples used in this study.

alloy homogeneity.

Table 8. Trace element concentrations of each type of sample used in Pu spectral data acquisition.

	Trace element content (ppm)	
Sample type	**Fe**	**Ni**
S0	0	0
S1	634	1305
S2	743	561
S3	246	105
S4	246	105

Spectral acquisition was conducted through the SciAps Profile Builder software, enabling laser triggering and data acquisition settings changes from the computer, while the device remained in glovebox. The device was used in gated collection mode, with a gate delay of 250 ns and an integration period of 1 ms. An 8x8 raster pattern was implemented, recording 8 spectra at 8 locations on the sample each time the laser was triggered and averaging every 8 spectra, yielding a final total of 8 spectra per individual recording. An example Pu spectra recorded by the device is illustrated in Fig. 50, with the major Pu and Ar emission peaks labeled. Between 2-6 locations

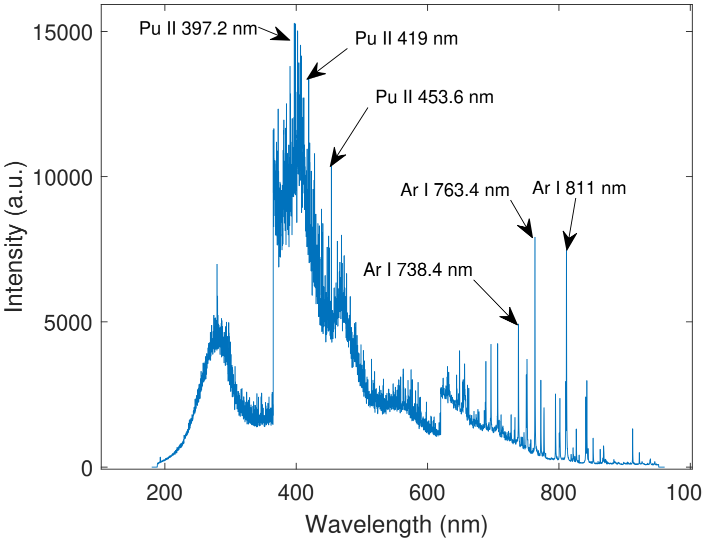

Figure 50. Pu CRM spectrum recorded by the Z300.

on each sample were tested, generating a total of 145 spectra collected across the whole sample set after a few individual spectra were thrown out due to recording errors by the computer software. It should be noted that while the device is triggered from an external laptop, it is held to the sample by a glovebox operator. Small hand movements during the laser firing and signal recording process can yield jitter and shot-to-shot deviations in the spectra that are greater than a typical laboratory LIBS experiment. This was partially mitigated by operator training, and our work yielded shot-to-shot intensity fluctuations of 30% which is within the typical range for LIBS experiments; this was adjusted for during pre-processing using the standard normal variate (SNV) method for spectral normalization as defined by Eq. 16.

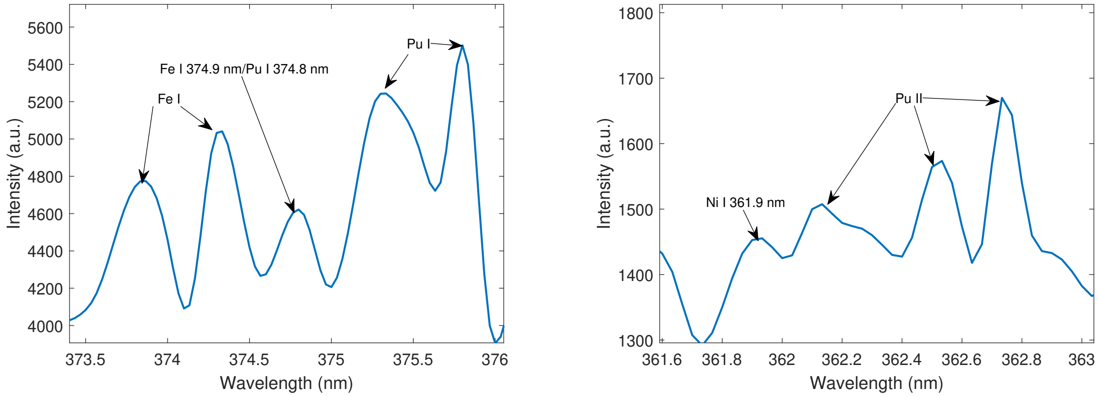

(a) **(b)**

Figure 51. Peaks of a) Fe and b) Ni shown in the Pu spectra with surrounding interference emissions.

Chemometric routines were developed to utilize the entire UV-VIS spectra to identify changes in analyte concentration and compared to a univariate technique based on a singular peak height. The overarching goal of implementing chemometrics in this work was to generate a robust prediction model that can relate holistic changes across the breadth of the UV-VIS spectra that are related to changes in analyte concentration. Chemometric methods are imperative when analyzing a complex metal like plutonium due to the large amount of spectral intereferences that can occur with other trace analytes in the sample. This is illustrated in Fig. 51, which demonstrates the close proximity or direct interference of common Fe and Ni emissions with nearby Pu emission lines. These large interferences between emissions of the bulk and trace analyte material throughout the spectra make traditional univariate calibration methods difficult to implement for development of accurate regression models. The complexity of the spectra of actinide metals therefore highlights the need for more advanced techniques which can adequately detect peaks of trace metals like Ni and Fe and discern the relationship between small changes in spectral intensity and the trace analyte concentration.

4.4 Univariate calibrations

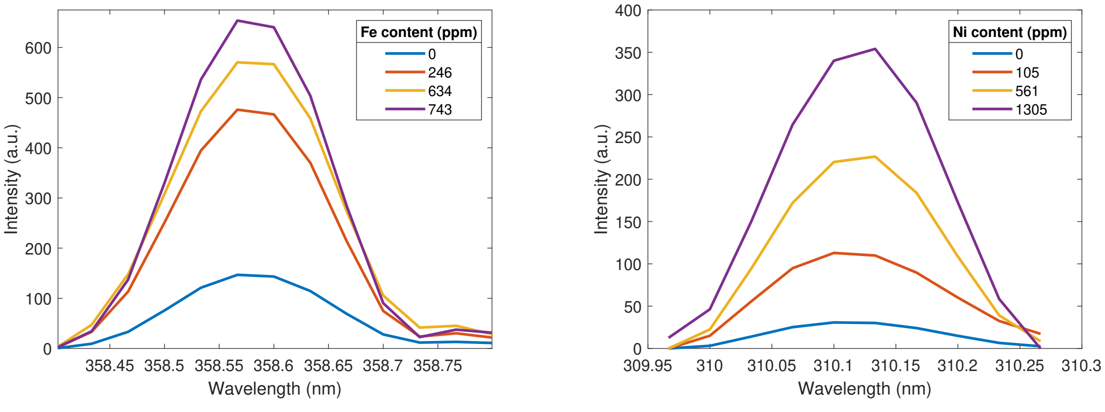

(a) **(b)**

Figure 52. Emissions of a) Fe and b) Ni in the Pu spectra chosen for univariate analysis.

The Fe I 358 nm and Ni I 310 nm lines were selected as the basis of univariate calibrations as shown in Fig. 52 because they were the strongest lines available that were also interference free. Nonetheless they are still minor peaks as all major peaks for iron and nickel suffered from interferences with Pu emissions. The selected emission line peak intensities for the four different concentrations of each element were extracted from the data, along with uncertainties propagated from standard deviation of the peak intensities between each shot. The custom MATLAB function *linfitxy()* was implemented to produce a linear regression which factored in the uncertainty of each data point, determined from the standard deviation of peak intensity between shots and statistical error propagation rules. The resulting linear regressions for Fe and Ni, along with R^2 values for each fit, are displayed in Fig. 53.

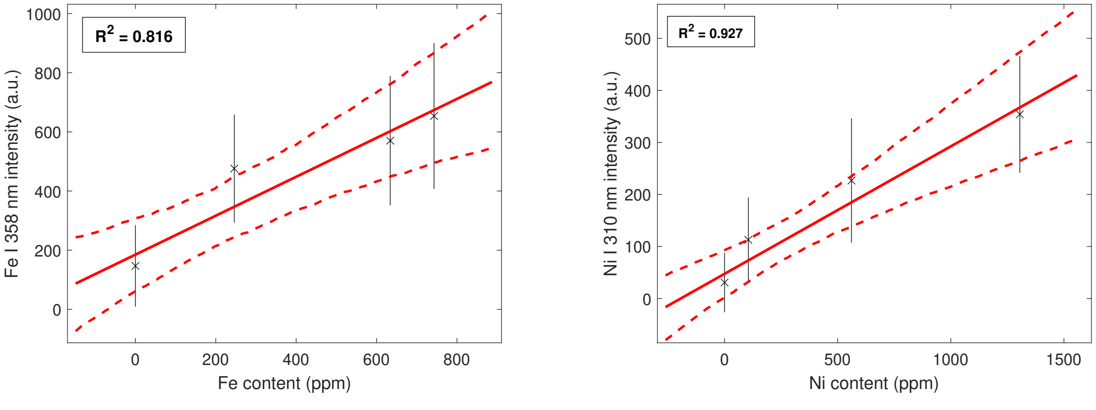

(a) **(b)**

Figure 53. Regression fits of a) Fe and b) Ni peak intensities over the range of sample concentrations.

The linear regressions to peak intensity were used to calculate a univariate LoD and MAPE for each regression model in order to evaluate the regression sensitivity and precision, respectively. The fitting parameters and sensitivity/precision metrics for each model are listed in Table 9. The fit to the Ni peak yielded a better R^2 value than the Fe regression, but was marked by a poorer LoD. This is directly attributable to the lower slope of the Ni regression. The univariate LoD is directly dependent on the sensitivity of the measurements, quantified by the slope of the regression. A lower regression fit slope then correlates to a higher LoD and overall less sensitive model. It should also be noted that the univariate calibration LoDs are in the high hundreds of ppms; these quantities are unacceptable for accurately conducting a trace metal analysis in Pu. One potential underlying cause of the low sensitivities of these models is the self-absorption phenomenon discussed earlier [83].

Additionally, a previous study by Zhang *et al.* notes the fragility of implementing univariate methods for creating calibration curves due to susceptibility to fluctuations in laser energy and matrix effects in the sample [84]. Sometimes these effects can be mitigated by normalizing the spectral internally to a particular strong emission line, however internal standard normalization often becomes less effective when analyzing a complex metal like plutonium with hundreds of convolved major emissions. This sheds some light as to the reasons for the high LoDs from these calibrations. Both regressions had *RMSE* values of the same order, with Ni markedly lower around 38. Ideally for a more accurate model, these *RMSE* values should be orders of magnitude lower than the range of target values for the regression. The clear underperformance of these simple univariate models stresses the need to implement chemometrics to generate more robust models which yield lower LoDs and prediction error values for better trace element quantification.

Table 9. Regression fitting parameters from the Fe and Ni univariate calibration models for the line y = ax + b.

Element	a	δa	b	δb	R^2	LoD (ppm)	*MAPE*
Fe	0.658	0.324	184.9	123.6	0.816	640	15.4%
Ni	0.245	0.091	47.47	45.32	0.927	700	27.9%

4.5 Chemometric regression results

The PCA algorithm was used to decompose the entire 145x23141 spectral emission data set into loadings and scores; the variance explained by the first 10 principal components is depicted in Fig. 54. The first three PCs explain over 95 percent of the variance of the data, a more than sufficient quantity needed to generate a regression. The first three PCs were kept and used to create a regression relating the transformed PC scores of components 1 through 3 to the mean centered concentrations of Fe and Ni in all the samples. Fig. 55 depicts the generated predictive regression for each

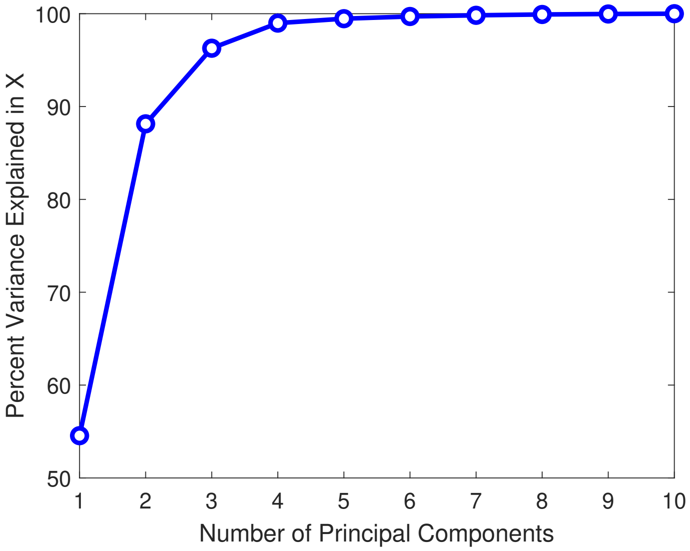

Figure 54. Percentage of variance of the total data set explained by cumulative PCs. The more PCs used in the regression, the larger the percentage of the original variance explained by the model.

trace element, with the accompanying R^2 value for each fit.

The PCR method provided a poor fit to the Fe target data, and performed slightly better for the fit to the Ni target data. Analyzing the predictive accuracy of each model can be conducted by calculating the LoD and RMSE of each regression. Table 10 lists the regression fit parameters, R^2, and calculated LoDs and $RMSE$s for each element. Although the LoD for Ni was comparable to the lower bound of the range of this trace metals in the samples, the result for Fe is markedly poorer at 340 ppm. This is directly caused by the poor PCR fit to the Fe target data, indicating that PCR may not be able to perform well enough to reliably analyze trace iron content in plutonium metal. One explanation for this disparity in achieved LoD could be that emissions from Fe interfere more with the Pu emissions in the spectra than Ni emissions do. Higher elemental and spectral interference may inhibit the PCA algorithm's ability to distinguish between the elements and provide a robust regression model. Overall, both PCR models displayed poor predictive accuracy as noted by their high $RMSE$ values. These values are an order of magnitude higher than the corresponding

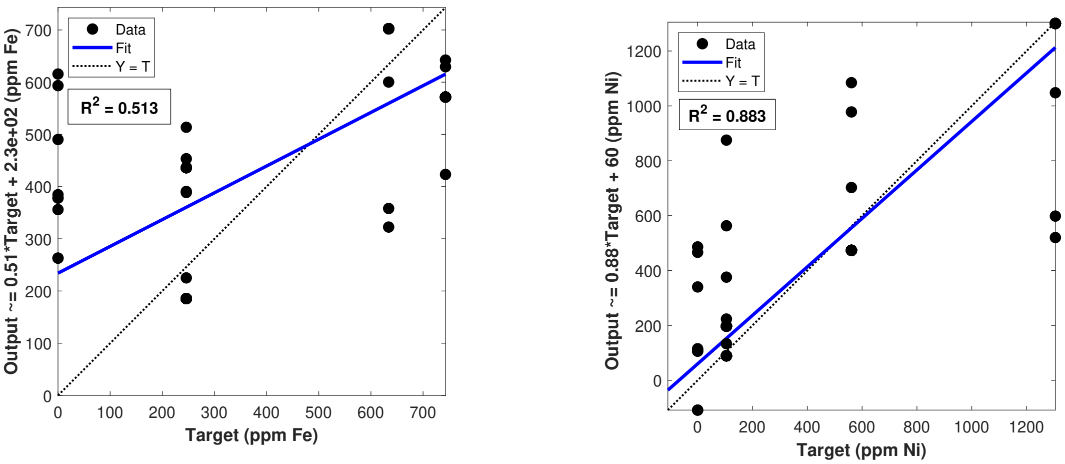

(a) **(b)**

Figure 55. PCR fits of a) Fe and b) Ni data. The fit (blue) to the data (black points) denotes how well the model output prediction of elemental concentration compared to the known target concentration.

univariate *RMSE*s. This trend is directly attributable to the unsupervised nature of the PCA technique; without target data to fit to the trends in spectral intensity variations, the predictive capability of the model is significantly diminished. These results conclude that PCA is not the ideal solution for analysis of complex spectral data, and a supervised chemometric technique such as PLS is necessary.

Table 10. Regression fit parameters, R^2, LoD and RMSE for PCR models.

Element	a	b	R^2	LoD (ppm)	$RMSE$ (ppm)
Fe	230	0.51	0.513	340	176
Ni	60	0.88	0.883	125	160

A PLS decomposition was performed on the complete spectral data set; a regression was constructed using the first 3 latent variables, which account for more than 95% of the original variance, to keep consistency with the PCR model. The regression fits and accompanying R^2 values are illustrated in Fig. 56. LoD and $RMSE$ values were calculated for each fit according to the previously discussed methodology; these metrics along with the regression fit parameters are listed in Table 11. The R^2

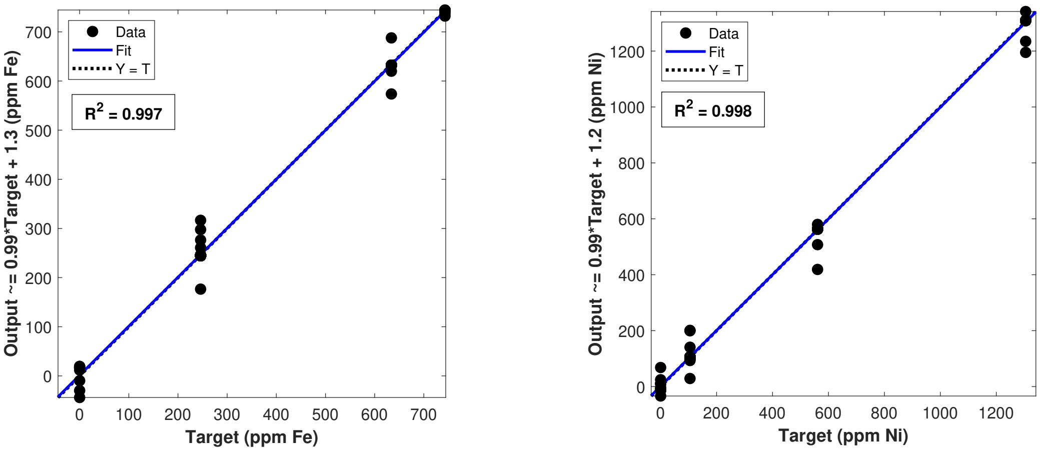

(a) **(b)**

Figure 56. PCR fits of a) Fe and b) Ni data. The fit (blue) to the data (black points) denotes how well the model output prediction of elemental concentration compared to the known target concentration.

Table 11. Regression fit parameters, R^2, LoD and RMSE for PLSR models.

Element	a	b	R^2	LoD (ppm)	$RMSE$ (ppm)
Fe	1.3	0.99	0.997	15	13.2
Ni	1.2	0.99	0.998	20	22.8

values indicate a nearly perfect correlation between the target and predicted analyte concentrations. Each model was able to achieve an LoD an order of magnitude lower than that of their corresponding PCR fits, reaching the low 10s of ppm levels for both elements. This significant improvement in sensitivity is directly attributable to the high slopes of the regression fits to the PLS prediction data. Additionally, significant improvements in *RMSE* were made with this model when compared to the univariate and PCR methods, with the Fe regression reaching the low 10s of ppm levels for error. These values show promise that the PLS algorithm can accurately track small changes in spectral intensity caused by variations in trace metal content, and accurately represent these trends in a quantitative model. Overall, the PLSR models performed substantially better than the PCR models evaluated earlier, showing vastly increased sensitivity and higher predictive accuracy. To determine exactly why PLSR outperforms PCR to this degree, we examined the variance explained by each latent variable for each part of the data. Unlike PCA, PLS also generates variables explaining the covariances between the input (spectral data) and output (metal content); this is illustrated in Fig. 57. The first 3 LVs explain over 95 percent of

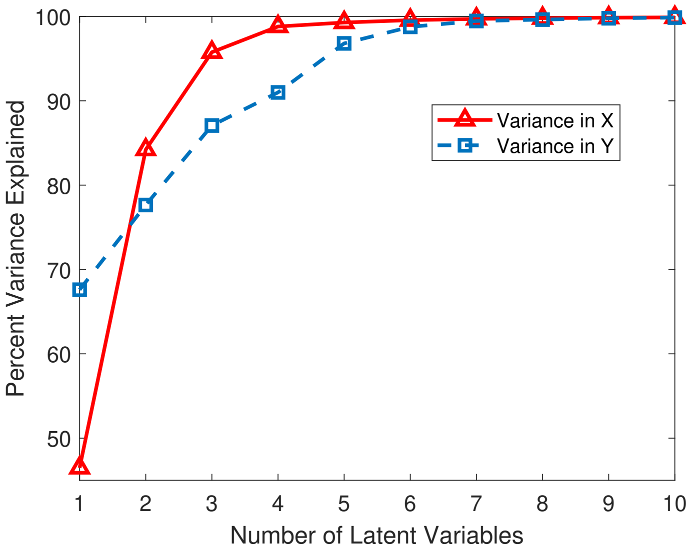

Figure 57. Percent variance in total input (X) and target (Y) data explained by cumulative LVs of PLS model. Constructing a regression with more LVs yields a model explaining a higher portion of the total data variance.

the variance in X, but also account for about 85 percent of the variance in Y. The PLSR model uses the transformed data relating the input and output variables in the regression and is able to better quantify the relationships between spectral response and trace metal content. As a result, it generates better regression fits to the target data and yields lower LoDs for each element than the corresponding PCR models. These results indicate that a supervised learning technique is necessary to properly capture and quantify the relationship between spectral emission variations and trace metal content in the plutonium metal.

4.6 ANN regression results

A shallow feedforward neural network (FFNN) with 100 neurons in the hidden layer and a scaled conjugate gradient optimization function was built to perform regression fits of the data for both trace elements. This specific structure was chosen since it was applied in a previous study on Pu surrogate material spectra for detection of Si [72]. A 60/20/20 % training/validation/testing split was applied to the full set of 145 spectra. Figs. 58 and 59 display the training (blue), validation (green), testing (red) and total (grey) regressions for Fe and Ni content determination. R^2 values for each elemental model and partition are listed in Table 12. The training and validation fits for Fe showed high R^2 values, but the test regression significantly underperformed with a poor R^2 of 0.492. This result provides a primary indication that the FFNN failed to generalize an accurate predictive model for new spectral data, despite achieving good fit metrics for the data during training and validation. Additionally, the FFNN test regression data for Fe yielded an LoD of 290 ppm, four times higher than the LoD of the PLSR for Fe, indicating significant underperformance for iron content prediction.

Table 12. R^2 values for ANN training, validation, test and total regression fits for each elemental model.

Element	Train	Validate	Test	Total
Fe	0.977	0.960	0.492	0.834
Ni	0.940	0.975	0.813	0.921

Fig. 60 illustrates the performance curves for the ANN models built for the Fe and Ni regressions over each training cycle (epoch). The blue, red, and green lines respectively note the mean-squared error (MSE) yielded by the model at a certain epoch for the training, validation, and test data. In both models, the test performance curve terminates at an MSE about an order of magnitude higher than the training and validation MSEs. This indicates the occurrence of overfitting; the

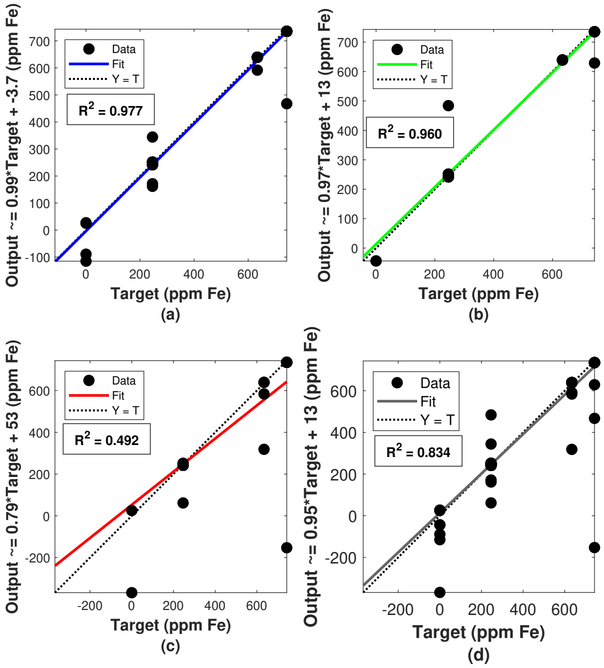

Figure 58. FFNN a) training (blue), b) validation (green), c) testing (red) and d) total (grey) regression fits for Fe content prediction.

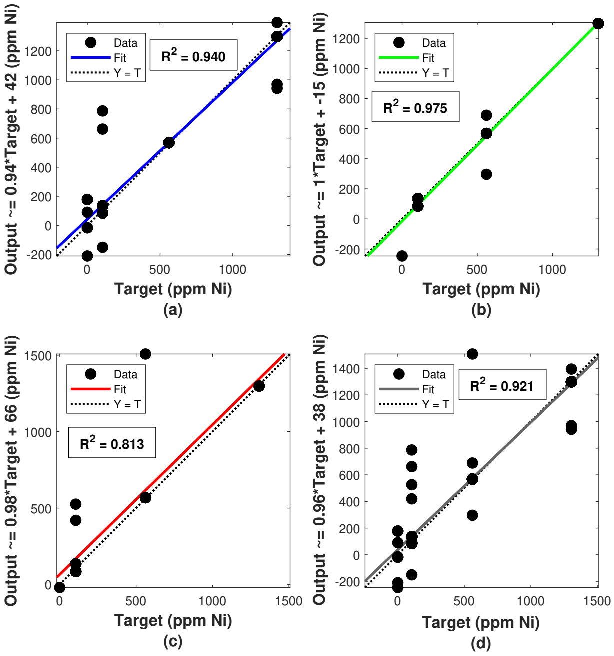

Figure 59. FFNN a) training (blue), b) validation (green), c) testing (red) and d) total (grey) regression fits for Ni content prediction.

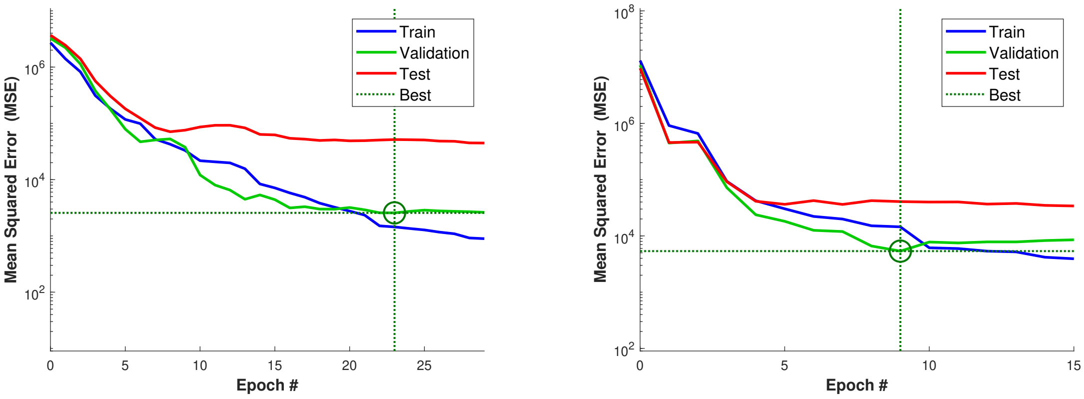

(a) **(b)**

Figure 60. Performance curves for a) Fe and b) Ni regressions denoting change in MSE for each ANN model during training (blue), validation (green) and testing (red) over each training cycle (epoch). The order of magnitude disparity between the end result of the test curve to the training curve indicates overfitting.

model failed to generalize the results from training and validation to new data and could not generate accurate predictions for the test set. Further evidence of this behavior is listed in Table 13, which displays *RMSE* of the training set, root mean-squared error of cross validation (*RMSECV*) for the validation set, and root mean-squared error of prediction (*RMSEP*) of the test set. The model generates order of magnitude higher errors with the test data than with the training or validation set, indicating a failure to generalize the trends from the spectral information. Overfitting often plagues ANN based regression models when large and complex data sets are being passed for training and prediction. The behavior seen in the performance curve indicates that the ANN models are operating with low bias and high variance. This result indicates the need to implement methods such as hyperparameter tuning and regularization to increase bias and lower variance to overcome overfitting. The

Table 13. Root mean-square errors for training, validation and testing ANN regression models for Fe and Ni. All error values are in ppm.

Element	$RMSE$	$RMSECV$	$RMSEP$
Fe	28.9	50.6	211
Ni	62.6	73.2	184

performance curve results also reflect the disparity between the R^2 values of the training and test regressions in Fig. 60. Combining the evidence of the poorer test regression fit and higher test MSE rendered by the Fe and Ni prediction models, it is clear that the chosen ANN architecture cannot produce an entirely reliable or robust model for concentration determination of these two trace metals. The test data regression fitting parameters and evaluation metrics for all ANN models are listed in Table 14.

Table 14. Regression fit parameters, $\mathbf{R^2}$, and LoD for ANN models.

Element	a	b	R^2	LoD (ppm)
Fe	53	0.79	0.492	290
Ni	66	0.98	0.813	150

V. Analysis of Ce with portable XRF device

The Bruker S1 Titan model 800 was implemented for analysis of the cerium-gallium pellets. This experiment used a generation energy from 15-40 kV, and a multi-phase recording over 120 seconds to generate and record a broad range of elemental x-ray excitation emissions from the cerium pellets. 20 recordings were taken of each of the 9 different sample concentrations, yielding 180 total spectra for calibrations. The XRF spectrum of cerium is remarkably simpler than its LIBS spectrum; Fig. 61 illustrates the XRF spectrum of pure CeO_2 with the three major Ce L-shell emissions annotated. The L designation signifies the emission occurs from an electron transitioning to fill a vacancy in the L-shell. The Greek letter subscripts depend on the quantum number change associated with the transition. It is clearly evident that the XRF spectra will prove much less challenging to analyze, as even the heavier lanthanide metals only have a few tabulated x-ray emissions that show up on the spectrum.

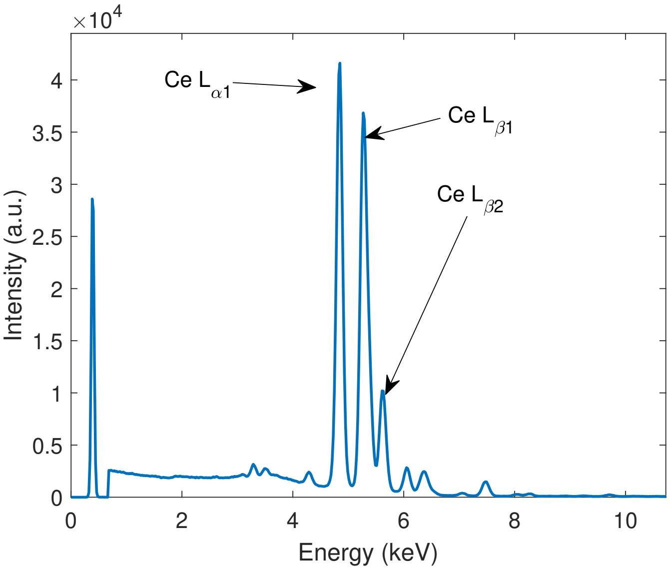

Figure 61. Pure cerium oxide XRF spectrum recorded with the Bruker S1 Titan.

Two major Ga K-shell emissions were identified in the spectra of the samples;

these are illustrated in Fig. 62. The intensity of both these major emissions shows a clear linear variation with increasing Ga concentration in the samples. Additionally it should be noted that because the physical mechanism of XRF doesn't require the generation of a plasma to induce photon emissions, the XRF spectrum isn't susecptible to plasma physics phenomena such as self-absorption, which was clearly seen in the pLIBS spectra in Section 4.1. As a result, it can be expected that univariate calibrations from these spectra will be more sensitive and precise.

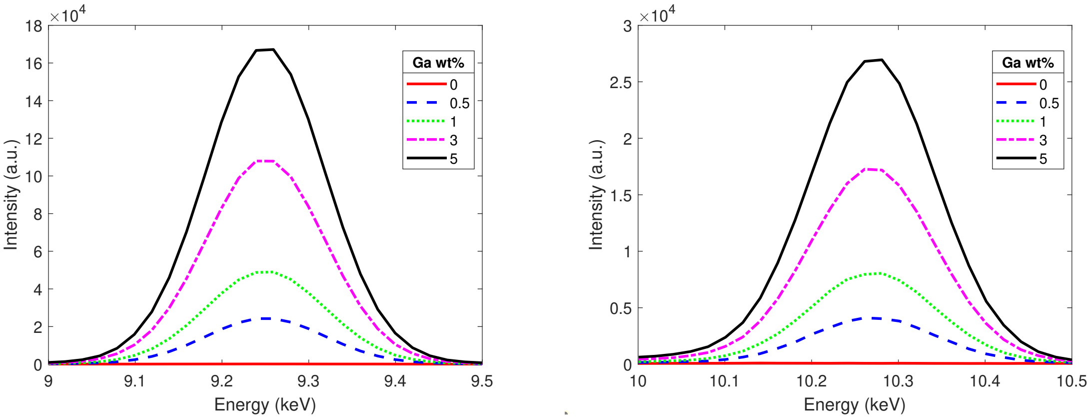

(a) **(b)**

Figure 62. Ga K-shell peaks at a) 9.25 keV and b) 10.26 keV varying with increasing Ga content.

The selected XRF emissions were used to construct calibration curves to contrast to the LIBS calibration models analyzed earlier. Since XRF doesn't generate a plasma and induces electronic emissions by perturbing individual electrons rather than the bulk sample, there are no physical phenomena such as self-absorption to affect the intensity data collected by this device. This is clearly demonstrated in the calibration curves for the K_α and K_β peak intensities in Fig which demonstrate nearly perfect linear fits to the data points. The *MAPE* and LoD values calculated for each calibration are listed in Table 15. The XRF calibrations yield a mean error percentage of the same order of magnitude as the corrected handheld LIBS calibrations discussed in Section 4.1, with less than 10 percent error shown by the models

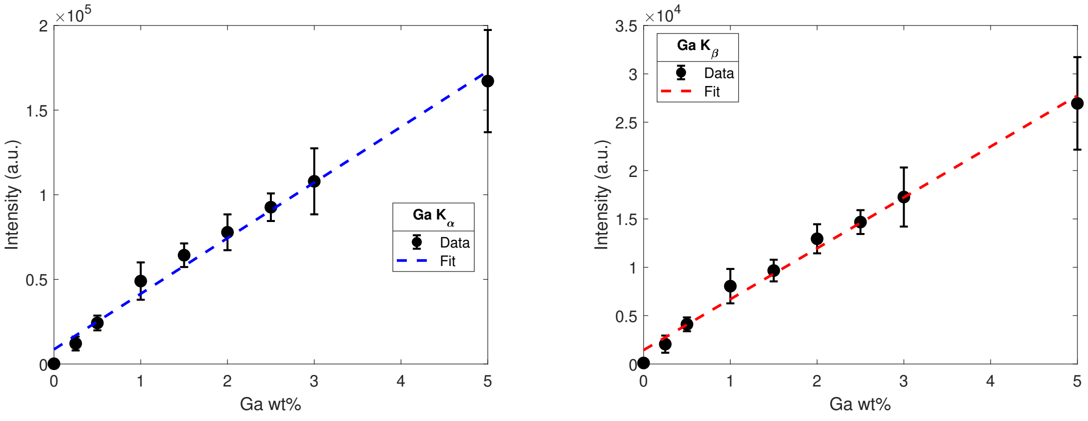

(a) **(b)**

Figure 63. Calibration curves relating Ga concentration to intensity changes of a) Ga K$_\alpha$ and b) Ga K$_\beta$ peaks.

created with either devices. While the 500 ns delay portable LIBS calibrations are still slightly more accurate by a few percent, a significant overall improvement over the LIBS calibrations is attributed to the LoD values for the XRF models. The LoDs for the K$_\alpha$ and K$_\beta$ curves reach 0.002% and 0.008% Ga, respectively. To achieve such low sensitivities from LIBS, either a large laboratory laser and spectrograph setup are needed, or complex machine learning algorithms are required for analysis of the LIBS spectra. Additionally, the effects of self-absorption in a LIBS plasma often hamper the sensitivities of calibration models, even when the intensity values are corrected. The distinctly linear response to concentration yielded by the fluorescence technique created a robust model with excellent detection capabilities and superlative responsivity to changes in Ga concentration. This result points to significant advantages of the portable XRF for the detection of gallium in a cerium matrix. The method provides a significantly less complex data set for chemometric analysis, and can circumvent the

Table 15. XRF univariate calibration fit metrics: *MAPE* and LoD for each emission peak.

Peak	*MAPE*	LoD
K$_\alpha$	9.8 %	0.002%
K$_\beta$	8.3%	0.008%

many physics processes which occur in a laser-induced plasma which can detriment the accuracy of LIBS spectra based quantitative calibration models. As a result, the XRF was able to yield superior quantitative models in this study. Drawbacks to note of the XRF device are the durability of the device itself and the data acquisition time. While a LIBS measurement can be conducted in less than a second, the XRF needs a timescale of minutes to generate reliable spectra. Additionally, the Bruker Titan relies on a delicate silicon drift detector (SDD), which can be sensitive to changes in temperature or damage from impact shocks to the device. Lastly, a key potential drawback of the XRF stems from its inability to detect elements lighter than Mg; quality control studies may need to quantify presence minor elements such as Li, Be, B or Na in the Pu matrix to ensure the alloy chemistry is passing comprehensive fabrication standards. Detection of light minor elements can easily be done with the handheld LIBS device. While this study does not seek to chose one device as the superlative method for potential trace element analysis in Pu alloys, the results of this investigation bring up several important factors to consider when choosing these devices for analysis of nuclear material or related endeavors.

This investigation comparing another elemental analyzers to the LIBS device served to discover potential points of consideration when evaluating handheld LIBS or XRF devices for trace element quantification. The complexity of the electronic emissions seen in lanthanide and actinide metals, coupled with deleterious plasma effects such as self-absorption, limit the performance of a handheld LIBS device for analysis of gallium in plutonium or cerium. While precision can be improved using a self-absorption correction and a later delay time to reduce errors down to the low single percent range, the corrected sensitivity is not greatly affected by increasing gate delay. In fact, the reduction in recording signal could potentially increase the detection limits at later delay times. The XRF device yielded much cleaner calibration fits with comparable errors on the same order of magnitude as the corrected LIBS fits. The XRF calibrations saw immense improvements in sensitivity, showing LoDs as low as 0.002% for the detection of Ga. Although the XRF needs longer timescales for data acquisition and relies on more sensitive components for detection, it produced quantitative models with objectively superior sensitivity and for the problem examined in this experimental work.

VI. Laboratory scale LIBS setup results

The full-scale LIBS setup described in Section 3.2.3 was implemented for an initial higher resolution univariate study of the cerium-gallium pellet spectra. The laser was run at an energy of 100 mJ/pulse, with other laser and camera parameters set as discussed in Section 3.2.3. The burst mode of the DDG and a 3.5s delay between shots was used to capture 20 spectral recordings of each sample concentration (0, .25, .5, 1, 1.5, 2, 2.5 3, and 5 wt% Ga). The initial data set was captured with a 500 ns gate delay, and found that the major Ga I emission at 417.2 nm was present in all spectra containing Ga. This is of note because emissions in this range were not extractable from the Z300 data due to the limited resolution. The Echelle spectrograph used in the laboratory setup had an order of magnitude better resolution than the Z300, at $\Delta\lambda = 0.01$ nm, making peaks in this more cluttered bandwidth easily resolvable. The difference between the spectra around the emission line wavelength is show in Fig. 64.

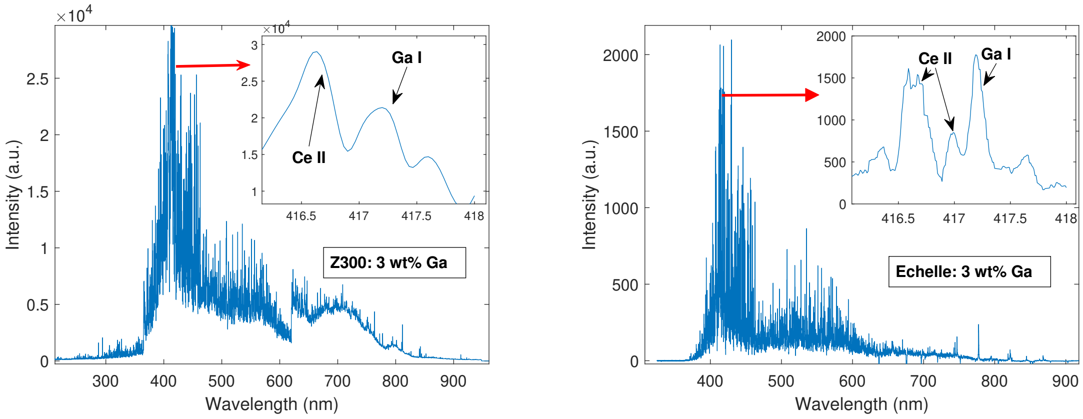

(a)

(b)

Figure 64. Comparison of the resolution of the Ga I 417.2 nm peak as recorded with the a) Z300 and b) Echelle.

A filtering routine was implemented to pre-process the extracted spectral data around the 417 nm peak. A 7-point Savitzky-Golay filter was applied to removed continuum noise from the peak, and a third order 1D median filter was applied to further remove noise from the peak wings of each recording. These parameters were optimized to remove signal noise while minimizing peak information loss. Once a successful pre-processing routine was solidified, the LIBS measurements were repeated on the samples at gate delays of 250 and 1000 ns to evalute temporal changes of the Ga I 417 nm line. Fig. 65 illustrates the relationship between emission line intensity and Ga concentration for 5 of the 9 samples at each delay time; each peak taken from the average of the 20 spectra taken of each sample at each gate delay. While

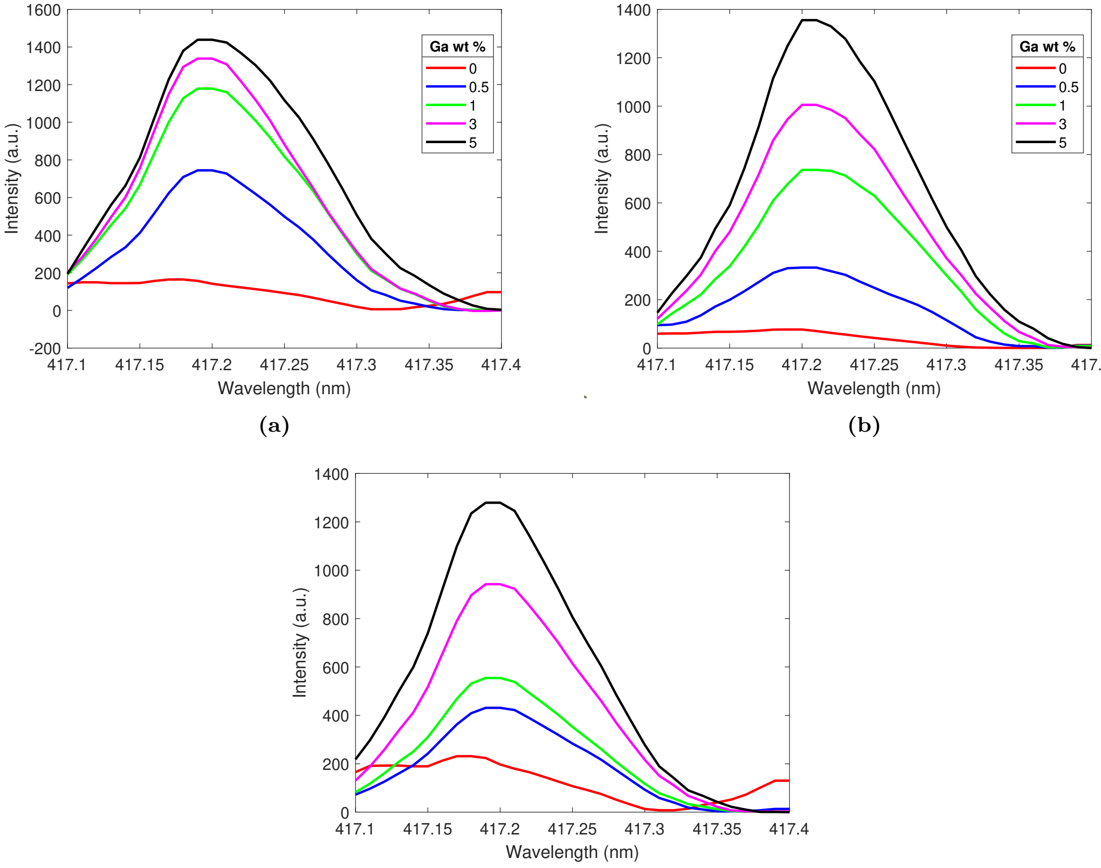

(a) (b)

(c)

Figure 65. Ga I 417.2 nm line intensity relationship to Ga concentration at (a) 250 ns (b) 500 ns and (c) 1000 ns gate delay.

the intensity follows the expected trend of increasing with Ga content at each gate delay, the behavior at 250 ns differs significantly from the other two times. At 250 ns it would appear that the increase in intensity begins to fall off as the Ga content approaches 5 wt%, with the overall trend being distinctly nonlinear. This effect is much less pronounced at 500 and 1000 ns. This initial visual inspection of the emission lines points to the presence of self-absorption suppressing intensity increases at higher concentrations, particularly at early gate delay times. This result hints at self-absorption being more prevalent earlier in the plasma lifetime.

6.1 Evaluation of Temporal Self-Absorption Behavior

Calibration curves relating the peak intensity of the Ga I 417 nm line to the Ga concentration were built for all three gate delay times. The 20 recordings taken for one sample at a given delay time were averaged; intensity of the Ga line was extracted from this averaged spectra, and uncertainty was calculated as the standard deviation of the peak intensity between each shot in one set of 20 recordings. To quantitatively evaluate self-absorption, a power curve in the form of Eq. 12 previously described in Section 4.1 was fit to the data to yield a calibration curve. This provided a relationship between the peak intensity (I) at each concentration (C), which varied based on an intercept factor (a) and an exponent (b) known as the self-absorption (SA) coefficient. A curve with $b \approx 1$ denotes no self-absorption, and smaller values of b indicate the greater effect of the phenomenon on the spectral intensity. Calibration curves of this form have been used in previous LIBS experiments to evaluate self-absorption behavior [75, 76].

The corresponding power fits to the peak intensity data at each gate delay time are illustrated in Fig. 66; the calibration curves clearly demonstrate the presence of self-absorption in the plasma bending the curve downwards. The fitting parameters for each data set are listed in Table 16. A visual inspection of each calibration curve concludes that self-absorption has a greater effect on the calibration at an earlier

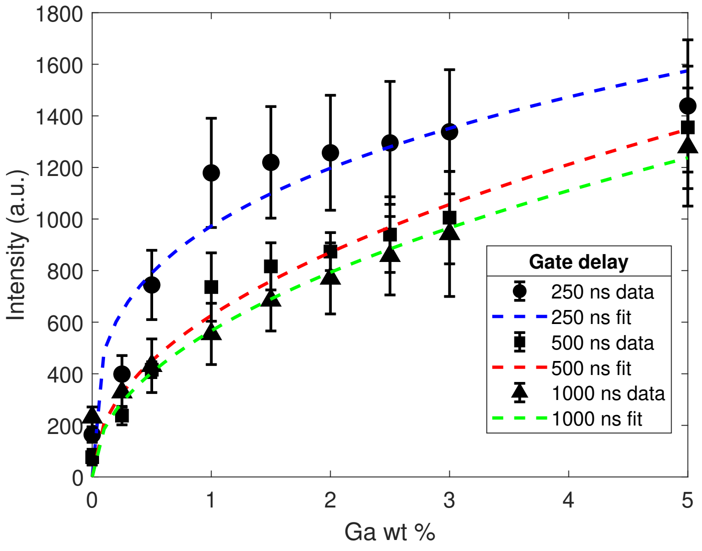

Figure 66. Calibration curves using Ga 417 nm peak intensity at 250, 500 and 1000 ns gate delay.

Table 16. Calibration curve coefficients at each gate delay time.

t_d	a	b
250 ns	972.9	0.2992
500 ns	626.0	0.4764
1000 ns	566.4	0.4855

gate delay, as the 250 ns curve shows a more pronounced 'elbow' where the curve deviates from linear behavior. However, collecting the spectra at later times reduces recorded signal intensity as the LIBS plasma is significantly cooler, which diminishes the sensitivity of a derived calibration curve [26]. Thus, there is a trade-off between the mitigation of self-absorption effects and achievable univariate calibration sensitivity when increasing the gate delay. This trend is expressed in the fitting parameters shown in table 1 as longer gate delays yield a lower 'a' coefficient (sensitivity) while improving the 'b' coefficient (self absorption). One should also note that continuing to extend the gate delay leads to diminishing improvements in self absorption after about 500 ns while sensitivity continues to decrease at faster rate. This behavior indicates that extending the gate delay can only partially mitigate the effects of self-absorption, as the increases in linearity will plateau while the loss of total signal persists.

6.2 Self-Absorption Correction Results and Analysis

The methodology discussed in Sect. 3.3.2 was implemented to correct for the effects of self-absorption of the Ga I 417 nm line. Fig. 67 displays the mathematically corrected calibration curves (blue line) at each gate delay. The SA correction formulation yields a noticeably more linear calibration curve that follows the expected intensity. To evaluate the corrected and uncorrected calibrations, the $MAPE$ and LoD are again calculated as measures of model precision and sensitivity, respectively. Table 17 lists these calculated parameters for each gate delay time; $MAPE$ was calculated for both corrected and uncorrected calibrations to examine how the mathematical correction affects precision. The uncorrected calibration error reveals another temporally varying behavior of the calibration curves; $MAPE$ is reduced as the gate delay time is increased, hinting that the uncorrected models have higher precision at longer delay times. The earlier analysis of the self-absorption coefficient behavior indicated that the effects of self-absorption were less prevalent at later gate delays. The mathematical correction greatly reduced the error of all three models, with the 1000 ns calibration being the most accurate with a $MAPE$ of 4.3%. These improvements clearly indicate that implementing the SA factor correction yields a more precise calibration, and could help circumvent the deleterious effects of self-

Table 17. Percent error of calibration before and after SA correction, and LoD of the corrected linear calibration model at each gate delay.

t_d	Uncorr. MAPE	Corr. MAPE	LoD
250 ns	23.5%	7.56%	0.008%
500 ns	19.5%	13.6%	0.009%
1000 ns	14.8%	4.31%	0.015%

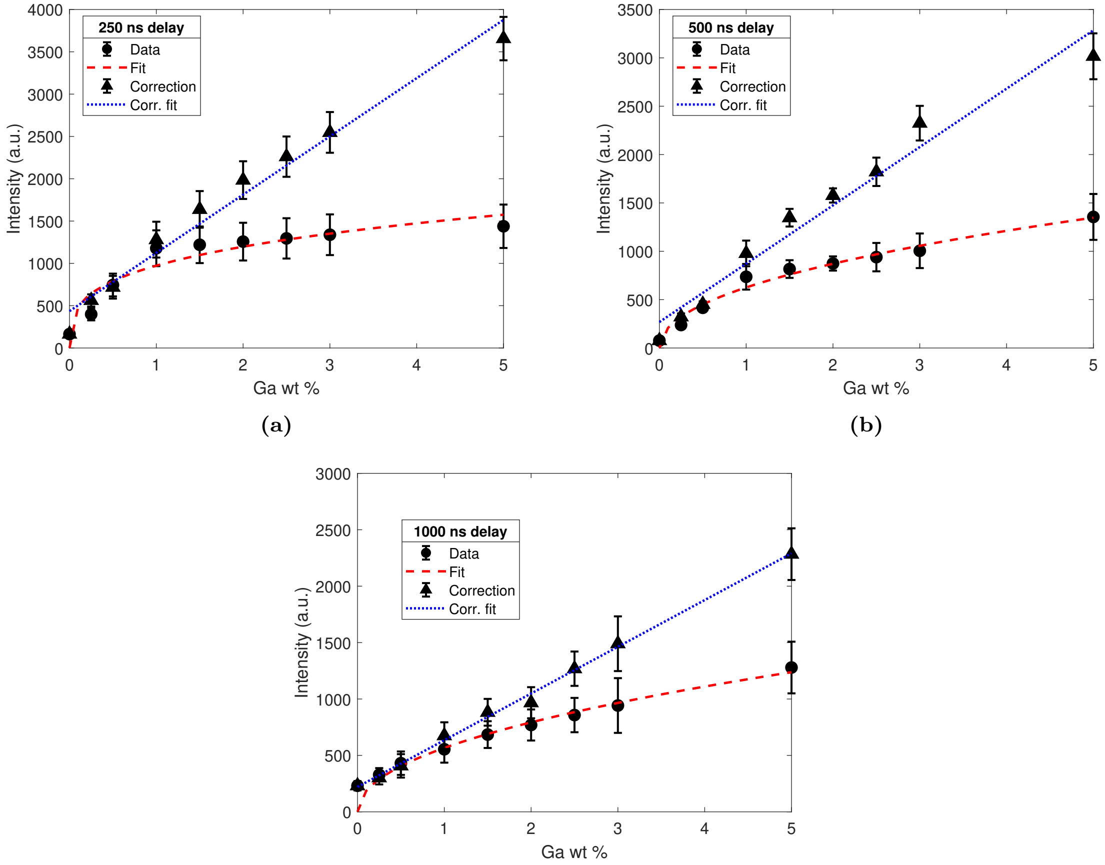

(a) (b)

(c)

Figure 67. Self-absorption corrections of Ga calibration curves at a) 250 ns b) 500 ns and c) 1000 ns.

absorption on calibration accuracy. The sensitivity of the corrected model, evaluated by the LoD, appears to follow the opposing trend as gate delay is increased. Due to the lower intensities recorded at longer gate delays, the slope of the corrected calibration decreases as delay is increased. This in turn increases the LoD of the corrected model, rendering the calibrations slightly less sensitive as t_d is raised. The 250 ns calibration is most sensitive with an LoD of 0.008 wt% Ga. The 500 and 1000 ns fits yield LoDs of 0.009 and 0.015 wt% Ga, respectively. Reaching sub 100s of ppm sensitivity levels for a univariate calibration quantifying metals in lanthanide or actnide matrices is often difficult with LIBS data due to combined effects of self-absorption and other chemical matrix effects. However, the results of this study indicate that performing the mathematical correction can help boost calibration sensitivity even when faced with physical phenomena that detract from the reliability of the spectral recording.

These results serve as an initial, proof-of-concept that using a self-absorption correction can help mitigate plasma effects and yield more robust calibration models. Additionally, it also serves to demonstrate the trade off between sensitivity loss and precision gain when extending the gate delay of a spectral recording to circumvent self-absorption. These results set the foundation for further investigations of other analytical methods to improve the efficacy of regression models without having to implement physics-based corrections to the spectra. Notably, the complex spectral response and physical effects in the plasma hint at the need to apply machine learning methods to yield better analytical solutions for this problem.

6.3 Machine Learning Model Study

The last major phase of this analysis sought to test several machine learning methods on the spectra acquired with the laboratory setup to examine how enhancing the resolution of the recordings and tuning ML models could help boost fidelity of the predictive regression models. Using the same Ce-Ga pellet set between 0-5 wt% Ga, 40 recordings of each sample concentration were taken at a delay of 500ns and laser energy of 100 mJ/pulse; other camera, laser and delay settings were kept the same as used for the univariate data set collection. The ML workflow layed out in Section 3.3.3 was implemented in full for this analysis. Firstly, normalization and feature reduction were applied to the raw data set; 40 recordings at 9 different Ga concentrations yielded a data set of 360 recordings with 60,001 wavelength variables each. The raw data was normalized with the SNV method used previously and described by Eq. 16. This was done to reduce signal fluctuation and hopefully boost the training performance of ML models used on the data set. Next, a PCA decomposition was performed to analyze the loadings values in the broadband 325-925 nm spectra. The loadings

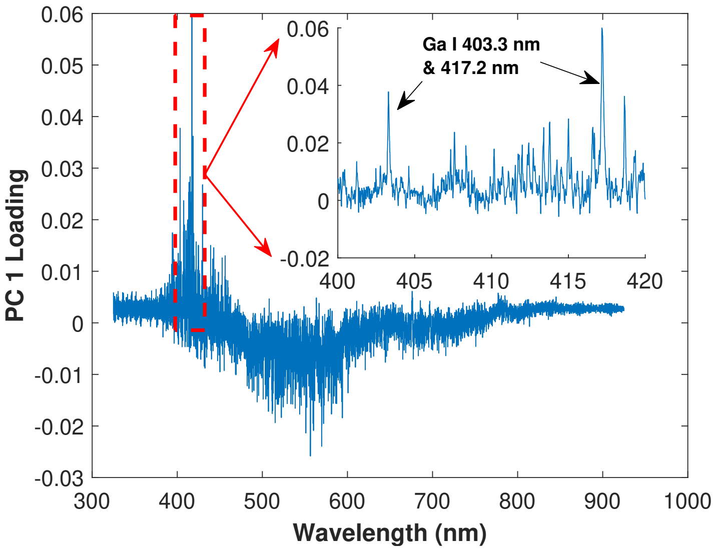

Figure 68. PC 1 loadings of each wavelength in the data. The two wavelengths corresponding to the strongest Ga I emissions load the highest, and therefore contribute to most of the total variance of the data.

of each wavelength on the first PC, which explains more than 65% of the variance of the original data, are shown in Fig 68. The inset portion of the figure shows the two largest tabulated Ga I emissions loading the highest on this PC, indicating that they explain a significant portion of the variance in the data. As a result of this initial analysis, the normalized data set was then reduced from the full 325-925 nm spectra to just the 400-420 nm range, cutting the total data set down to a 360x2001 matrix. This significantly simplifies the data set allowing for higher computational efficiency when training the selected ML methods for regressions. Lastly, the filtering routine using a 7-point SG filter and 3rd order median filter described earlier were implemented to finish the preprocessing method.

The eight different machine learning paradigms discussed in Section 2.7 were chosen for optimization, training and testing. These include: decision trees, bagged ensemble regression, boosted ensemble regression, extra trees, random forest, support vector regression, kernel regression and artificial neural networks. The following sections describe the hyperparameter optimization experiment and training results.

6.3.1 Optimization of Hyperparameters

An automated hyperparameter optimization routine was implemented on all the selected regression models. This routine used a Bayesian optimizer to run through a set range of values of all tunable hyperparameters of each model, changing the values from one iteration to the next in order to minimize model error (mean-squared error). Each optimization was run for 30 iterations, which was enough learning cycles for all models to converge to a low error value after hyperparameter tuning. Table 18 shows a comprehensive list of all regression models, tunable hyperparameters, and ranges of values examined to determine the best model of each kind. Leaf size and number of splits were tuned for a single decision tree model. Minimum leaf size refers to the depth of each tree in the ensemble, or the number of decision nodes, where maximum number of splits refers to the number of total branches created from all the nodes in the tree. For ensemble regressions, both bagged and boosted models were examined. The number of learning cycles (i.e., the number of predictors) was varied for both types of ensembles. The boosted ensemble learning rate was also tuned; this parameter affects how much the contribution of each subsequent learner shrinks. Additionally, extra trees and random forest were tuned for leaf size, number of splits, and learning cycles. Kernel function bandwidth (h) and error margin ϵ were tuned for both the SVR and GKR to adjust the input weights and function error tolerance, respectively. SVR optimization also examined three types of kernel functions to generate weights, and tuned the slack variable ξ for misclassification penalty. The GKR optimization also examined a parameter called regularization (λ); this variable is used to penalize overly complex models and encourage the development of simpler regression models to the input data. This is implemented to prevent overfitting. Regularization constants were also examined in the ANN optimization. Three types of single layer ANNs were tested, with narrow, medium and wide referring to an increasing number of neurons in the single layer. Bilayer and trilayer architectures were also examined with varying numbers of neurons in the different layers as well. Three different activation functions were examined during tuning to optimize the weight values generated by each neuron, and the training iteration limit was varied from 100-10000 to adjust how much time the model had to converge. All ANNs tested in the optimization experiment used a limited memory Broyden-Flecter-Goldfarb-Shanno quasi-Newton algorithm (LBFGS) for loss function minimization, based on the mean-squared error (MSE). The tuned values of all model hyperparameters used for analysis of predictive regressions are listed in the last column of Table 18.

The tuned hyperparameter values for each model were saved and used to construct optimized models which were subsequently trained and tested on the processed spectral data. The goal of implementing this design optimization routine is to preemptively drive down the loss of each regression model via hyperparameter tuning, such that the best performance possible is obtained when the tuned model is exposed to test data. In particular it should be noted that in previous portions of this research, the ANN models used failed to generalize training results to test data and could not yield robust predictive models for determining trace elements in the Ce spectra. Only simple FFNN structures were implemented in previous analyses; this design process examined other ANN architectures and introduced significantly more variables in order to develop more robust models which are not plagued by overfitting. Doing this successfully would be a huge achievement, as a well-tuned ANN would have the potential to yield extremely sensitive regression models with minimal prediction error.

Table 18. Hyperparameter optimization options for all models

Model	Hyperparameters	Range	Tuned Value
Tree	Min. Leaf Size	1-144	20
	Max Num. Splits	1-100	61
Bag	Min. Leaf Size	1 - 144	10
	Num. Learning Cycles	10 - 500	495
Boost	Max Num. Splits	1 - 100	34
	Num. Learning Cycles	10 - 500	180
	Learning Rate	0.001 - 1	0.095
ET	Min. Leaf Size	1-144	20
	Max Num. Splits	1-100	5
	Num. Learning Cycles	10-500	300
RF	Min. Leaf Size	1-144	20
	Max Num. Splits	1-100	10
	Num. Learning Cycles	10-500	300
SVR	Kernel Function	Linear; Gaussian; Polynomial	Linear
	Slack (ξ)	0.001 - 1000	200.2
	Bandwidth (h)	0.001 - 1000	454.7
	Error (ϵ)	1.48e-3 - 148	0.362
GKR	Bandwidth (h)	0.001 - 1000	51.14
	Regularization (λ)	4.99e-7 - 0.499	1.72e-5
	Error (ϵ)	1.48e-3 - 148	1.51e-3
ANN	Layer size	Narrow; Medium; Wide; Bilayer; Trilayer	Trilayer
	Number of neurons	2 - 50	[20;10;10]
	Activation Function	ReLU; Sigmoid, tanh	sigmoid
	Iteration Limit	1e2 - 1e4	1000
	Regularization (λ)	4.99e-7 - 0.499	4.96e-5

6.3.2 Tuned Machine Learning Model Results and Analysis

Once tuned hyperparameter values for each model had been selected, prediction models using those values were created and trained on the data set. An 80/20 percent holdout validation split was applied to separate 20% of the spectra for testing after the models had been trained. The tree-based regression methods were created and analyzed first with the corresponding tuned hyperparameter values listed in Table 18. All tree-based model test regressions are shown in Fig. 69.

The lone decision tree fared poorly, showing significant dispersion in the prediction points, indicating a failure to properly generalize the complex spectral relationships. This is expected, as single decision trees are fairly simple models which can struggle

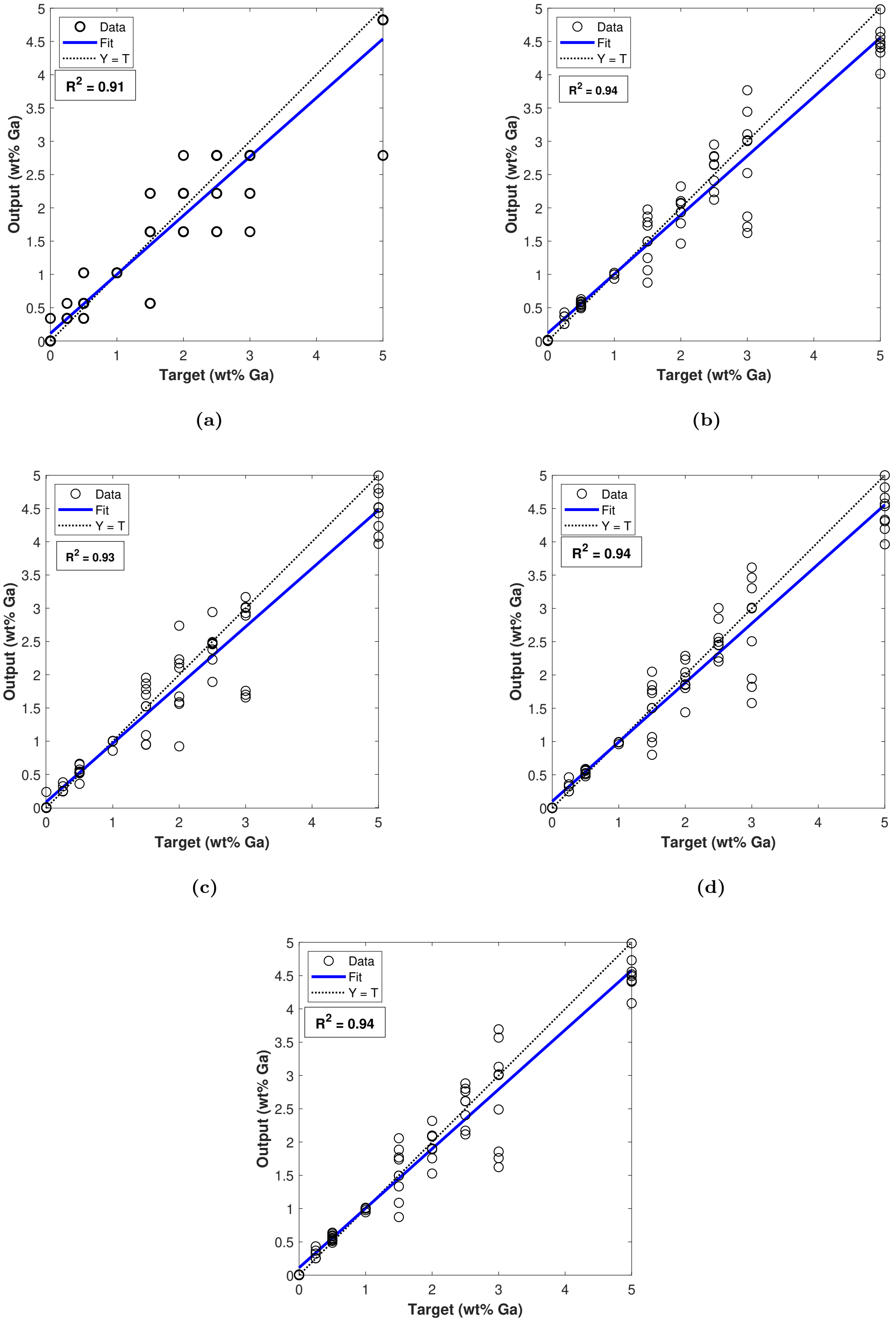

(a)

(b)

(c)

(d)

(e)

Figure 69. Tree based test regressions showing prediction results from a) decision tree b) bagged ensemble c) boosted ensemble d) extra trees and e) random forest.

to make accurate predictions when faced with complex, nonlinear data set. The other four models yielded test regressions with very similar linearity values; to fully evaluate these we examine their error and detection limits. These evaluation metrics are listed in Table 19. The tree ensemble methods clearly outperformed the lone decision tree, with all four showing improved *RMSEP* values. For the most part, these errors are lower than the errors generated by the machine learning models created from the Z300 spectra, indicating an improvement in precision with the higher resolution spectrometer. However, the bagged model in this study had error around a tenth of a percent higher than the bagged model created to predict the Si concentration in Ce from the Z300 spectra. This indicates there may be a limit to how low the prediction error can be driven with this setup. Examining the regression figures reveals a larger range of predictions for intermediate samples in the 1.5-3 wt% Ga range. A potential cause of this dispersion may stem from inhomogeneities in the pressed pellet caused by static buildup in the homogenizer capsule. One solution which should be investigated for future studies is implementing different types of pellet binders to enable proper dispersion of the minor analyte and form a more homogeneous pellet.

Table 19. Tree based regression model *RMSEP* and LoD values

Model	Tree	Bag	Boost	ET	RF
RMSEP	0.475%	0.394%	0.422%	0.394%	0.391%
LoD	0.366%	0.025%	0.256%	0.006%	0.018%

The main takeaway from these results is evident in the LoD values calculated for the ensemble models. With the exception of the boosted regression, the other models were able to reach sensitivities below a tenth of a percent. In particular, the extra trees regression yielded a sensitivity of 0.006%, or 60 ppm Ga. This is an extraordinary improvement over previous models, indicating that the high resolution spectra allowed for the creation of much more sensitive prediction models. Achieving

LoDs in the low tens of ppm for quantification of Ga in Pu with LIBS would be a significant accomplishment for the Pu production quality control procedure, and this result indicates that using machine learning paradigms with LIBS data can feasibly accomplish this goal. The higher LoD of the boosted model must be noted however, as it barely improved on the LoD of the lone tree. Examining Fig. 69c, particularly the 0 wt% predictions, reveals higher dispersion of the intercept from the boosted regression than seen in the other ensemble models. This directly contributes to a higher σ_a value, thereby increasing the calculated sensitivity. It is not immediately clear why the boosted ensemble test regression failed to accurately identify a blank sample spectra when compared to the other models.

The test results from the three remaining tuned ML models (SVR, GKR, and ANN) are shown in Fig. 70. Error and sensitivity calculations are listed in Table 20. The SVR model yielded higher comparative prediction errors to all the tree based models, and delivered an LoD of 0.098%, better than only the boosted regression. The GKR and ANN test regressions were able to deliver predictions with errors comparable to the tree-based models; the GKR actually yielded the regression with the lowest error seen in this study at 0.329%. While kernel regression methods are seldom seen in analytical spectroscopy, this result indicates that the methodology of the gaussian kernel function has significant advantages for solving problems with complex and non-linear data. Weighting all inputs as a distribution and using all the input features to form a prediction seems to have allowed this model to yield higher precision outputs to test data when compared to the tree-based regressions. Both the

Table 20. SVR, GKR and ANN model test regression error and sensitivity results

Model	SVR	GKR	ANN
RMSEP	0.611%	0.329%	0.399%
LoD	0.098%	0.015%	0.017%

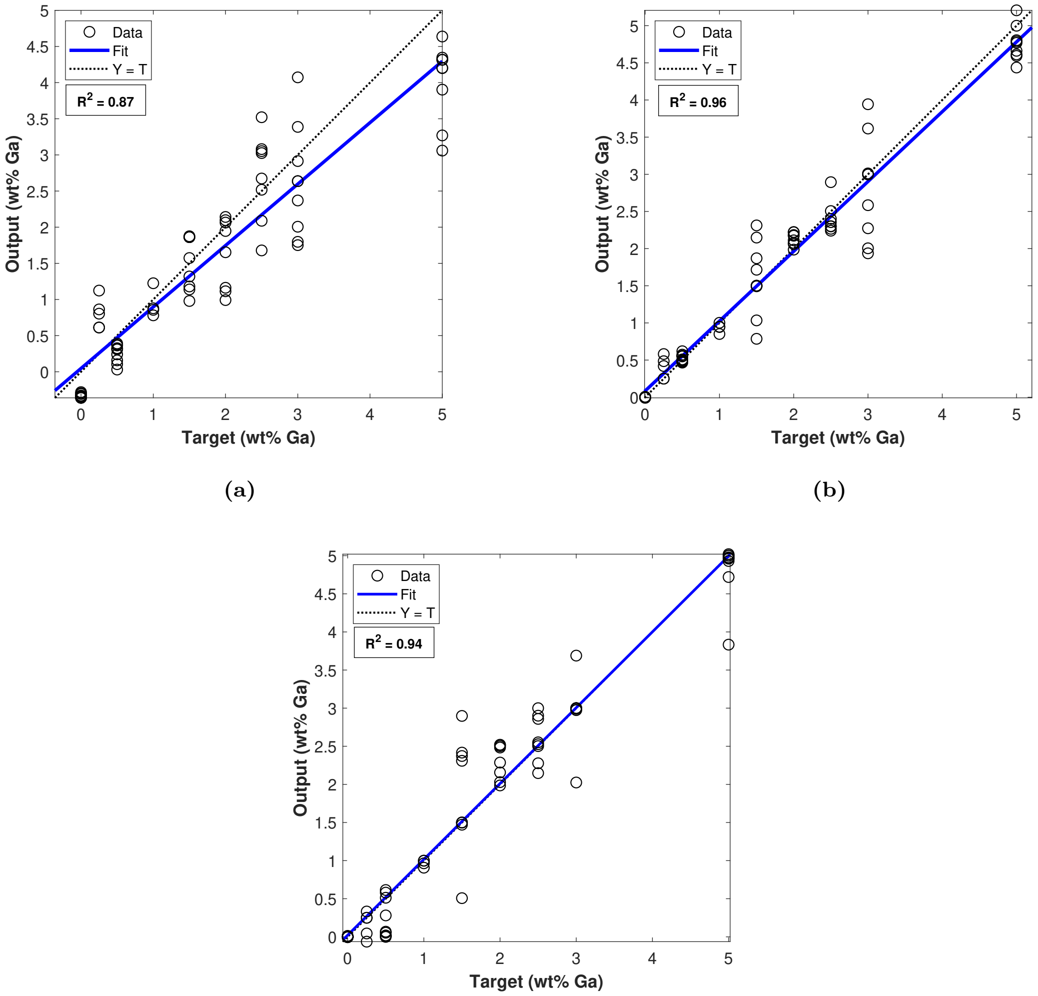

(a)

(b)

(c)

Figure 70. Test regressions showing prediction results from a) SVR b) GKR and c) ANN models.

GKR and ANN delivered comparable LoDs at 0.015 and 0.017%; these sensitivities are superior to all the tree based models except extra trees. It should be noted that the hyperparameter optimization routine enabled the creation of an ANN model which finally overcame the overfitting issues which had plagued previous, simpler ANN models used for spectroscopic analysis earlier in this work. Rather than a simple feedforward construct, the optimization routine indicated that a trilayer ANN (20, 10 and 10 neurons in each respective layer) employed with a regularization of 4.96e-5 would minimize prediction loss. This more complex structure, in addition to implementing a regularization function during training, finally allowed for proper generalization of the trends in the training spectra and the creation of a regression model which could output accurate test predictions.

Overall, the results of this ML workflow analysis reveal several important points. First, that ML paradigms not commonly implemented in spectroscopy, such as the GKR and extra trees, show great potential for the chemical analysis of complex material spectra. The precision and sensitivity metrics yielded in this study indicate promise for applications to plutonium analysis. We are able to reach tens of ppm sensitivity levels for gallium detection when employing these ML paradigms. Secondly, the proper tuning of an ANN architecture can help overcome the overfitting issues which commonly detriment these models when analyzing complex spectra. Implementing more complex ANN structures and employing regularization can create significantly more robust predictive models.

VII. Conclusion

7.1 Summary of findings

This dissertation study encompassed a broad evaluation of different atomic spectroscopy techniques and chemical analysis methodologies, in order to demonstrate the feasibility of alternate approaches for plutonium analysis. Building upon the prior Master's thesis results, the capabilities of the SciAps Z series portable LIBS devices for lanthanide and actinide analysis were fully investigated. While advanced analytical methods yield great improvments in sensitivity for detection of trace elements in Pu, other spectroscopic techniques offer several merits as competetive methodologies.

The SciAps Z300 was used for a complete evaluation of different analytical methods to detect trace elements in plutonium surrogate matrices. Self-absorption was observed and evaluated with the univariate regression methods, and it was determined that the effects of this plasma phenomenon along with the lower resolution of the device called for better spectral analysis methods to be employed. Traditional chemometric methods were compared to machine learning constructs, specifically tree-based ensemble methods. It was determined that using the ensemble regression techniques yielded great improvements in sensitivity and precision over traditional chemometric methods, hinting at the promising efficacy of machine learning techniques. A similar analysis was applied to spectra of actual Pu alloy samples taken with the Z300. It was clearly demonstrated that the significant interference of Pu emissions with the major emission lines of analytes such as Fe and Ni call for chemometrics or ML methods to be applied. PCA, PLS and ANN methods were implemented on this limited data set; PLSR proved superior but was still unable to reach the sub 100s of ppm detection limit desired for this problem.

A portable XRF device was employed on Ce-Ga samples to contrast the performance of the LIBS device. The XRF recordings proved much easier to analyze as even lanthanide metals only have a few notable characteristic emission peaks in an XRF spectrum. This enabled the creation of significantly improved univariate regressions, whose sensitivities reached the high tens of ppm for Ga, far exceeding the sensitivity of the LIBS device even with machine learning employed. However, the univariate calibrations still yielded mean errors in the high single percents. Additionally, the XRF device requires a significant amount of time to take a meaningful spectral recording, whereas LIBS can generate a useable spectrum in fractions of a second. Furthermore, the utility of the XRF for a complete metallurgical quality control analysis is detrimented by its inability to induce flourescence in elements lighter than Mg. Quantifying presence of light minor elements in Pu alloys is necessary for proper quality standards analysis, and a secondary analysis method would have to be implemented in tandem with the XRF device to detect the presence of lighter elements. Overall, the results of the XRF investigation indicated that this portable device has its merits where instantaneous analysis is not required, and high error percentages are tolerable.

Finally, the results of the portable device investigations pointed to the need to perform this analysis on a full laboratory scale setup with a high resolution spectrometer in order to leverage the efficacy of the machine learning methods and the resolving power of an Echelle spectrograph. Firstly, a univariate analysis indicated significant self-absorption behavior in the plasma. This was partially mitigated by recording at later gate delays albeit at the expense of sensitivity. The higher resolution of the laboratory spectra allowed for the use of the major Ga I 417.2 nm emission for calibration. Subsequently, a self-absorption correction methodology was formulated and employed based on Stark broadening parameters extracted from the spectra. This correction yielded order of magnitude lower errors in the calibration, and enabled the regression models to reach detection limits comparable to those of the pXRF. A final comprehensive design experiment was employed to optimize, train and test several ML paradigms to predict Ga content from cerium spectra. These optimized constructs were the most superior predictive models, with the extra trees regression yielding a detection limit of 0.006 wt% Ga. Additionally, the novel Gaussian kernel regression method yielded the lowest *RMSEP* of all the models from all three methodologies in this study at around 0.33%. The last main accomplishment of this optimization experiment was that the ANN model created was able to properly generalize the spectral relationships and generate a robust prediction model, overcoming the overfitting issues that previously examine ANN models had succumbed too earlier in the study.

7.2 Benefits and limitations

This work provides a comprehensive and robust evaluation of different machine learning methods for a complex analytical spectroscopy problem. It effectively proved the usefulness and durability of these models for analyzing trace metal content in Pu and Pu surrogate matrices, even though many of these methods are not typically applied for analytical spectroscopy. The machine learning regressions created in this study, along with the employment of a higher resolution spectrometer, show great promise for enabling precise and rapid measurements of trace metals in Pu alloys with high sensitivity levels.

The efficacy of a standard laboratory laser for this problem is limited by how well a laser beam can be directed into a glovebox where plutonium is contained. Additionally, collecting the spectral emissions from such a setup and directing them into a spectrometer also pose a significant challenge. The likely solution to overcome this would be to utilize fiber optic cables for both beam transmission and atomic emission collection. The drawback of such a setup would be light attenuation by the fiber optic cables, as well as possible issues maintaining a stable beam energy between shots. This work also indicates that the Z300 is more than capable of performing *in-situ* analysis of Pu alloys, as was the original goal of this research. However, even with applying machine learning for the spectral analysis, the sensitivity and accuracy of this device is inevitably curbed by its limited spectral resolution. The device is more than capable of yielding measurements with precision to within tenths of a percent and sensitivities down to the low tenths of percent as well. However, the results of these experimental proceedings do not indicate that the device can yield detection limits in the tens of ppm that standard LIBS setups have previously demonstrated.

7.3 Recommendations for future work

- **Improving sample quality:** Possible inhomogeneities in the surface of the Ce-Ga pellets may stem from the generation of electrostatic forces on the walls of the homogeneizer capsule which cause material to clump. This could be causing improper distribution of gallium in the Ce powder. Developing a new sample creation methodology with a binder to improve homogenization could yield more consistent spectra and more sensitive machine learning regression models.

- **Full range investigation of a variety of minor impurities:** Investigating mixed samples containing several different minor analytes of interest is key to advancing the capabilities of the investigated analytical techniques and pushing the limits of multielemental analysis. The interferences between different minor elements could pose an additional challenge to overcome for the machine learning regression models using LIBS spectra. Additionally it is imperative that the limits of the handheld XRF be verified by analyzing samples with elements

Z<11 present.

- **Fiber laser LIBS setup:** If a higher resolution spectrograph is to be used with a larger LIBS setup for Pu analysis, propagation of the laser beam into the glove box, and subsequent transmission of spectral emissions out, poses a hardware challenge. To adhere to optical safety standards, a proof of concept experiment can be created coupling the current laboratory laser systems to optical fibers transmitting the laser photons to the sample and refocusing the beam to induce ablation. Laser fluence and power loss would have to be evaluated to determine if fiber-coupled LIBS is feasible with current technology. Additionally, the quality of spectra recorded from such a setup must be evaluated for signal-to-noise ratio, LIBS signal stability, and quality of calibrations from the spectra.

- **Laser and spectrometer settings:** The current laboratory setup has a variety of parameters which can be varied, some of which were investigated in this study. The lab Nd:YAG lasers have variable power levels, and conducting a study how laser power affects signal stability and quality of the recorded spectra could yield useful data for future calibration experiments. Additionally, a secondary investigation into altering the gate width and gate delay on the recorded signals can be conducted. Many LIBS measurements use gate delays past the 1 μs range examined in this study, and it would be of interest to study the evolution of Ce-Ga emissions over a longer period of the plasma lifetime.

- **Double-pulse LIBS:** The laboratory setup has the capability to conduct double pulse LIBS, and significant graduate level work could be conducted by investigating the effects of adding a second laser pulse to the current LIBS setup. The reheating of the plasma from the secondary laser pulse could lengthen some of the key atomic emissions used for analysis in this study. Double pulse LIBS is known to enhance emission signals over background noise and yield more sensitive calibration models. Finally, the reheating of the plasma plume from the secondary pulse could have interesting effects on the temperature evolution of the plasma, and subsequently affect how self-absorption manifests in the plasma. The potential of a double pulse setup for mitigating SA effects should be investigated.

- **Ultrafast LIBS** A full study on using pico or femtosecond laser pulses for this LIBS analysis would be of great scientific interest. Ultrafast laser pulses interact with material in a fundamentally different way than nanosecond pulses do. fs lasers have shown cleaner ablations with no thermal damage to the material, and no heat transfer between the ablation plume and the trailing laser pulse. Using an ultrafast laser could potentially yield significant signal enhancement and improve the quality of LIBS calibrations for cerium or plutonium alloy analysis.

- **Fielding handheld analyzers:** Thus far, the handheld analyzers used in this dissertation work have primarily been used in the controlled laboratory environment. The work related to these devices that has been done the last few years indicates these devices have the potential for analysis of not just Pu, but other actinide elements of interest in nuclear science. Fielding them for on-site analysis of nuclear debris or contamination would open up a whole new avenue of capabilities to investigate.

Bibliography

1. P. S. Hsu, M. Gragston, Y. Wu, Z. Zhang, A. K. Patnaik, J. Kiefer, S. Roy, and J. R. Gord, "Sensitivity, stability, and precision of quantitative Ns-LIBS-based fuel-air-ratio measurements for methane-air flames at 1–11 bar," *Appl. Opt.*, vol. 55, no. 28, pp. 8042–8048, Oct 2016.

2. A. K. Patnaik, Y. Wu, P. S. Hsu, M. Gragston, Z. Zhang, J. R. Gord, and S. Roy, "Simultaneous LIBS signal and plasma density measurement for quantitative insight into signal instability at elevated pressure," *Opt. Express*, vol. 26, no. 20, pp. 25 750–25 760, Oct 2018.

3. M. L. Najarian and R. C. Chinni, "Temperature and Electron Density Determination on Laser-Induced Breakdown Spectroscopy (LIBS) Plasmas: A Physical Chemistry Experiment," *Journal of Chemical Education*, vol. 90, pp. 244–247, 2013.

4. L. Pardini, S. Legnaioli, G. Lorenzetti, V. Palleschi, R. Gaudiuso, A. D. Giacomo, D. D. Pace, F. A. Garcia, G. de Holanda Cavalcanti, and C. Parigger, "On the determination of plasma electron number density from Stark broadened hydrogen Balmer series lines in Laser-Induced Breakdown Spectroscopy experiments," *Spectrochimica Acta Part B: Atomic Spectroscopy*, vol. 88, pp. 98 – 103, 2013.

5. U. et al, "Measurements of plasma temperature and electron density in laser-induced copper plasma by time-resolved spectroscopy of neutral atom and ion emissions," *Pramana Journal of Physics*, vol. 74, pp. 983–993, 2010.

6. B. Bhatt, K. Hudson Angeyo, and A. Dehayem-Kamadjeu, "Libs development methodology for forensic nuclear materials analysis," *Anal. Methods*, vol. 10, pp. 791–798, 2018.

7. J. E. Barefield, E. J. Judge, K. R. Campbell, J. P. Colgan, D. P. Kilcrease, H. M. Johns, R. C. Wiens, R. E. Mcinroy, R. K. Martinez, and S. M. Clegg, "Analysis of geological materials containing uranium using laser-induced breakdown spectroscopy," *Spectrochim. Acta B*, vol. 120, pp. 1–8, 2016.

8. J. Klus, P. Mikysek, D. Prochazka, P. Porizka, P. Prochazková, T. T. J. Novotny and, M. S. K. Novotny and, and J. Kaiser, "Multivariate approach to the chemical mapping of uranium in sandstone-hosted uranium ores analyzed using double pulse laser-induced breakdown spectroscopy," *Spectrochim. Acta B*, vol. 123, pp. 143–149, 2016.

9. J. Sirven, A. Pailloux, Y. Baye, N. Coulon, T. Alpettaz, and S. Gosse, "Towards the determination of the geographical origin of yellow cake samples by laser-induced breakdown spectroscopy and chemometrics," *J. Anal. At. Spectrom.*, vol. 24, pp. 451–459, 2009.

10. Y. Kim, B. Han, H. S. Shin, H. D. Kim, E. C. Jung, J. H. Jung, , and S. H. Na, “Determination of uranium concentration in an ore sample using laser-induced breakdown spectroscopy,” *Spectrochim. Acta B*, vol. 75, pp. 190–193, 2012.

11. M. B. Shattan, M. Gragston, Z. Zhang, I. John D. Auxier, K. G. McIntosh, and C. G. Parigger, “Mapping of Uranium in Surrogate Nuclear Debris Using Laser-Induced Breakdown Spectroscopy (LIBS),” *Applied Spectroscopy*, vol. 73, no. 6, pp. 591–600, 2019.

12. R. Chinni, D. A. Cremers, and R. Multari, “Analysis of material collected on swipes using laser-induced breakdown spectroscopy,” *Appl. Opt.*, vol. 49, pp. C143–C152, 2010.

13. A. Sarkar, D. Alamelu, and S. K. Aggarwal, “Determination of thorium and uranium in solution by laser-induced breakdown spectrometry,” *Appl. Opt.*, vol. 4, pp. G58–G64, 2008.

14. I. Gaona, J. Serrano, J. Moros, and J. J. Laserna, “Evaluation of laser-induced breakdown spectroscopy analysis potential for addressing radiological threats from a distance,” *Spectrochim. Acta B*, vol. 96, pp. 12–20, 2014.

15. SciAps. (2019) LIBS Analyzer Models. [Online]. Available: https://www.sciaps.com/libs-handheld-laser-analyzers/z-series/

16. M. B. Shattan, D. J. Miller, M. T. Cook, A. C. Stowe, J. D. Auxier, C. Parigger, and H. L. Hall, “Detection of uranyl fluoride and sand surface contamination on metal substrates by hand-held laser-induced breakdown spectroscopy,” *Appl. Opt.*, vol. 56, no. 36, pp. 9868–9875, Dec 2017.

17. A. Rao, M. Cook, H. Hall, and M. Shattan, “Quantitative analysis of cerium-gallium alloys using a hand-held laser-induced breakdown spectroscopy device.” *Atoms*, vol. 84, no. 7, 2019.

18. A. Rao, “Rapid analysis of plutonium surrogate material via hand-held laser-induced breakdown spectroscopy,” Master’s thesis, Air Force Institute of Technology, Wright-Patterson AFB, 3 2020, an optional note.

19. H. Yoshii, K. Yanagihara, H. Imaseki, T. Hamano, H. Yamanishi, M. Inagaki, Y. Sakai, N. Sugiura, O. Kurihara, and K. Sakai, “Methodology using a portable x-ray fluorescence device for on-site and rapid evaluation of heavy-atom contamination in wounds: A model study for application to plutonium contamination,” *PLOS ONE*, vol. 9, no. 7, pp. 1–7, 07 2014. [Online]. Available: https://doi.org/10.1371/journal.pone.0101966

20. D. Kirsanov, V. Panchuk, A. Goydenko, M. Khaydukova, V. Semenov, and A. Legin, “Improving precision of x-ray fluorescence analysis of lanthanide mixtures using partial least squares regression,” *Spectrochimica Acta Part B: Atomic Spectroscopy*, vol. 113, pp. 126–131, 2015.

21. E. Judge, J. M. Berg, L. A. Le, L. N. Lopez, and J. E. Barefield, “LIBS Spectral Data for a Mixed Actinide Fuel Pellet Containing Uranium, Plutonium, Neptunium and Americium,” 2012.

22. G. L. Donati, R. S. Amais, and C. B. Williams, “Recent advances in inductively coupled plasma optical emission spectrometry,” *J. Anal. At. Spectrom.*, vol. 32, pp. 1283–1296, 2017.

23. M. Krachler and R. Alvarez-Sarandes, “Capabilities of high resolution ICP-OES for plutonium isotopic analysis,” *Microchemical Journal*, vol. 125, pp. 196 – 202, 2016.

24. Office of the Secretary of Defense, “2018 Nuclear Posture Review,” 2018.

25. C. Dowding, “19 - laser ablation,” in *Advances in Laser Materials Processing*, ser. Woodhead Publishing Series in Welding and Other Joining Technologies, J. Lawrence, J. Pou, D. Low, and E. Toyserkani, Eds. Woodhead Publishing, 2010, pp. 575 – 628.

26. H. Hu, X. Wang, and H. Zhai, “High-fluence femtosecond laser ablation of silica glass: effects of laser-induced pressure,” *Journal of Physics D: Applied Physics*, vol. 44, no. 13, p. 135202, mar 2011.

27. “The bohr model.” [Online]. Available: https://www.pas.rochester.edu/~blackman/ast104/bohr.html

28. U. Fantz, “Basics of plasma spectroscopy,” *Plasma Sources Science and Technology*, vol. 15, no. 4, pp. S137–S147, oct 2006.

29. “Overview of Spectroscopy,” jun 5 2019, [Online; accessed 2022-02-07].

30. D. Bulajic, M. Corsi, G. Cristoforetti, S. Legnaioli, V. Palleschi, A. Salvetti, and E. Tognoni, “A procedure for correcting self-absorption in calibration free-laser induced breakdown spectroscopy,” *Spectrochimica Acta Part B: Atomic Spectroscopy*, vol. 57, no. 2, pp. 339–353, 2002. [Online]. Available: https://www.sciencedirect.com/science/article/pii/S0584854701003986

31. F. Rezaei, G. Cristoforetti, E. Tognoni, S. Legnaioli, V. Palleschi, and A. Safi, “A review of the current analytical approaches for evaluating, compensating and exploiting self-absorption in laser induced breakdown spectroscopy,” *Spectrochimica Acta Part B: Atomic Spectroscopy*, vol. 169, p. 105878, 2020.

32. A. Kramida, Y. Ralchenko, and J. Reader, “NIST Atomic Spectra Database.” [Online]. Available: https://physics.nist.gov/asd

33. H. Jiajia, L. Zhang, Z. Yang, W. Zhe, Y. Zhang, M. Weiguang, D. Lei, Y. Wangbao, X. Liantuan, and J. Suotang, "Mechanisms and efficient elimination approaches of self-absorption in libs," *Plasma Science and Technology*, vol. 21, no. 3, p. 034016, 2019.

34. J. Patterson, "HH-XRF and HH-LIBS for alloy analysis Choosing the Right Tool for the Right Job," 2014.

35. "How xrf works." [Online]. Available: https://www.bruker.com/en/products-and-solutions/elemental-analyzers/handheld-xrf-spectrometers/how-xrf-works.html

36. SciAps, "LIBS vs. X-Ray," 2019. [Online]. Available: https://www.sciaps.com/libs-vs-x-ray-the-whole-story/

37. T. Akhmetzhanov, G. Pashkova, V. Chubarov, T. Labutin, and A. Popov, "Three calibration techniques combined with sample-effective design of experiment based on latin hypercube sampling for direct detection of lanthanides in ree-rich ores using txrf and wdxrf," *Journal of Analytical Atomic Spectrometry*, vol. 36, 01 2021.

38. B. T. Manard, E. M. Wylie, and S. P. Wilson, "Analysis of Rare Earth Elements in Uranium Using Handheld Laser-Induced Breakdown Spectroscopy (HH LIBS)," *Applied Spectroscopy*, vol. 72, no. 11, pp. 1653–1660, 2018.

39. P. Soderlind, F. Zhou, A. Landa, and J. Klepeis, "Phonon and magnetic structure in δ-plutonium from density-functional theory," *Scientific Reports*, vol. 5, p. 15958, 10 2015.

40. S. S. Hecker, "Plutonium: Coping with instability," *JOM*, vol. 55, no. 9, pp. 13–19, Sep 2003.

41. M. Steinzig and F. H. Harlow, "Characterization of cast metals with probability distribution functions," *MRS Proceedings*, vol. 538, 03 1999.

42. F. E. Gibbs, D. L. Olson, and W. Hutchinson, "Identification of a physical metallurgy surrogate for the plutonium—1 wt.% gallium alloy," *AIP Conference Proceedings*, vol. 532, no. 1, pp. 98–101, 2000.

43. M. Moore and Y. Tao, "Aerosol physics considerations for using cerium oxide ceo2 as a surrogate for plutonium oxide puo2 in airborne release fraction measurements for storage container investigations," 2017.

44. H. Zheng, F.-Y. Yueh, T. Miller, J. Singh, K. E. Zeigler, and J. C. Marra, "Analysis of plutonium oxide surrogate residue using laser-induced breakdown spectroscopy," *Spectrochimica Acta*, vol. 63, pp. 968–974, 2008.

45. J. Marra, "Cerium as a surrogate in the plutonium immobilized form," 6 2001.

46. J. Gruber, J. Heitz, N. Arnold, D. Bäuerle, N. Ramaseder, W. Meyer, J. Hochörtler, and F. Koch, "In situ analysis of metal melts in metallurgic vacuum devices by laser-induced breakdown spectroscopy," *Applied Spectroscopy*, vol. 58, no. 4, pp. 457–462, 2004.

47. G. Guo, G. Niu, Q. Shi, Q. Lin, D. Tian, and Y. Duan, "Multi-element quantitative analysis of soils by laser induced breakdown spectroscopy (libs) coupled with univariate and multivariate regression methods," *Anal. Methods*, vol. 11, pp. 3006–3013, 2019.

48. J. L. Gottfried, R. S. Harmon, F. C. D. Lucia, and A. W. Miziolek, "Multivariate analysis of laser-induced breakdown spectroscopy chemical signatures for geomaterial classification," *Spectrochim Acta B*, vol. 64, no. 10, pp. 1009 – 1019, 2009.

49. P. K. Tiwari, S. Awasthi, R. Kumar, R. K. Anand, P. K. Rai, and A. K. Rai, "Rapid analysis of pharmaceutical drugs using libs coupled with multivariate analysis," *Lasers in Medical Science*, vol. 33, no. 2, pp. 263–270, Feb 2018.

50. C. R. Bhatt, F. Y. Yueh, and J. P. Singh, "Univariate and multivariate analyses of rare earth elements by laser-induced breakdown spectroscopy," *Appl. Opt.*, vol. 56, no. 8, pp. 2280–2287, Mar 2017.

51. S. M. Clegg, E. Sklute, M. D. Dyar, J. E. Barefield, and R. C. Wiens, "Multivariate analysis of remote laser-induced breakdown spectroscopy spectra using partial least squares, principal component analysis, and related techniques," *Spectrochimica Acta Part B: Atomic Spectroscopy*, vol. 64, no. 1, pp. 79 – 88, 2009.

52. Z. Jaadi, "A step by step explanation of principal component analysis," May 2019. [Online]. Available: https://towardsdatascience.com/a-step-by-step-explanation-of-principal-component-analysis-b836fb9c97e2

53. D. Larose and C. Larose, *Data Mining and Predictive Analysis.* Wiley, 2015.

54. N. Yang, N. Eash, J. Lee, M. Martin, Y.-S. Zhang, F. Walker, and J. E. Yang, "Multivariate analysis of laser-induced breakdown spectroscopy spectra of soil samples," *Soil Science*, vol. 175, pp. 447–452, 09 2010.

55. P. Porizka, "Using laser-induced breakdown spectroscopy (libs) for material analysis," 2014.

56. Www.statsoft.com, "Partial least squares (pls)." [Online]. Available: http://www.statsoft.com/Textbook/Partial-Least-Squares

57. P. Geladi and B. Kowalski, "Partial-least squares regression: A tutorial," *Analytica Chimica Acta*, vol. 185, pp. 1–17, 1986.

58. S. Haykin, *Neural Networks: A Comprehensive Foundation.* Prentice Hall, 1999.

59. K. J. Cios and I. Shin, “Image recognition neural network: Irnn,” *Neurocomputing*, vol. 7, no. 2, pp. 159 – 185, 1995. [Online]. Available: http://www.sciencedirect.com/science/article/pii/0925231293E0062I

60. W. Mo, X. Luo, Y. Zhong, and W. Jiang, “Image recognition using convolutional neural network combined with ensemble learning algorithm,” *Journal of Physics: Conference Series*, vol. 1237, p. 022026, jun 2019. [Online]. Available: https://doi.org/10.1088%2F1742-6596%2F1237%2F2%2F022026

61. L. Rokach and O. Maimon, *Data Mining with Decision Trees.* World Scientific Publishing Company, 2007.

62. ——, *Decision Trees.* Boston, MA: Springer US, 2005, pp. 165–192. [Online]. Available: https://doi.org/10.1007/0-387-25465-X_9

63. B. Fresch, D. Hiluf, E. Collini, R. D. Levine, and F. Remacle, “Molecular decision trees realized by ultrafast electronic spectroscopy,” *Proceedings of the National Academy of Sciences*, vol. 110, no. 43, pp. 17 183–17 188, 2013. [Online]. Available: https://www.pnas.org/content/110/43/17183

64. E. Vasconcellos, R. Carvalho, R. Gal, F. LaBarbera, H. Capelato, H. Campos Velho, M. Trevisan, and a. Ruiz, “Decision tree classifiers for star/galaxy separation,” *The Astronomical Journal*, vol. 141, p. 189, 05 2011.

65. T. Hastie, R. Tibshirani, and J. Friedman, *The Elements of Statistical Learning*, 2nd ed. New York: Springer-Verlag, 2009.

66. V. Cherkassky, *Predictive Learning.* Minneapolis, Minnesota: VCtextbook, 2013.

67. H. Takeda, S. Farsiu, and P. Milanfar, “Kernel regression for image processing and reconstruction,” *IEEE Transactions on image processing*, vol. 16, no. 2, pp. 349–366, 2007.

68. R. Blundell and A. Duncan, “Kernel regression in empirical microeconomics,” *Journal of Human Resources*, pp. 62–87, 1998.

69. G. Long and J. Winefordner, “Limit of detection. a closer look at the iupac definition,” *Analytical Chemistry - ANAL CHEM*, vol. 55, 09 2008.

70. F. Rezaei, P. Karimi, and S. H. Tavassoli, “Effect of self-absorption correction on libs measurements by calibration curve and artificial neural network,” *Applied Physics B*, vol. 114, 07 2013.

71. M. Zaghloul, “Computing the faddyeeva and voigt functions,” *Software*, vol. 38, no. 15, 2011.

72. A. P. Rao, P. R. Jenkins, J. D. Auxier II, and M. B. Shattan, “Comparison of machine learning techniques to optimize the analysis of plutonium surrogate material via a portable libs device,” *Journal of Analytical Atomic Spectrometry*, vol. 36, no. 2, pp. 399–406, 2021.

73. S. García, J. Luengo, and F. Herrera, *Data preprocessing in data mining.* Springer, 2015, vol. 72.

74. Z. Cong, L. Sun, Y. Xin, Y. Li, and L. Qi, “Comparison of Calibration Curve Method and Partial Least Square Method in the Laser Induced Breakdown Spectroscopy Quantitative Analysis,” *Journal of Computer and Communications*, vol. 1, pp. 14–18, 2013.

75. H. Yage, X. Wang, G. Shuai, A. Li, X. Xu, N. Wazir, D. Chunjie, T. Lu, L. Xie, M. Zhang, Y. Hao, W. Guo, and R. Liu, “Lithium ion detection in liquid with low detection limit by laser-induced breakdown spectroscopy,” *Applied Optics*, vol. 58, p. 422, 01 2019.

76. Y. Tang, S. Ma, Y. Chu, T. Wu, Y. Ma, Z. Hu, L. Guo, X. Zeng, J. Duan, and Y. Lu, “Investigation of the self-absorption effect using time-resolved laser-induced breakdown spectroscopy,” *Opt. Express*, vol. 27, no. 4, pp. 4261–4270, Feb 2019. [Online]. Available: http://www.opticsexpress.org/abstract.cfm?URI=oe-27-4-4261

77. A. P. Rao, M. Gragston, A. K. Patnaik, P. S. Hsu, and M. B. Shattan, “Measurement of electron density and temperature from laser-induced nitrogen plasma at elevated pressure,” *Opt. Express*, vol. 27, no. 23, pp. 33 779–33 788, Nov 2019.

78. J. Guezenoc, A. Gallet-Budynek, and B. Bousquet, “Critical review and advices on spectral-based normalization methods for libs quantitative analysis,” *Spectrochimica Acta Part B: Atomic Spectroscopy*, vol. 160, p. 105688, 2019. [Online]. Available: http://www.sciencedirect.com/science/article/pii/S0584854719302794

79. D. Syvilay, N. Wilkie-Chancellier, B. Trichereau, A. Texier, L. Martinez, S. Serfaty, and V. Detalle, “Evaluation of the standard normal variate method for laser-induced breakdown spectroscopy data treatment applied to the discrimination of painting layers,” *Spectrochimica Acta Part B: Atomic Spectroscopy*, vol. 114, pp. 38 – 45, 2015. [Online]. Available: http://www.sciencedirect.com/science/article/pii/S0584854715002359

80. A. Ismaël, B. Bousquet, K. M.-L. Pierrès, G. Travaillé, L. Canioni, and S. Roy, “In situ semi-quantitative analysis of polluted soils by laser-induced breakdown spectroscopy (libs),” *Applied Spectroscopy*, vol. 65, no. 5, pp. 467–473, 2011, pMID: 21513588. [Online]. Available: https://doi.org/10.1366/10-06125

81. P. Heraud, B. R. Wood, J. Beardall, and D. McNaughton, “Effects of pre-processing of raman spectra on in vivo classification of nutrient status of microalgal cells,” *Journal of Chemometrics*, vol. 20, no. 5, pp. 193–197, 2006. [Online]. Available: https://onlinelibrary.wiley.com/doi/abs/10.1002/cem.990

82. Y. Guo, Y. Ni, and S. Kokot, “Evaluation of chemical components and properties of the jujube fruit using near infrared spectroscopy and chemometrics,” *Spectrochimica Acta Part A: Molecular and Biomolecular Spectroscopy*, vol. 153, pp. 79 – 86, 2016. [Online]. Available: http://www.sciencedirect.com/science/article/pii/S1386142515301657

83. F. Rezaei, G. Cristoforetti, E. Tognoni, S. Legnaioli, V. Palleschi, and A. Safi, “A review of the current analytical approaches for evaluating, compensating and exploiting self-absorption in laser induced breakdown spectroscopy,” *Spectrochimica Acta Part B: Atomic Spectroscopy*, vol. 169, p. 105878, 2020. [Online]. Available: https://www.sciencedirect.com/science/article/pii/S0584854720301488

84. T. Zhang, H. Tang, and H. Li, “Chemometrics in laser-induced breakdown spectroscopy,” *Journal of Chemometrics*, vol. 32, no. 11, p. e2983, 2018, e2983 CEM-17-0119.R1. [Online]. Available: https://onlinelibrary.wiley.com/doi/abs/10.1002/cem.2983

REPORT DOCUMENTATION PAGE

1. REPORT DATE 12-05-2022	**2. REPORT TYPE** Doctoral Dissertation	**3. DATES COVERED** **START DATE** Apr 2020	 **END DATE** Sept 2022

4. TITLE AND SUBTITLE

Enabling rapid chemical analysis of plutonium alloys via machine learning-enhanced atomic spectroscopy techniques

5a. CONTRACT NUMBER	**5b. GRANT NUMBER**	**5c. PROGRAM ELEMENT NUMBER**
5d. PROJECT NUMBER	**5e. TASK NUMBER**	**5f. WORK UNIT NUMBER**

6. AUTHOR(S)

1st Lt Ashwin P. Rao

7. PERFORMING ORGANIZATION NAME(S) AND ADDRESS(ES) Air Force Institute of Technology Graduate School of Engineering and Management (AFIT/EN) 2950 Hobson Way WPAFB, OH 45433-7765	**8. PERFORMING ORGANIZATION REPORT NUMBER** AFIT/GAP/ENP/11-S01

9. SPONSORING/MONITORING AGENCY NAME(S) AND ADDRESS(ES)	**10. SPONSOR/MONITOR'S ACRONYM(S)**	**11. SPONSOR/MONITOR'S REPORT NUMBER(S)**

12. DISTRIBUTION/AVAILABILITY STATEMENT

DISTRIBUTION A; APPROVED FOR PUBLIC RELEASE; DISTRIBUTION UNLIMITED

LA-UR-22-22098

13. SUPPLEMENTARY NOTES

14. ABSTRACT

Analytical atomic spectroscopy methods have the potential to provide solutions for rapid, high fidelity chemical analysis of plutonium alloys. Implementing these methods with advanced analytical techniques can help reduce the chemical analysis time needed for plutonium pit production, directly enabling the 80 pit-per-year by 2030 manufacturing goal outlined in the 2018 Nuclear Posture Review. Two commercial, handheld elemental analyzers were validated for potential in situ analysis of Pu. A handheld XRF device was able to detect gallium in a Pu surrogate matrix with a detection limit of 0.002 wt% and a mean error of 8%. A handheld LIBS device was able to yield univariate detection limits as low as 0.1 wt% Ga with mean error of 3%. Implementing machine learning methods for spectral analysis with the handheld LIBS device reduced error to 0.27%, but the limited device resolution impedes improvements in sensitivity. A compact Echelle spectrometer was implemented with a laboratory LIBS setup to reach a detection limit of 0.006 wt% Ga when coupled with an optimized extra trees regression. A Gaussian kernel regression trained on this high resolution data set yielded the most accurate predictive model with 0.33% error. Lastly, the phenomenon of self-absorption was quantified and corrected for in Ce-Ga LIBS spectra. By implementing a Stark broadening based correction, the univariate detection limit for Ga from LIBS spectra was reduced to 0.008$\%$. Overall, this research indicates that implementing a compact, high resolving power spectrograph for recording Pu alloy spectra and developing optimized machine learning models for spectral analysis can yield high fidelity solutions for Pu alloy chemical analysis and quality control.

15. SUBJECT TERMS

Laser-induced breakdown spectroscopy; LIBS; plutonium alloys; machine learning

16. SECURITY CLASSIFICATION OF:			**17. LIMITATION OF ABSTRACT**	**18. NUMBER OF PAGES**
a. REPORT U	**b. ABSTRACT** U	**C. THIS PAGE** U	U	135

19a. NAME OF RESPONSIBLE PERSON	**19b. PHONE NUMBER** *(Include area code)*
Dr. Anil K. Patnaik, AFIT/ENP	937-255-3636 x4532